

**Brain-inspired algorithms to approach
engineering applications and conversely
to study the brain:
the Basal Ganglia and the Cerebellum.**



Rubén Darío Pinzón Morales

Department of Computer Science
Chubu University

This dissertation is submitted for the degree of
Doctor of Engineering

Graduate School of Engineering

January 2015

Please avoid printing this document where possible to avoid wasting paper, if printed copy
is required please print double sided. Take care of the enviorement.



Copyright ©2015 Rubén Darío Pinzón Morales

All rights reserved. No part of this publication may be reproduced, stored in a retrieval system, or transmitted, in any form or by any means, electronic, mechanical, photocopying, recording, or otherwise, without permission of the author.

Printed in Japan.

Declaration

I hereby declare that except where specific reference is made to the work of others, the contents of this dissertation are original and have not been submitted in whole or in part for consideration for any other degree or qualification in this, or any other university. This dissertation is my own work and contains nothing which is the outcome of work done in collaboration with others, except as specified in the text and Acknowledgements. This dissertation contains fewer than 65,000 words including appendices, bibliography, footnotes, tables and equations and has fewer than 150 figures.

Rubén Darío Pinzón Morales

January 2015

Summary

This thesis focuses on two brain structures, involved in motor control, coordination and learning. The Basal Ganglia (BG) and the cerebellum. The philosophy through this thesis consider the developing of computational methods inspired in these brain areas to approach engineering applications and in turn, learn about the Basal Ganglia and the Cerebellum.

Chapter 2 showed the development of a novel computational method for analysis of neural activity from the BG with the purpose of automatically identify the subthalamic nucleus (STN), a common target for Deep Brain Stimulation (DBS), was presented. This is important because it aids the implantation of the electrode of the DBS during treatment of advanced cases of Parkinson's disease. In **Chapter 3** we introduced a detailed description of a realistic neuronal network model of the cerebellum and its application into classical control was tested. This chapter illustrated the versatility of the cerebellar model and exemplify how to integrate it into feedback control loops to improve the control performance obtained with classical controllers.

Chapter 4, 5, and 6 attempt to solve three unanswered questions about the cerebellum with the help of the model developed in **Chapter 3** during engineering applications. First, **Chapter 4** focuses on the type of error information carried in the CF. It is important to clarify the type of error because of the critical role of the CF input in cerebellar learning. We show that learning in the model is adequately driven by SE, ME, or a combination of the two during all the control scenarios tested. The second question, tackled in **Chapter 5**, is the mechanisms of asymmetrical cerebellar learning. We show that two features in the model are sufficient to produce asymmetrical adaptation. First, a bi-hemispherical structure, and second, a CF with direction sensitivity and low-frequency firing rate content. Finally, the third question explored in **Chapter 6** concerns the role of the abundant number of GCs. We explore this question by selectively knocking down the output of the GCs in the model and analyzing the behavioral and neural consequences. The model presents an unique framework to evaluate the GCs role in the cerebellar circuit in opposition to physiological experiments because the integrity of the cerebellar circuit can be secure in the model while it is outstandingly difficult to achieve successful isolation of GCs in the real biological system.

cal system. Results showed that increasing the number of GCs improve motor performance and robustness of the cerebellar model against structural changes. In particular, a model with large number of GCs demonstrates to be highly stable even when the initial conditions and synaptic weights are changed.

This thesis demonstrated that by creating computational methods inspired by the brain, solutions to engineering applications in diverse fields such as neuroscience, medicine, and control engineering can be established. In turn, incorporation of computational models into engineering applications provided a unique framework to test and proposed new hypotheses about the brain.

Table of contents

Summary	iv
Table of contents	vi
List of figures	ix
List of tables	xi
1 Introduction	1
1.1 Historical Overview	2
1.2 Neural circuits of the the Basal Ganglia and the cerebellum	4
1.3 Basal Ganglia and Parkinson's Disease	7
1.4 Cerebellar motor learning	9
1.5 Motivation	11
1.6 Scope of this thesis	12
2 Analysis of Basal Ganglia's neural activity during Parkinson's disease	16
2.1 Introduction	17
2.2 Methodology for automatic identification of Basal Ganglia's neural activity	17
2.2.1 Wavelet function optimization based on genetic algorithms	20
2.2.2 Database of microelectrode recordings (MER) from the Basal Ganglia	22
2.3 Results	23
2.3.1 New wavelet function inspired by the neural activity of the Basal Ganglia	23
2.3.2 Comparison of the classification performance with the new and classical wavelets	24
2.3.3 Automatic identification of Basal Ganglia with MER, LFP and spikes	26
2.4 Discussion	27

3 Model of the cerebellum for adaptive robot control	30
3.1 Introduction	31
3.2 The neuronal network model of the cerebellum	31
3.3 Robot control experiments with the cerebellar model	35
3.3.1 Characteristics of the control objects	35
3.3.2 Experimental protocol	37
3.4 Results	38
3.4.1 Control of a 1 DoF plant: a DC motor	38
3.4.2 Control of a 2 DoFs plant: a two-wheel balancing robot	38
3.4.3 Control of a 6 DoFs plant: a simulated quadcopter	40
3.5 Discussion	41
4 Error signals in the climbing fiber required for cerebellar motor learning	44
4.1 Introduction	45
4.2 Configuration of the model to test the CF error content	46
4.2.1 Nature of the two types of error information in CF	46
4.2.2 Experimental protocol	47
4.3 Results	47
4.3.1 Simple control scenario	47
4.3.2 Complex control scenario	50
4.3.3 Neural consequences of the CF error content	51
4.4 Discussion	54
5 Mechanisms of asymmetrical cerebellar motor learning	58
5.1 Introduction	59
5.2 Configuration of the model to produce asymmetrical adaptation	60
5.2.1 Low-DC firing rate in the CF	60
5.2.2 Experimental protocol	62
5.3 Results	63
5.3.1 Symmetrical control scenario	63
5.3.2 Asymmetrical control scenario	68
5.3.3 Effect of the CF low-DC firing rate in the model	70
5.4 Discussion	72
6 Role of the abundant number of cerebellar granule cells	75
6.1 Introduction	76
6.2 Experimental protocol	77

6.3 Results	77
6.3.1 Behavioral consequences of the number of GCs	78
6.3.2 Neural consequences of the number of GCs	83
6.4 Discussion	86
7 Discussion and Future research	89
References	95
Appendix A LabVIEW framework for building neuronal network models of the cerebellum	107
A.1 Introduction	108
A.2 LabVIEW architecture	109
A.2.1 Off-line construction of the cerebellar network	109
A.2.2 Integrating the neural network model to the engineering application	111
A.3 Results	113
A.4 Conclusions	113
Appendix B Mobile and stand alone implementation of the cerebellar model	118
B.1 Introduction	119
B.2 Characteristics of the real time device	119
B.3 Results	119
B.4 Discussion	122
Appendix C List of publications	123

List of figures

1.1	Neural circuits of the BG and the cerebellum	5
1.2	Deep brain stimulation of the BG	8
1.3	Original scheme of the cerebellar model articulation controller (CMAC) . .	10
1.4	The three pillars of the philosophy of this thesis	12
1.5	Overview of this thesis	15
2.1	General scheme of the proposed computational method for identification of Basal Ganglia nuclei	18
2.2	Lifting scheme construction of the wavelet transform	19
2.3	General diagram of the wavelet optimization procedure	21
2.4	Microelectrode recording signal and typical components.	23
2.5	New wavelet function for analysis of MER signals	24
2.6	Classification performance with the optimal and classical wavelet	25
2.7	3D feature space visualization tool for identification of BG	26
3.1	General scheme of the cerebellar model and its configuration for robot control	32
3.2	Real and simulated robot plants and their control variables	36
3.3	Control performance during control of the DC motor	39
3.4	Control performance during control of the two-wheel balancing robot . .	41
3.5	Control performance during control of the quadcopter	42
4.1	Control performance with a DC motor and different types of CF input . .	48
4.2	CF activities during control of the DC motor	49
4.3	Control performance with the two-wheel balancing robot and different types of CF input	50
4.4	Firing rates of CF and PC during control of the two-wheel balancing robot .	52
4.5	Synaptic weights between GC and PC during control of the two-wheel balancing robot	53
4.6	Correlation of GC's firing rate, CF, and MFs versus GCs	55

4.7	Control performance during control of the two-wheel balancing robot in terms of RSE of ME	56
5.1	Climbing fiber with low-DC firing rate	61
5.2	Control plant and symmetrical/asymmetrical perturbations	62
5.3	Control performance during symmetrical perturbation	64
5.4	Asymmetrical control scenarios with a uni-hemispheric cerebellar model . .	65
5.5	Performance achieved during control of the robot at different frequencies of the desired motion and perturbations	67
5.6	Performance of the robot under asymmetrical conditions with an external load	69
5.7	Performance attained during asymmetrical perturbation control of the robot	71
5.8	Effects of the spontaneous CF in the cerebellar model	73
6.1	Comparison of control performance with the number of GCs during control of the DC motor	79
6.2	Comparison of control performance with the number of GCs during control of the two-wheel balancing robot	81
6.3	Comparison of control performance with the number of GCs during control of the quadcopter	82
6.4	Control performance and variability due to the initial conditions	84
6.5	Firing rate of PCs and VN as the number of GCs changes	84
6.6	GO and MF input pattern of the GCs in the cerebellar model	87
A.1	General scheme of the software architecture in LabVIEW	108
A.2	UML class diagram of the LabVIEW application.	110
A.3	Algorithm for allocation of neurons inside the cube of cerebellar cortex .	112
A.4	Algorithm for connecting the neurons inside the cube of cerebellar cortex .	114
A.5	Address Event Representation (AER) for representation of the cerebellar network	115
A.6	Algorithm for computing the firing rate of each neuron	116
A.7	Example neuronal networks	117
B.1	Implementation of the cerebellar model into a real-time portable device .	120
B.2	Control performance with a real-time device implementation of the model .	121
B.3	Execution time of the cerebellar model taken by the myRIO and a Windows PC	122

List of tables

2.1	Classification in terms of sensitivity (E) and specificity (F) using LFP, spikes, and raw MER signals 3D spaces generated with the optimal wavelet function.	27
2.2	Classification and statistical analysis of the bi-class classification problem .	28
2.3	Computational time of the proposed computational method. $CU = 0.0010$ seconds on the test-bench computer.	29
3.1	Convergence and divergence synaptic ratio of the cerebellar model	33
3.2	Mossy fibers for each control plant	34

1

Introduction

HE brain has been the ultimate source of awe of researchers for centuries. Understanding the brain mechanisms of cognition, memory, motor control, and consciousness has been a preeminent goal. The cerebellum and the basal ganglia are two of the most studied brain areas because of the evident psychomotor symptoms resulted from deficiencies in these areas. Parkinson's disease, voluntary tremor, atonia, asthenia, and astasia are some of the pathologies linked to the basal ganglia and the cerebellum. Computational methods to understand the brain have the potential to cast light into its mechanism and function, and also to provide effective approaches to solve engineering applications. Here we embark upon the study of the basal ganglia and the cerebellum using computational methods and explore their use in engineering applications.

1.1 Historical Overview

The Basal Ganglia

The basal ganglia (BG) was not recognized as a specific brain area involved in the control of psychomotor behavior until the end of the sixteenth century¹¹⁹. A first identification of its structures was presented by Andreas Vesalius (1524-1564), however, he did not hypothesized about its functional significance. Thomas Willis (1621-1675) introduced the term *corpus striatum* (striated or chamfered body) for the biggest BG nuclei and recognized its role in sensorimotor integration. Karl Friedrich Burdach (1776-1847) provided the first differentiation of the striatum into the putamen and the caudate nucleus. He also identified a grayish structure within the inner portion of the lentiform nucleus that he termed “globus pallidus”, correctly identified its inner and outer segments, and described the fiber fascicles that separate the elements (i.e., internal and external capsule) of the BG. Félix Vicq-d’Azyr (1748-1794) discovered the substantia nigra and claustrum¹¹⁹. Thereafter, research about the BG was relayed to the background because of other discoveries in the cerebral cortex and cerebellum that called out the attention of the scientific community. In the 20th century the BG came back to the spotlight after movement disorders were reported with injuries in the striatum. During this century, the development in tracing techniques to delineate neuronal pathways and connections, histochemical methods to localize neurotransmitters, enzymes and receptor bindings provided the tools for a better understanding of the networks in the BG¹¹⁸. Further advances in neurophysiological recording techniques and biological analysis clarified the molecular and functional characteristics of individual neuron types, including their integration in the BG and related networks¹⁴⁶. Consensus and compiling reviews have been presented^{110;134}. Mathematical models of the BG started emerged in recent years because of the increasing necessity of interpretation of the vast amount of experimental data accumulated⁵⁴.

The cerebellum

The cerebellum first mentioned in the biological writings of Aristotle 2400 years ago, has been the center of more speculation than almost any other part in the nervous system³⁶. The earliest documented references to the cerebellum dates back to Aelius Galenus (AD 129-199) who considered the cerebellum to be the source of motor nerves and the spinal cord. He claimed that the vermis of the cerebellum acts as a valve to regulate the flow of the animal spirit through the ventricular system. This notion prevailed until the seventeenth century. During this and the eighteenth centuries there were no further significant

attempts to explain cerebellar function, instead paying more attention to its anatomical features. Anatomists were aided by new techniques developed by Raymond Vieussens (1635-1715) for boiling the brain in oil and Johann C Reil's (1759-1809) alcohol fixation process, producing outstanding copperplate illustrations, however, little was known of these works because they remained enclosed to German-reading nations. By 1837 Jan Evangelista Purkyně (1787-1869) using achromatic microscope discovered the most important cell of the cerebellum still known today by his name, the Purkinje cell³⁶. Luigi Rolando (1773-1831) performed the first experiments towards studying the function of the brain and cerebellum. He ablated portions of the brain in a wide variety of animals and correctly concluded on the motor nature of the cerebellum. Nonetheless, he thought that the cerebellum was the “organ controlling motion” rather than regulating motor activity. Marie Jean Pierre Flourens (1794-1867) revised this notion and suggested that the cerebellum was involved in control of posture and movements. He wrote “all movements persist following ablation of the cerebellum: all that is missing is that they are not regular and coordinated”^{40;148}. Luigi Luciani (1842-1919) demonstrated later that by ablation of the cerebellum three main motor symptoms were acquired: atonia, asthenia and astasia⁹⁹, which are still recognized as the main motor manifestation of cerebellar dysfunction. Thereafter, Gordon Holmes (1917-1922) identified the association of the cerebellum with diskinesia and voluntary tremors during clinical observations of 1st world war injured soldiers. Enormous steps toward understanding the cerebellum came forward with the work of Camillo Golgi (1843-1926) and Santiago Ramón y Cajal (1852-1934). Camillo Golgi opened the door to the detailed morphology studies with his silver staining method in 1873. He described the fine anatomical structure of the nervous system and the morphology of a ‘big nerve cell’ that later was named after him, the Golgi cell⁴⁹. Ramón and Cajal carried out extensive investigation of the morphology of the nerve cells and their processes, the communication between neurons, and their capability to plastically modify their synapses. Later he proposed his doctrine of the neuron and described the neuron cells of the molecular layer of the cerebellum, in particular, neurons that form “baskets” around the Purkinje cells. He also showed the intimate contact of climbing fibers with the dendrites of Purkinje cell, and the projections of mossy fibers to granule and Golgi cells by mossy fibers¹³². The works of Ramón and Cajal and Golgi, showed that the cerebellar cortex was relatively simple morphologically and homogeneous through its folia²⁷.

Modern studies of the physiology, anatomy, and theory of function of the cerebellum started with John Eccles (1903-1997), Janos Szentágothai (1912-1994), Masao Ito (1953-), David Marr (1945-1980) and James Albus (1935-2011)¹⁴⁸. They identify the wiring of the cerebellar neural circuit, its learning capabilities, and the inhibitory and excitatory nature

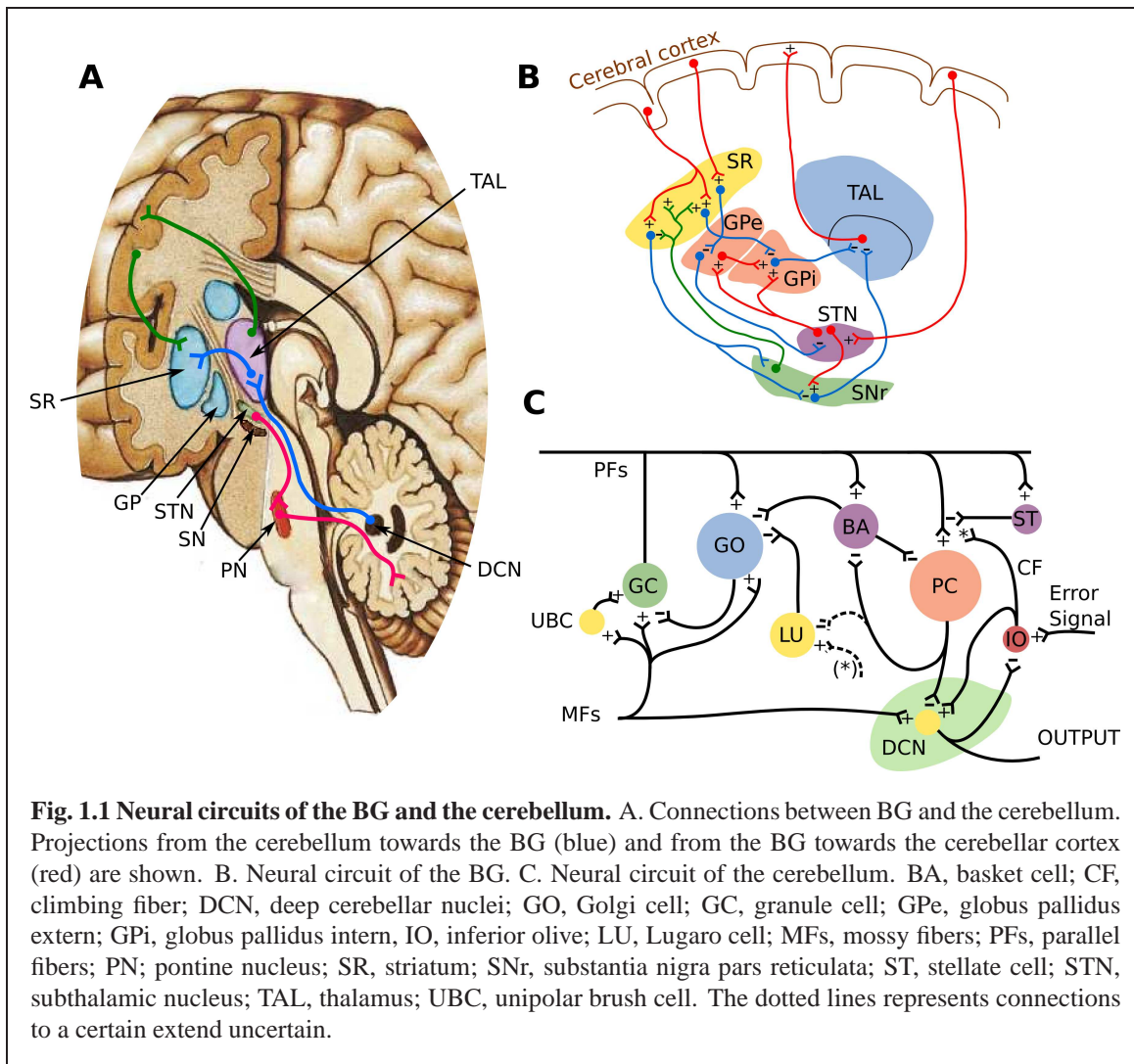
of its neurons. Eccles proposed the “beam theory”³⁵ according to which beams of information reach the Purkinje cell via parallel fibers of granule cells. However, this hypothesis was uniquely based on anatomy and disregarded circuit dynamics⁴⁴. David Marr and James Albus proposed the “motor learning theory”^{2;103}. According to this theory afferent input events conveyed by the mossy fibers to the cerebellar cortex are expanded into smaller representations by the granule cells, and that learning happens by facilitation at synapses between parallel fiber and Purkinje cell with the conjunction of presynaptic (i.e., parallel fiber activity) and climbing fiber activity. Later on Ito formulated the “forward controller theory”⁷¹, which considered the cerebellar function in terms of motor system control. Although the Marr-Albus-Ito theory is one of the most prevalent theories of cerebellar functioning in the present, other more abstract approaches have also been presented, such as the “adaptive filter theory”³¹, and the “tensor network theory”¹²⁰.

1.2 Neural circuits of the the Basal Ganglia and the cerebellum

Before describing the neural network of the BG and the cerebellum, in this paragraph the interconnection between these two structures is presented. The BG and the cerebellum are interconnected^{11;12} (**Fig. 1.1A**). The traditional view was that any interaction between these two structures occurred at the neocortical level⁸². However, recent experiments with virus and retrovirus have identified disynaptic pathways that directly link the cerebellum with the BG¹³. The dentate nucleus in the deep cerebellar nuclei projects disynaptically to the striatum (caudate and putamen) (**Fig. 1.1A**, blue lines), whereas the subthalamic nucleus projects disynaptically to the cerebellar cortex (**Fig. 1.1A**, red lines). These pathways act in both motor, and non-motor somatotopic areas of the cerebellum and BG, and therefore, both structures could possibly influence each other in non-motor, as well as motor functions¹¹.

Neural circuit and function of the Basal Ganglia

The neural network in the BG⁵⁵ in the primates includes the nuclei shown in **Fig. 1.1B**. These are the striatum (ST), globus pallidus (GP) and the subthalamic nucleus (STN) in the forebrain, and the substantia nigra (SN) in the midbrain. The GP is further subdivided in the internal and external segments (GPi and GPe, respectively), while the ST contains distinct areas denominated compacta (SNC) and reticulata (SNr). The major source of excitation in the BG is the STN⁵⁵, whereas most of the other nuclei are inhibitory. The SNC provides dopaminergic input to the ST and might exert both inhibitory and excitatory effects



depending on the receptor type in the post-synaptic cells (i.e., D1 or D2 type receptors, respectively). The major portion of neurons in the ST is GABAergic spiny cells, receiving excitatory inputs to the BG from wide range of brain structures and also dopaminergic input from SNC. In turn, they provide phasic inhibitory output to the GPi, GPe, and SNr. Activity of the SNC propagates through the BG via the ST. The couple GPi/SNr receives projections exclusively from spiny cells associated to D1-type receptor, whereas GPe receives projections mainly from spiny cell binding to D2-type receptors⁴⁸. The major outputs of the BG are the GPi and SNr, which provide extensively GABAergic efferents to functionally related zones in the ventral thalamus (TAL), which in turn projects back to the cerebral cortex, superior colliculus, cerebellar cortex¹¹, and other brain stem areas^{54;55}.

The function of the BG in motor control/coordination is to prepare the starting and stop-

ping of voluntary motions by means of the Direct and Indirect pathways. The Direct pathway provides a “gate” role to avoid unwanted movements by inhibiting the TAL. It comprises the projections from motivation and association cortices in the cerebral cortex, the GPi, SNC, and the outputs to the ventral part of the TAL. The indirect pathway serves as a double brake by nullifying the effects of the direct pathway. It includes the STN and GPi.

Neural circuit and function of the cerebellum

The cerebellar cortex has a homogeneous structure all over its volume, and it has vast connections to the most important structures of the central nervous system, including brainstem, spinal cord, BG, and TAL. Its basic learning algorithm is sometimes called a generic algorithm of the cerebellum^{25;69}(Fig. 1.1C). The cerebellar network can be subdivided into four main layers: the granular layer, the molecular layer, the deep-cerebellar layer, and the inferior olive²⁵. The granular layer includes granule cells (GCs), Golgi cells (GOs), Lugaro cells (LUs), and Unipolar brush cells (UBCs) (only in the vestibulocerebellum, see below)⁶⁹. The molecular layer includes basket cells (BAs), stellate cells (SCs), and Purkinje cells (PCs). Inputs from brainstem nuclei (notably the reticular nucleus and the red nucleus) are carried to the cerebellar circuit via mossy fibers (MFs). GCs are the smallest (soma diameter 5-8 μm), the only excitatory neuron in the cerebellar cortex with UBCs, and the most numerous neurons in the brain^{25;69}. Each GC receives four to five MFs and same number of inhibitory GO projections. GOs are large neurons with dendrites that extend like a bouquet into the molecular layer and also send descending projections to the granular layer. GO exerts extensive spatio-temporal modulation of activity at the granular layer⁴⁴. They receive excitatory input from parallel fibers (PFs) of GCs forming a feedback loop, and excitatory inputs by MFs. LUs are serotonergic neurons located slightly below the PCs. They reach GOs and might play a role in synchronizing populations of GOs³³. PCs are the largest neurons in the cerebellar cortex, extending planar fan-like dendrites perpendicular to the PFs. The number of PFs contacting a single PC can be as high as 180,000⁶⁹ in humans. PC is the single output of the cerebellar cortex sending inhibitory projection to the deep-cerebellar nuclei, and collaterals to BAs. BAs and SCs are middle size neurons in the molecular layer close to the PCs. BA synapses onto the bottleneck of the PC soma, whereas the SC makes synapses with the dendrites of the PC. BAs also contact GOs in the granular layer providing a strong feedback inhibition loop with the potential to modulate the activity of GCs. BA receives inputs from PFs, thus, forming a feed-forward inhibition loop to control PC activity. Each PC is contacted by a single climbing fiber (CF) originating from the inferior olivary nucleus. The CF produces strong calcium gradients in the dendrites of PCs affecting the synaptic efficiency of PF-PC synapses, and has been proposed to the

mechanism of cerebellar learning⁷¹.

When initiating a movement, the frontal and parietal cerebral cortex also send an efference copy of the movement to the cerebellum, via relay neurons in the Pons. The purpose of this efference copy is to provide information to compare with the sensory feedback the cerebellum gets from various nuclei in the brainstem. The spinal cord relays the proprioceptive information of ongoing movements and posture from the abundant muscle spindles and other mechano-receptors in the body, while the vestibular nuclei send information on angular and linear acceleration from the labyrinth in the ear. As mentioned above, the inferior olive plays an active role in developing the memory in the cerebellum. The cerebellar cortex is functionally divided in three major parts, the cerebrocerebellum related with higher functions such as speech and fine-tune motion of the hands, the spinocerebellum that receives direct input from the spinal cord and it's mainly concerned with distal muscle movements such as walking control, and the vestibulocerebellum that is involved in eye movement reflexes, posture and equilibrium. Movement regulation exerted by the PCs is achieved by the modification of the PF-PC synaptic efficiency via the CF input. Modification of these synapses translates in modulation of the PC activity and the inhibition to the deep cerebellar nuclei. The deep cerebellar nuclei inhibits the TAL via the brainstem relay closing the loop between the cerebral cortex and the cerebellum.

1.3 Basal Ganglia and Parkinson's Disease

Parkinson's disease is the second most common neurodegenerative disease after Alzheimer's disease⁴. Estimated prevalence for those aged 65-74 years is 598 (per 100.000)¹⁵⁶. The pathophysiology of Parkinson's disease is characterized by four cardinal motor symptoms: slowness in both the beginning and the execution of a movement (bradykinesia), muscle rigidity, tremor, and postural instability (balance impairment)^{4;24}. Parkinson's disease involves the loss of dopaminergic cells in the SNc (**Fig. 1.1B**)⁵⁶. This leads to depletion of dopamine in the SR (**Fig. 1.1B**) and abnormal oscillatory activity in the BG. The cerebellum has been shown to be interconnected with the BG (**Fig. 1.1A**)^{12;13} and therefore its involvement in Parkinson's disease has been suggested^{11;166}. Cerebellar activity during Parkinson's disease is abnormal¹³. In human patients and monkey models of the disease, oscillatory activity at tremor frequencies has been recorded in regions of the TAL that receives projections from the cerebellum rather than from the BG¹³. Normally, drug treatment with Levodopa drugs reduces symptoms, however in advanced cases of Parkinson's disease drug treatment gives a way to deep brain stimulation (DBS).

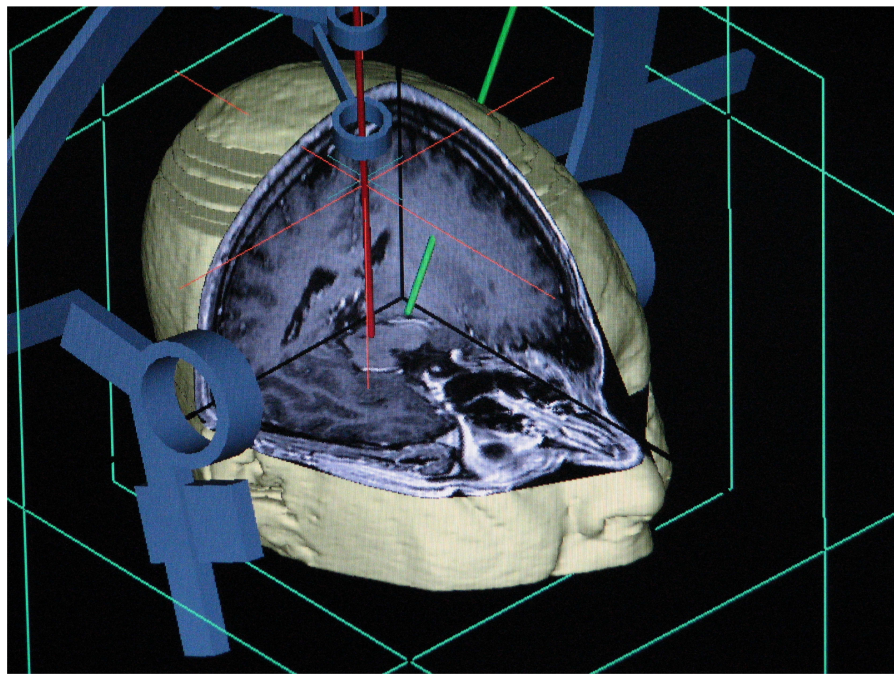


Fig. 1.2 Trajectory commonly used to approach the STN in the BG during the DBS procedure. Red and green bars show the left and right electrodes used during a double-size DBS implantation procedure. The stereotactic frame is shown.

Deep Brain Stimulation for Parkinson’s Disease treatment

Deep brain Stimulation (DBS) of the BG nuclei has become a standard treatment for advanced cases of Parkinson’s disease. Among the different nuclei within the BG, the STN is the preferred target for placing the DBS electrode, although other zones are also feasible⁴⁷. Stimulation of the STN is not only highly effective in reducing the motor symptoms of Parkinson’s disease, but also restores the cerebellar activity and function¹³. Success in DBS procedures relies on the correct localization of the target nucleus, where the stimulation microelectrode is to be placed¹⁶⁴(**Fig. 1.2**). For this purpose, stereotactic frames and T1-weighted magnetic resonance images are used for preoperative planning of the path to the target. Additionally, electrophysiological techniques that can provide intraoperative information, such as microelectrode recordings (MER), are frequently used to refine the precision of targeting¹⁷⁰. In practice, skilled specialists use visual and acoustic clues of the microelectrode recording for determining the position of the target. However, elevated uncertainty and mistakes can arise from this highly subjective and human-dependent approach. Furthermore, microelectrode recordings from several nuclei may express similar activity, making the recognition task more arduous. In this sense, a computer-assisted system for automatic

identification of nuclei would be of outstanding help during DBS implantation.

1.4 Cerebellar motor learning

Cerebellar motor learning can be regarded as the activity-dependent modification of synaptic transmission efficiency. Specifically, plasticity at PF-PC synapses has been considered the core of the cerebellar dependent learning because of its location within the neural circuit and the vast number of PF⁶⁹. Back in the forties the pioneers of cerebellar research David Marr, James Albus, and Masao Ito, proposed that modification of the synaptic efficiency at PF-PC driven by the error information conveyed in the CF underlies of cerebellar learning^{1;71;103}. It was initially stated that only depression (long term depression: LTD) was the process occurring at these synapses. Later the complementary mechanism to LTD required to prevent saturation and allow reversal of motor learning, that is, potentiation (long term potentiation: LTP) of PF-PC synapses was also demonstrated^{91;136}. Thus, bidirectional plasticity at PF-PC synapses driven by the CF input seems to be behind learning in the cerebellum^{23;98}.

Although the PF-PC LTD/LTP learning hypothesis has been widely defended and is relatively matured⁹⁸, other hypotheses have also been debated⁹⁵ and encouraged by experimental demonstrations that motor learning proceeds in the absence of LTD^{139;161}. The motor timing hypothesis⁹⁵ states that the CF exerts a rapid (phasic) signaling at PCs to override whatever the cells are doing and generate a strong activation resulting in a well timed inhibition of the cerebellar nuclei. This hypothesis is also supported by the fact that the cerebellum responds to inputs extremely fast (in about 10 ms), 1-2 orders of magnitude faster than the cerebral cortex²⁵. In this context, and because the ability of the cerebellum to coordinate movement sequences, it has been considered as a timing machine, rather than a learning machine⁹⁵. Nonetheless, the motor learning hypothesis remains to be the most popular hypothesis.

Cerebellar models for engineering applications

From the very early cerebellar model articulation controller (CMAC) proposed by James Albus² (**Fig. 1.3**) back in the seventies as a biologically inspired neural network and table-lookup controller for motor control for robotic manipulators, computational models of the cerebellum and their successful interpolation into engineering applications have extensively been reported. These models exploit the learning capabilities of the cerebellum to provide adaptability to their applications. Commonly, the PF-PC synapses are the loci for plasticity

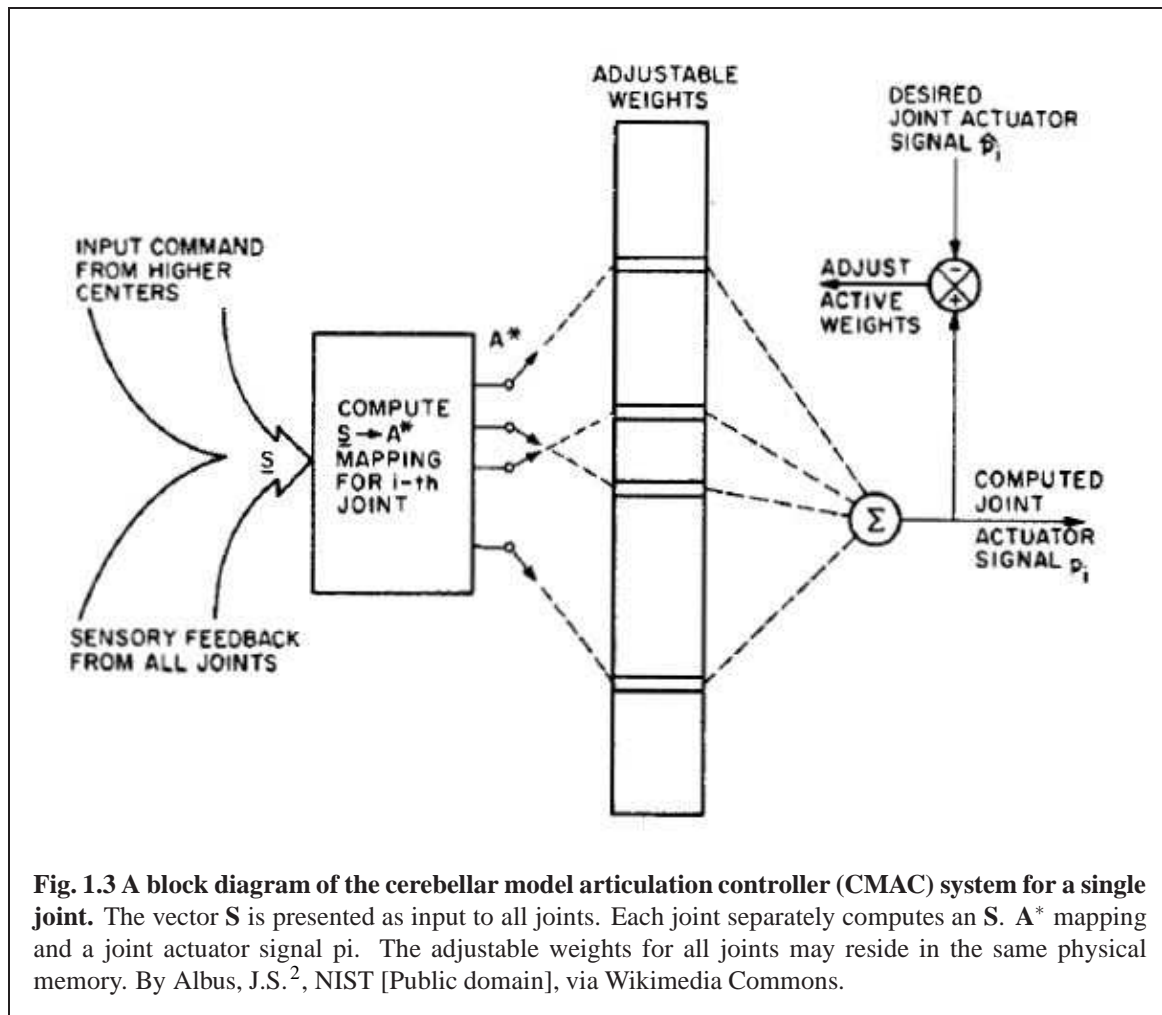


Fig. 1.3 A block diagram of the cerebellar model articulation controller (CMAC) system for a single joint. The vector S is presented as input to all joints. Each joint separately computes an $S \rightarrow A^*$ mapping and a joint actuator signal p_i . The adjustable weights for all joints may reside in the same physical memory. By Albus, J.S.², NIST [Public domain], via Wikimedia Commons.

driven by the CF input mimicking the mechanism of cerebellar motor learning. Applications range from control of a simulated eye plant⁸³, control of pneumatic muscles⁹⁰, control of robotic arms^{18;39;46;81;165}, control of biped robots⁹³, trajectory-tracking for mobile robots^{30;73}, and inverted pendulum systems^{124;135}.

These models have provided evidence of cerebellar capabilities in real world applications, however, they do not exploit thoroughly the architecture of the cerebellar microcircuit. It is common among the architecture of these models to find a partial representation of the cerebellar cortex including only GOs, GCs, and PCs, obliterating the role of the non traditional cerebellar neurons such as LU, and UBC. Similarly, several recurrent synaptic connections have been neglected such as the connection between BAs and GOs, LUs and GOs, and BAs and PCs. These neurons and connections are critical to understand the processing of information at the cerebellum. Lastly, one characteristic of the cerebellum that has barely been explored is its bi-hemispheric structure, which has been proposed to be

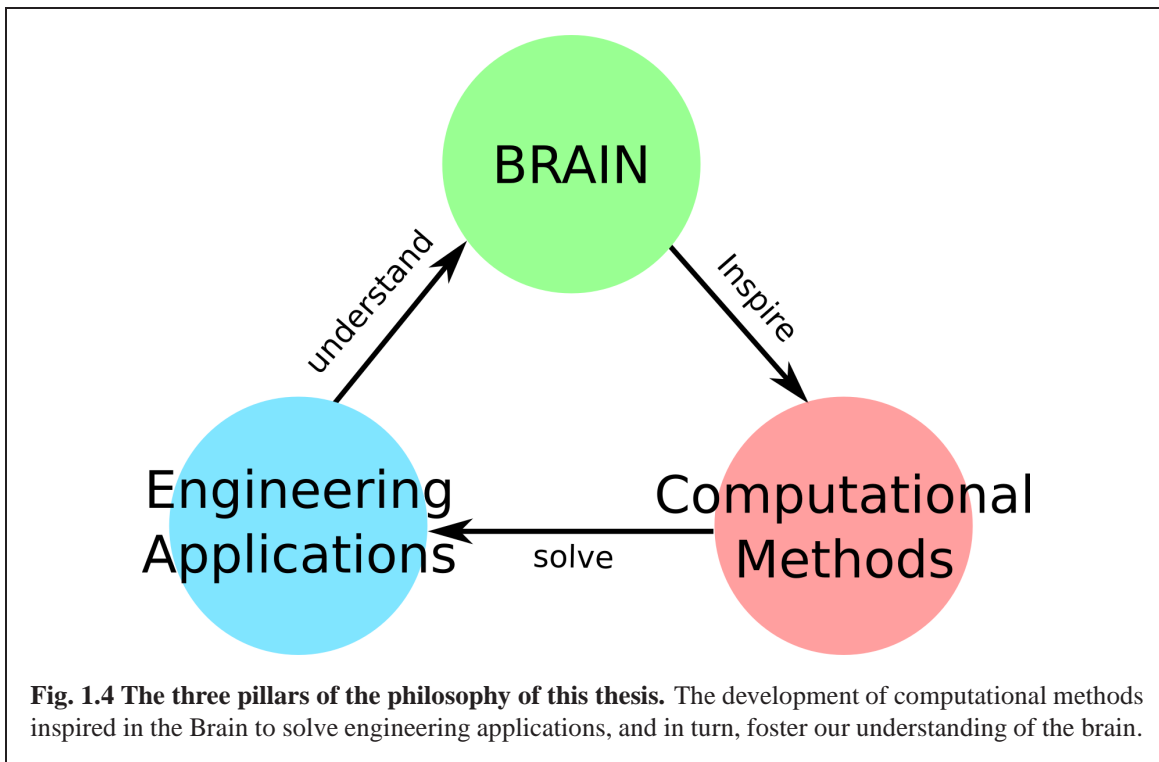
critical in asymmetrical motor adaptation among other cerebellar functions.

1.5 Motivation

Thus far the context of this thesis has been presented, yet the motivation behind is to be clearly stated. The pursue of such purpose, in a concise manner, is the core of the next two paragraphs.

The motivation of this thesis is two-fold. On one hand, the accurate localization of the STN in the BG for implementation of the electrode of the DBS during treatment of Parkinson's disease, and the more general adaptive control of robots are two engineering applications that could be solved with computational methods inspired in the BG and the cerebellum themselves. Developing an objective, deterministic and automatic computational method for identification of the BG during the surgery for Parkinson's disease translates in higher chances for the neurosurgeon at the moment of establishing the proper location for implanting the DBS's electrode. It follows that by reducing the uncertainty and subjectivity in the DBS procedure, the outcomes of the procedure could be maximized to reduce the motor symptoms related with the Parkinson's disease. Quality of life of parkinsonian patients could be further improved. In a similar way, the challenges in adaptive control of robots, which are in many cases reduced forms of control systems already solved in the brain, could be worked out by developing computational models inspired by the brain. In particular, the cerebellum is a very attractive neural structure for modeling because of its homogeneity, learning capabilities, and involvement in motor control, motor learning, and coordination.

On the other hand, solving engineering applications with computational models inspired by the brain could also be used to deepen our understanding of the brain itself. In many opportunities, computational models of the brain has been used to investigate questions related to the functioning of the brain from the molecular level at neuronal synapses to higher levels such as consciousness³⁷. Computational models help us make sense of the vast complex data available currently from neurophysiological and behavioral experiments. By incorporating engineering applications into the equation, additional explanations and predictions about the brain could be generated. To wrap-up, the motivation of this thesis is *the development of computational methods inspired in the Basal Ganglia and the cerebellum to solve engineering applications in neural signal processing and robot control, and in turn, provide explanations and hypotheses about the signal processing carried out in these two brain structures.*



1.6 Scope of this thesis

This thesis focuses on two structures of the brain tightly coupled, involved in motor control, coordination and learning. The Basal Ganglia and the cerebellum. The philosophy through this thesis, as mentioned above, follows the three pillars shown in **Fig. 1.4**, according to which by developing computational methods inspired in these brain areas engineering applications can be solved and in turn, by using engineering applications we can learn more about the Basal Ganglia and the cerebellum. In this context, this thesis is organized as follows (a graphical summary is shown in **Fig. 1.5**).

Chapter 2 shows the development of a novel computational method for analysis of neural activity from the BG with the purpose to automatically identify the STN. This is important because it aids the implantation of the electrode of the DBS during treatment of advanced cases of Parkinson's disease. We show that a new wavelet transform inspired by the neural data acquired from the BG (i.e., MER signals) is adapted by means of an genetic algorithm approach, allowing the discrimination of four structures in the BG, including the STN. We show that 3D feature spaces computed from the new wavelet's coefficients can be constructed to provide a visualization tool of the BG neural activity, that could be used as an intraoperative tool to support the surgery for DBS implantation.

In **Chapter 3** we embark upon the cerebellum. In this chapter, a detailed description of the realistic neuronal network model of the cerebellum is presented and its application into classical control is tested. This chapter illustrates the versatility of the cerebellar model and exemplify how to integrate it into feedback control loops to improve the control performance obtained with classical controllers. To this end, three different control plants are considered including a direct current (DC) motor, a two-wheel balancing robot, and a simulated quadcopter. Further details about the architecture, which is developed in LabVIEW (National Instruments, Austin, TX) is described in **Appendix A**.

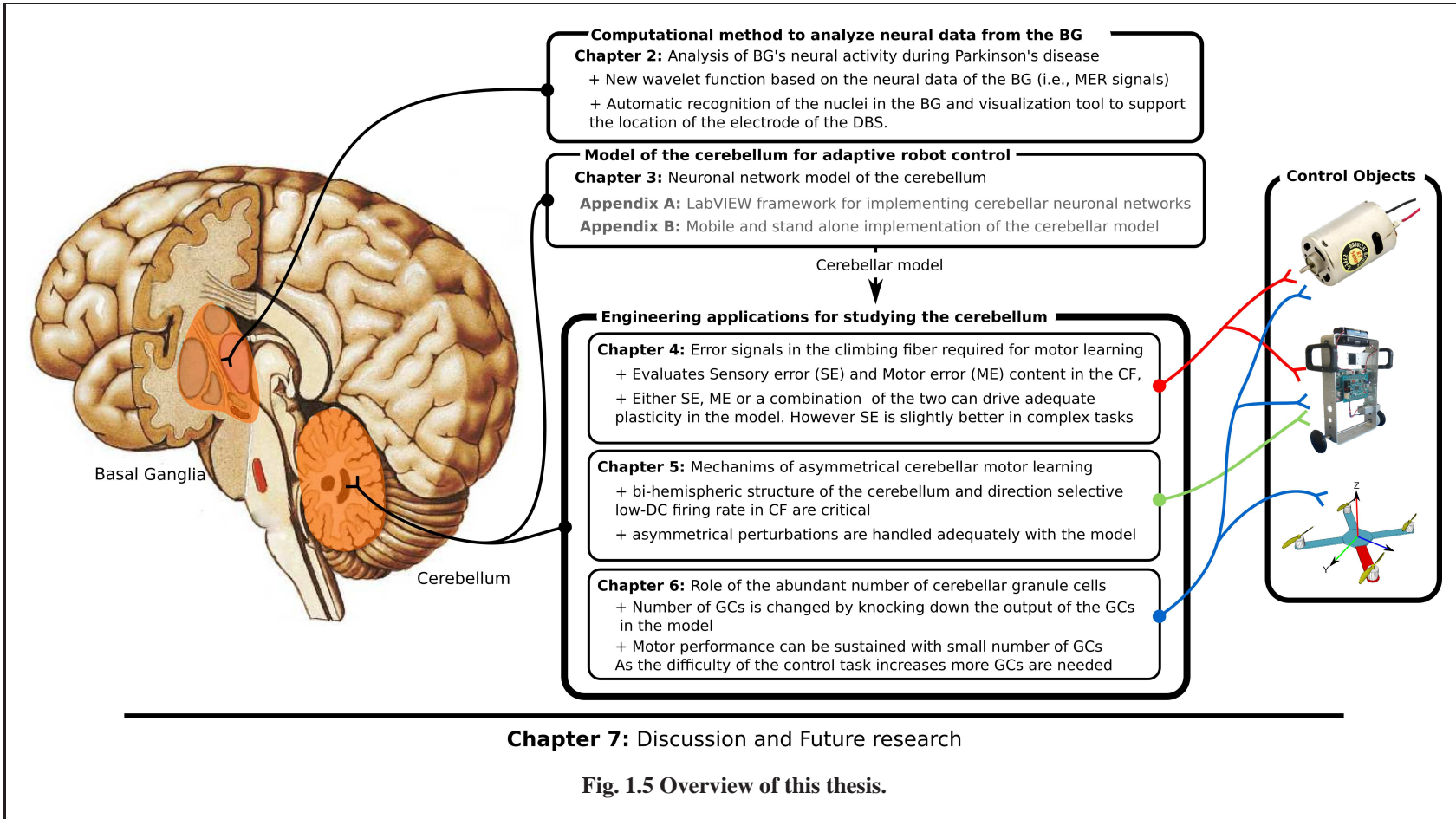
Chapter 4, 5, and 6 attempt to solve three unanswered questions about the cerebellum with the help of the model developed in **Chapter 3** during engineering applications. First, **Chapter 4** focuses on the type of error information carried in the CF. It is important to clarify the type of error because of the critical role of the CF input in cerebellar motor learning. There have been wide debates about this feature of the CF, resulting in two major hypotheses defending either sensory error (SE) or motor error (ME) content in the CF. The cerebellar model allows us to manipulate precisely the type of error conveyed in the CF and evaluate the behavioral and neural consequences during control of a simple (the DC motor) or a complex (the two-wheel balancing robot) control plant. We show that learning in the model is adequately driven by SE, ME, or a combination of the two during all the control scenarios tested. However, during the complex control task using SE resulted in higher performance. Behavioral consequence in the performance of the control plants evidences the differences between using SE and ME, whereas the neural consequences point to the neural mechanism that produces the differences between the CF error contents.

The second question, tackled in **Chapter 5**, is the mechanisms of asymmetrical cerebellar learning. The cerebellum is capable of adaptively compensating for changes produced in the muscle plants, or artificial conditions produced in the laboratory by exerting asymmetrical adaptation. Using the cerebellar model during control of the two-wheel balancing robot we explored this question by imposing asymmetrical conditions in the robot. We show that two features in the model are sufficient to produce asymmetrical adaptation. First, a bi-hemispherical structure, and second, a CF with direction sensitivity and low-DC firing rate content. We show that an uni-hemispheric cerebellar model cannot control the robot with asymmetrical perturbations, contrary to the bi-hemispheric model. Also we identify the critical role of the CF in balancing the contribution of the cerebellar hemispheres in the model by means of its low-DC firing rate.

The third question explored in **Chapter 6** concerns the role of the abundant number of GCs. We explore this question by selectively knocking down the output of the GCs in the model and analyzing the behavioral and neural consequences. The model presents

an unique framework to evaluate the GCs role in the cerebellar circuit in opposition to physiological experiments because the integrity of the cerebellar circuit can be sustained in the model while it is outstandingly difficult to achieve successful isolation of GCs in the real biological system. Results obtained during three different control scenarios with the DC motor, the two-wheel balancing robot, and the quadcopter show that increasing the number of GCs improves motor performance and robustness of the cerebellar model against structural changes. In particular, a model with the large number of GCs demonstrates to be highly stable even when the initial conditions and synaptic weights are changed.

To conclude and summarize, **Chapter 7** presents a general discussion of the findings of this thesis and future research.



2

Analysis of Basal Ganglia's neural activity during Parkinson's disease



EEP brain Stimulation (DBS) of the Basal Ganglia (BG) nuclei has become a standard treatment for advanced cases of Parkinson's disease. Among the different nuclei within the BG, the Subthalamic nucleus (STN) is the preferred target, although other zones are also feasible⁴⁷. Success in DBS procedures relies on the correct localization of the target nucleus, where the stimulation microelectrode is to be placed¹⁶⁴. For this purpose, stereotactic frames and T1-weighted magnetic resonance images are used for preoperative planning of the path to the target. Additionally, electrophysiological techniques that can provide intraoperative information, such as micro-electrode recordings (MER), are frequently used to refine the precision of targeting¹⁷⁰. In this chapter, we propose a computational method for automatic identification of the BG nuclei based on processing of MER signals with a novel optimal wavelet transform.

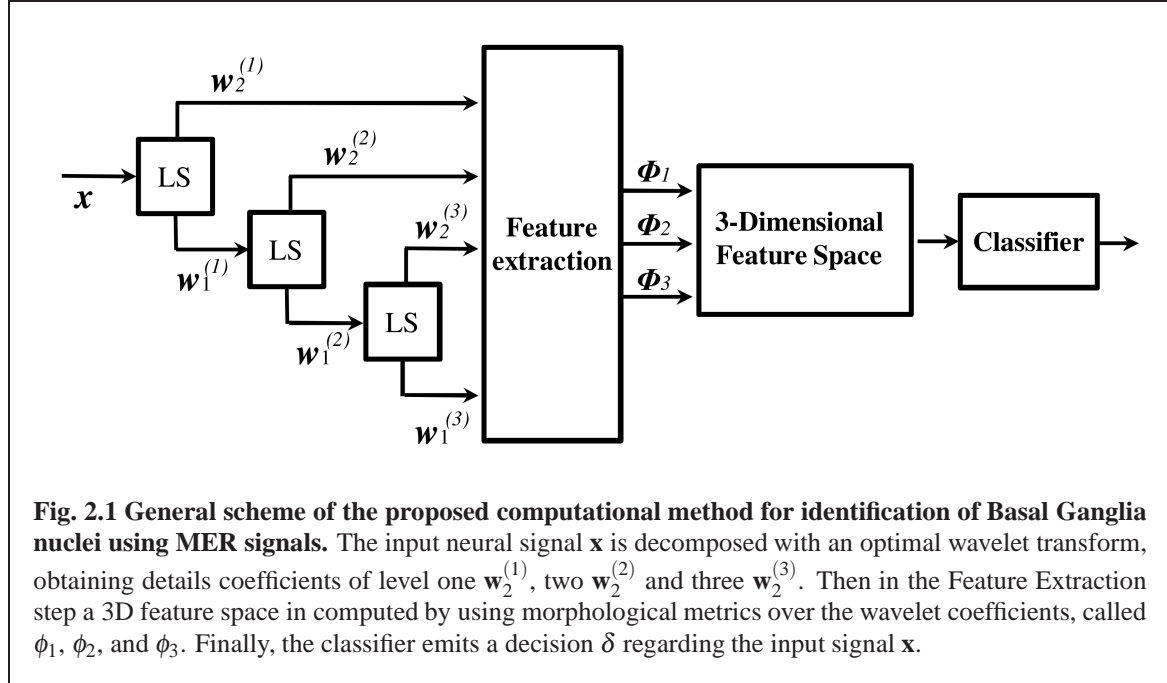
2.1 Introduction

Over the last two decades, investigators have made several attempts to improve localization of the STN during the implantation of DBS using MER signal analysis. Popular methodologies include the unsupervised classification of spikes based on wavelet transform and code-block searching²⁰, which employs an approach for single neuron's spike matching to preset neuronal patterns of the BG nuclei. Yet, these procedures are laborious and require the use of spike sorting algorithms before classification. Besides, there is need for the proper wavelet selection because of the similar activity generated by various nuclei in the brain^{53;137}. Other works have presented computational methods consisting of filtering the low frequency components of the MER signal, i.e., local field potential (LFP) component, to quantify the behavior of the STN^{88;154}. While this procedure has shown promising results at detecting different zones within the STN, results among other nuclei are troublesome. It has also been established that discriminant information can be directly extracted from the MER signal to recognize the STN along with its surroundings, hence, obtaining higher performance than spike or LFP based methods^{47;164}. Indeed, discriminant information is not only present in spikes or LFP, but also in background electrical noise. To the best knowledge of the authors, one approach that has not been considered is the gathering of characteristics from LFP, spikes, and neuronal noise simultaneously to gain higher differentiation among the BG nuclei, and as results better discrimination of the STN.

This chapter presents a computational method for identification of BG nuclei based on an optimal wavelet analysis, which is a customized realization of the discrete wavelet transform by using lifting schemes and genetic algorithms¹²⁹. This method is inspired in the BG itself and solves above issues by including a novel procedure for creating wavelet functions with unique properties for MER signal analysis. In addition, this approach allows creating 3-Dimensional neural space with maximum class separability that enables the use of basis classifiers from either LFP, spikes, or raw MER signals to discriminate the STN from other BG nuclei. Finally, the resulting 3D plot may be used as a visual assisting tool during DBS procedures¹²⁶.

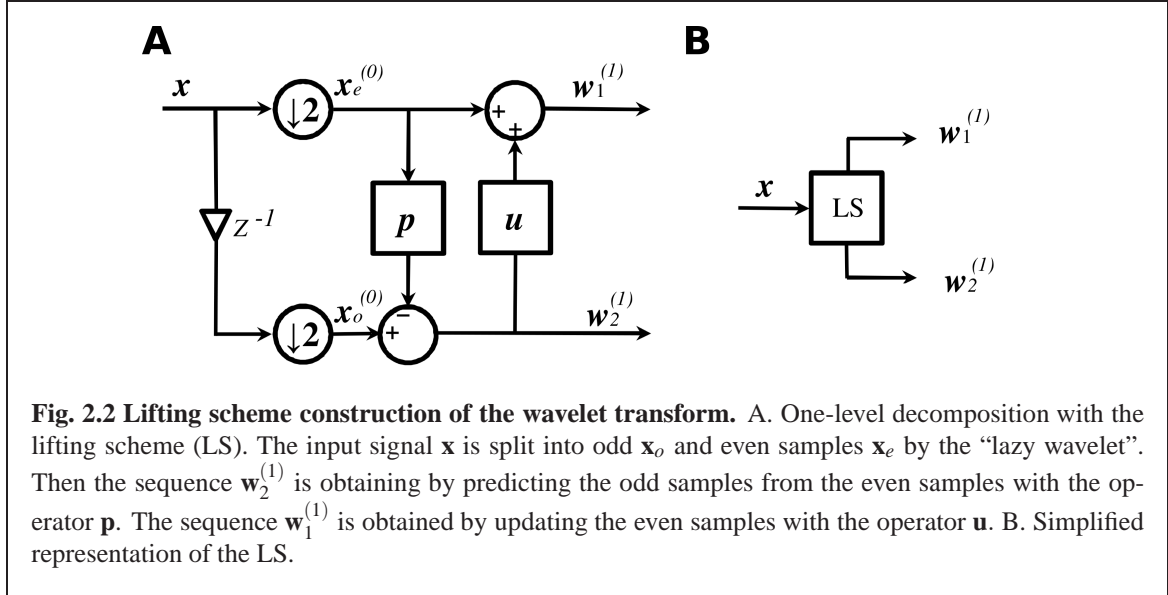
2.2 Methodology for automatic identification of Basal Ganglia's neural activity

The proposed computational method for identification of BG nuclei from MER signals comprises the following stages (see **Fig. 2.1**): firstly, the input MER signal $\mathbf{x} \in \mathbb{R}^{1 \times N}$ is



decomposed with the optimal wavelet transform, obtaining details coefficients of level one $\mathbf{w}_2^{(1)} \in \mathbb{R}^{1 \times N/2}$, two $\mathbf{w}_2^{(2)} \in \mathbb{R}^{1 \times N/4}$ and three $\mathbf{w}_2^{(3)} \in \mathbb{R}^{1 \times N/8}$. Secondly, in the feature extraction step, a 3D feature space is computed using a set of morphological metrics ϕ_1 , ϕ_2 , and ϕ_3 metrics over the detail coefficients \mathbf{w}_2 . Finally, the classifier emits a decision δ regarding the input signal \mathbf{x} and its origin at the BG.

At the beginning of the processing stage, the optimal wavelet is constructed via lifting scheme (LS) (shown in Fig. 2.2), which is built by applying the polyphase filter decomposition over the discrete wavelet transform¹⁴⁹. These schemes are regarded as a fast and efficient implementation of the wavelet transform. Moreover, the proper selection of the LS operators allows the construction of any orthogonal or bi-orthogonal wavelet. This characteristic is to be exploited during the optimization procedure (see below). During the LS decomposition the following three steps are involved: division, prediction, and update. In the division step, the input signal $\mathbf{x} = \{x[n] : n = 1, \dots, N\}$ is split into even samples $\mathbf{x}_e = \{x[2n] : n = 1, \dots, N\}$, as well as into odd samples $\mathbf{x}_o = \{x[2n - 1] : n = 1, \dots, N\}$. This procedure is also referred to as the “lazy wavelet”. Then in the prediction step, the operator \mathbf{p} is applied on $\mathbf{x}_e^{(l-1)}$ to predict $\mathbf{x}_o^{(l-1)}$ and for eliminating low order polynomials from \mathbf{x} , and thus, obtaining detail coefficients $\mathbf{w}_2^{(l)} = \{w_2^{(l)}[n] : n = 1, \dots, N/(2^l)\}$, which are described in Eq. 2.1.



$$\mathbf{w}_2^{(l)}[n] = \mathbf{x}_o[n] - \sum_{r=-N_p/2+1}^{N_p/2} p[r] \mathbf{x}_e^{(l-1)}[n+r], \quad (2.1)$$

where $\mathbf{p} = \{p[r] : r = 1, \dots, N_p\}$ are coefficients of the prediction operator, super-index (l) indicates the decomposition level, with $l = 0$ being the original signal \mathbf{x} , and N_p is the support of \mathbf{p} .

Next, in the update stage, an update on the even samples $\mathbf{x}_e^{(l-1)}$ is accomplished by using the update operator \mathbf{u} on the detail coefficients $\mathbf{w}_2^{(l)}$, and adding the result to $\mathbf{x}_e^{(l-1)}$. The update sequence $\mathbf{w}_1^{(l)} = \{w_1^{(l)}[n] : n = 1, \dots, N/(2^l)\}$ can be considered a rough view of \mathbf{x} , that is,

$$w_1^{(l)}[n] = x_e^{(l)}[n] + \sum_{j=-N_u/2}^{N_u/2-1} u_j w_2^{(l)}[n+j-1], \quad (2.2)$$

where $\mathbf{u} = \{u[r] : r = 1, \dots, N_u\}$ are coefficients of the update operator, and N_u is the support of \mathbf{u} . The concrete number l is fixed to be 3, matching the values suggested in similar works⁴⁷ and the frequency bands of interest in the MER signal’s spectrum.

After performing the wavelet decomposition, a set of morphological metrics¹⁶⁴ is computed from the detail coefficients \mathbf{w}_2 of level one to three in the feature extraction, thus, resulting in a vector of nine features $\Phi = \{\phi[n] : n = 1, \dots, 9\}$. The features included are:

$$\phi_1 = \frac{1}{2} \sum_{n=1}^{N-2} \max\{0, sgn(x[n+2] - x[n+1]) - sgn(x[n+1] - x[n])\}, \quad (2.3)$$

$$\phi_2 = \sum_{n=1}^{N-1} |x[n+1] - x[n]|, \quad (2.4)$$

$$\phi_3 = \sqrt{\frac{\sum_{n=1}^N x[n]^2}{N}} \quad (2.5)$$

where ϕ_1 is the peak's count, ϕ_2 is the curve length, and ϕ_3 is the root mean square amplitude of \mathbf{x} . Although, statistical moments or energy based metrics are also adequate descriptors, morphological metrics have shown to be discriminant for neural and non-neural activity in MER signals. Besides, they are also preferred because of their interpretability¹⁶⁴. The construction of the 3D feature space is based on an off-line selection of the best combination of three features, which produces the highest classification performance. At the end, the 3D space is fed into a classifier to get the corresponding decision δ .

2.2.1 Wavelet function optimization based on genetic algorithms

The core of the proposed method is the off-line optimization of the operators, \mathbf{u} and \mathbf{p} , as part of the LS implementation of the wavelet function based on genetic algorithms (GA). Each operator, \mathbf{p} and \mathbf{u} , can lead to its own wavelet function with unique time–frequency features¹⁷¹. In this sense, the following constrains are introduced to ensure that the associated wavelet function is suitable for linear phase, compact support, and perfect reconstruction, which are features desirable for a wavelet function. On one hand, the following symmetrical linear phase constraints are imposed⁵¹:

$$p[r] = p[-r+1], \quad r = 1, 2, \dots, N_p/2, \quad (2.6)$$

$$u[j] = u[-j+1], \quad j = 1, 2, \dots, N_u/2, \quad (2.7)$$

On the other hand, the filtering normalization conditions are as follow:

$$\sum_{r=1}^{N_p/2} p[r] = 1/2, \quad (2.8)$$

$$\sum_{j=1}^{N_u/2} u[j] = 1/4 \quad (2.9)$$

The off-line optimization procedure under the given constraints in Eqs. (2.6)-(2.9) follows the diagram shown in Fig. 2.3. This optimization is inspired in the MER signals acquired from the BG, so that the new wavelet function is fit for analysis of the MER signal

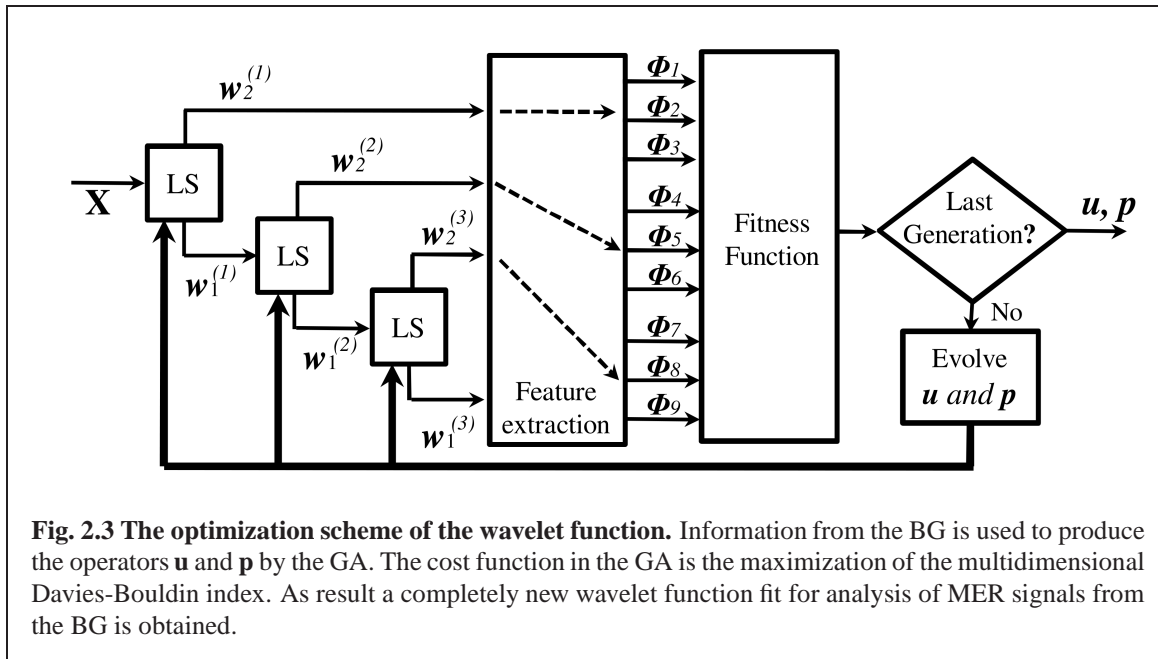


Fig. 2.3 The optimization scheme of the wavelet function. Information from the BG is used to produce the operators \mathbf{u} and \mathbf{p} by the GA. The cost function in the GA is the maximization of the multidimensional Davies-Bouldin index. As result a completely new wavelet function fit for analysis of MER signals from the BG is obtained.

itself. Firstly, a set of training MER signals \mathbf{X} is randomly selected from the database to supply the GA. \mathbf{X} should include patterns belonging to each type of BG nuclei to be detected. This requirement of the procedure is an important contribution of the present methodology since similar approaches for optimizing wavelet functions only consider either a matched signal or a representative prototype signal from the database^{17;53;171}. Secondly, each signal is decomposed up to level three with wavelet transform. As a result, detail coefficients $\mathbf{w}_2^{(l)}$ for $l = [1, 2, 3]$ are obtained. Then Φ is extracted from detail coefficients yielding a 9D feature vector. During the optimization, the whole set of nine features is used instead of the best three as used in the on-line method (Fig. 2.1). The reason for such a decision is that the GA based optimization procedure is to be fed with as much information as possible so that it can evolve the LS operators. Next, the fitness function for the GA is computed. In this work, a classification-oriented fitness function, namely, the Davies-Bouldin(DB) index²⁸ is used.

The DB index is a Euclidean distance that not only considers the inter-class distances, but the intra-class dispersion of each class as well. Thus, using DB index in the GA based optimization means that resulting LS operators maximize the separability among classes within the feature space¹⁶⁰. To adapt the DB index to the set of nine features obtained in the previous step, the multi-dimensional DB index (mDB) is used here. The mDB is based on the scatter matrices of the data, which require the computation of the class-to-class similarity, $R_{ij} = (D_{ii} - D_{jj})/D_{jj}$, where D_{ii} and D_{jj} are the dispersions of the i -th and j -th

classes, respectively, computed as follows:

$$D_{jj} = \sqrt{\frac{1}{N_j} \sum_{n=1}^{N_j} \left(\sum_{m=1}^d \|c[n]_{j,m} - \mu_{j,m}\|^2 \right)}, \quad (2.10)$$

Whereas D_{ij} is the Euclidean distance among the mean values, $D_{ij} = \|D_{ii} - D_{jj}\|$, where N_j is the number of MER signals belonging to the class j . The value $c[n]_{j,m}$ is the n -th sample of the j -th class over the m -th dimension, and $\mu_{j,m}$ is the mean value of class j over the m -th dimension. Here, $d = 9$. The fitness function mDB is accomplished through determining the worst case of separation for each class $i = [1, \dots, q]$, where q is the number of classes, and then, averaging these values, i.e.:

$$mDB = \frac{1}{q} \sum_{i=1}^q (\max_{i \neq j} R_{ij}). \quad (2.11)$$

Once the previous restrictions are defined, only $N_u/2 - 1$ and $N_p/2 - 1$ coefficients are optimized by the GA. Regarding the GA, the following five parameters must be selected: (i) the arithmetic operator, (ii) the mutation operator, (iii) the population scale, (iv) the number of generations, and (v) the bounds of iteration. Parameters (i) to (iv) can be set directly from literature¹⁷¹. The arithmetic crossover and no uniform mutation operators are employed as recommended¹⁷¹. And for the sake of simplicity, the population scale is set to be 20, whereas the number of generations is set equal to 50. The working iteration parameters of the GA are selected to range within the interval $[-0.5, 0.5]$, which are the possible values for the predictor and update coefficients that meet the normalization constraints (**Eq. 2.8** and **Eq. 2.9**).

2.2.2 Database of microelectrode recordings (MER) from the Basal Ganglia

Intraoperative recordings were made on unmedicated awake patients that underwent DBS implantation. Surgeries were carried out in the University General Hospital of Valencia, Spain. The recordings were labeled by both specialists in neurophysiology and electrophysiology, according to the reference stereotactic coordinates, visual and auditive inspection of the recording. The equipment used in the acquisition was the LeadPointTM Medtronic (Medtronics Functional Diagnostics, Minneapolis, MN). The sampling frequency was 24 kHz and 16-bit resolution and lasted 1 s. In total, there are 216 recordings coming from the following BG nuclei: 66 signals from the Thalamus (TAL), 25 signals from the Subthalamic

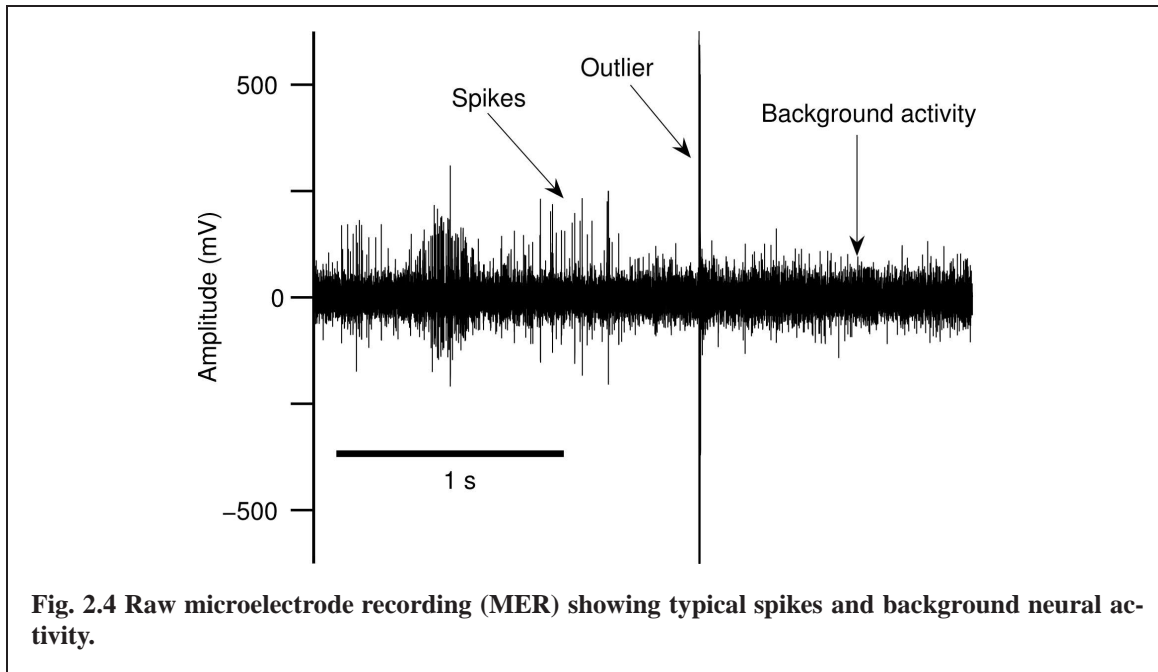


Fig. 2.4 Raw microelectrode recording (MER) showing typical spikes and background neural activity.

nucleus (STN), 38 signals from the Substantia Nigra pars Reticulata (SNR), and 87 signals from the Zone Incerta (ZI).

Raw MER signals were saved in digital files for off-line analysis, which have been performed using MATLAB (Mathworks, Natick, MA). LFPs are obtained by filtering the MER signals using a finite impulse response (FIR) equiripple low-pass filter of order 4000, with a passband of [0 – 140] Hz, and flat-shaped stopband. In the case of spike component, a FIR equiripple bandpass filter with stopband [0 – 470] Hz and [10.0 – 10.3] kHz, with passband [0.5 – 10.0] kHz, of the same order is employed⁸⁸. A typical MER signal is shown in **Fig. 2.4**.

2.3 Results

2.3.1 New wavelet function inspired by the neural activity of the Basal Ganglia

The tuning of the proposed methodology relies on the GA based optimization of both operators, \mathbf{p} and \mathbf{u} . A set of 62 MER signals, one-third of signals from each class in the database, is randomly fed to the GA. To avoid overspecialization in the results of the GA, this experiment is repeated ten times, thus, generating ten new wavelet functions. The best wavelet function is selected as the one with the largest cost function (**Eq. 2.11**). **Fig. 2.5** shows the

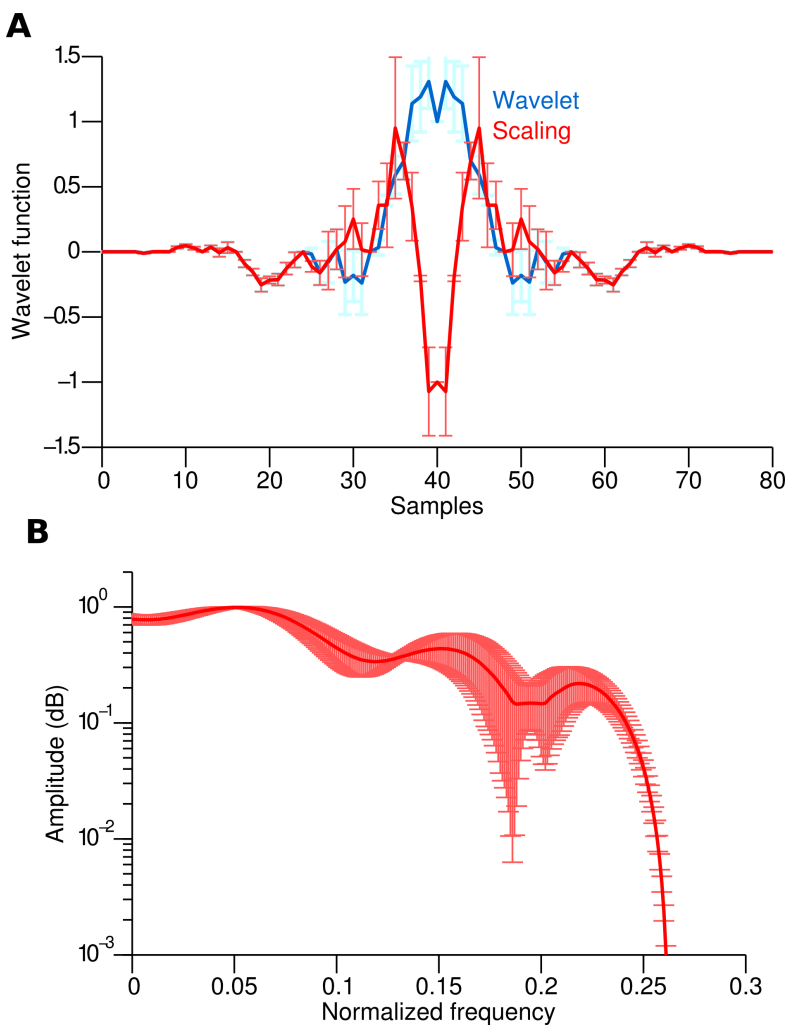


Fig. 2.5 Optimal wavelet function for analyzing MER signals. A. Temporal response of the wavelet and scaling functions associated with $\mathbf{u} = [0.0278 \ -0.2070 \ 0.4292 \ 0.4292 \ -0.2070 \ 0.0278]$ and $\mathbf{p} = [-0.0584 \ -0.0756 \ 0.6340 \ 0.6340 \ -0.0756 \ -0.0584]$. B. Frequency spectrum of the optimal scaling function. Frequency axis has been normalized by π . Error bars show ten different results obtained with ten different initializations of the GA procedure.

optimized wavelet functions and the frequency spectrum of the operator \mathbf{u} .

2.3.2 Comparison of the classification performance with the new and classical wavelets

For the sake of comparison, classification performance attained with several standard and the new wavelet is presented here. As the core of the proposed methodology is not the classification stage, but the characterization, a simple linear Bayesian classifier is used because of

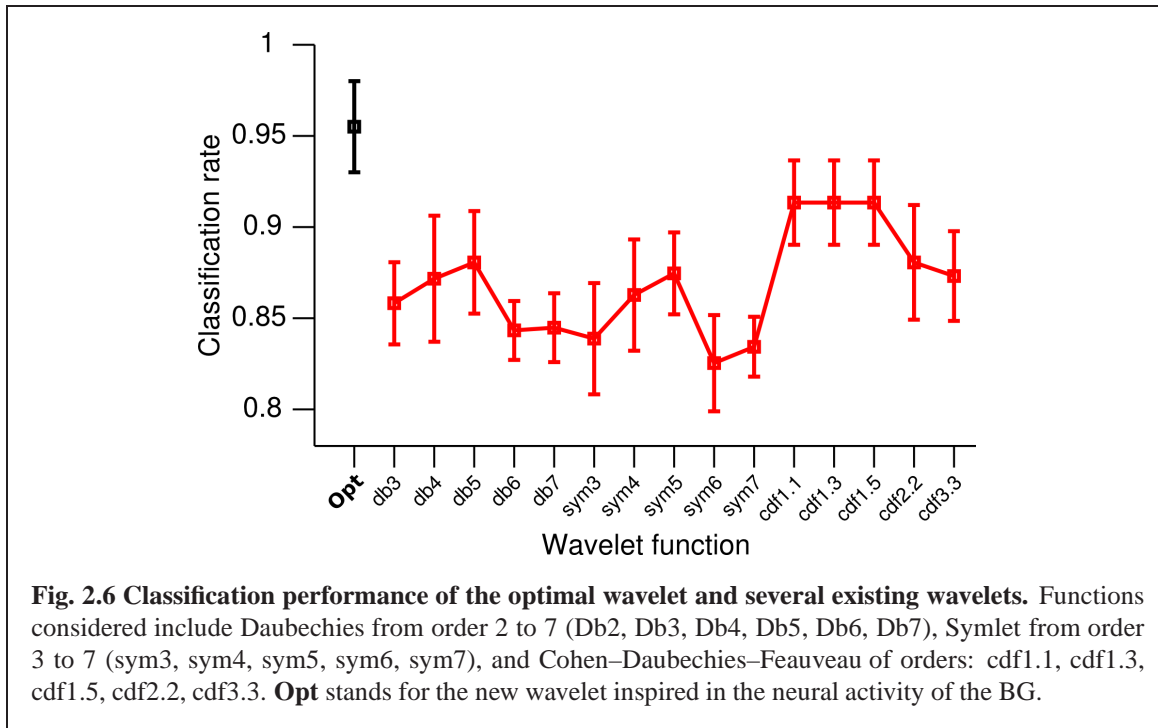


Fig. 2.6 Classification performance of the optimal wavelet and several existing wavelets. Functions considered include Daubechies from order 2 to 7 (Db2, Db3, Db4, Db5, Db6, Db7), Symlet from order 3 to 7 (sym3, sym4, sym5, sym6, sym7), and Cohen–Daubechies–Feauveau of orders: cdf1.1, cdf1.3, cdf1.5, cdf2.2, cdf3.3. **Opt** stands for the new wavelet inspired in the neural activity of the BG.

its simplicity of implementation and because it does not improve the classification potential of the input data. The k -fold cross-validation approach is used to manage the database. That is, the database is randomly divided into two subsets: the training and validation. The former set comprises 149 patterns, while the remaining 67 patterns are related to the latter set, i.e., 70/30 partition. There is no overlapping between the sets. The standard wavelets are taken from the literature⁴⁷, including wavelet functions of the families Daubechies, Symlet, and Cohen-Daubechies-Feauveau (CDF). As shown in **Fig. 2.6**, the classification rates obtained with the standard wavelets are lower than the one achieved by the new optimized wavelet. Particularly, differences ranged from 3% with the CDF family (order 1.5 and 3) up to 10% when using the rest of the considered standard wavelets. Lowest outcomes may be explained because families Daubechies, and Symlet do not adequately represent the MER signal dynamic. The CDF wavelets that share some features with the customized wavelet, e.g., linear phase, filter normalization, and compact support, presented the highest classification among the classical wavelets tested, yet lower than with the optimal wavelet.

Different metrics may be extracted from the wavelet coefficients, however, only the best combination of three features is to be selected to become a visualization tool in a 3D feature space. The selection was made off-line based on classification performance. As a result, the peak's count of $w_2^{(1)}$, the curve length of $w_2^{(2)}$, and the RMS value of $w_2^{(3)}$ became the best combination among the 504 possible combinations. This feature space is shown in **Fig. 2.7**,

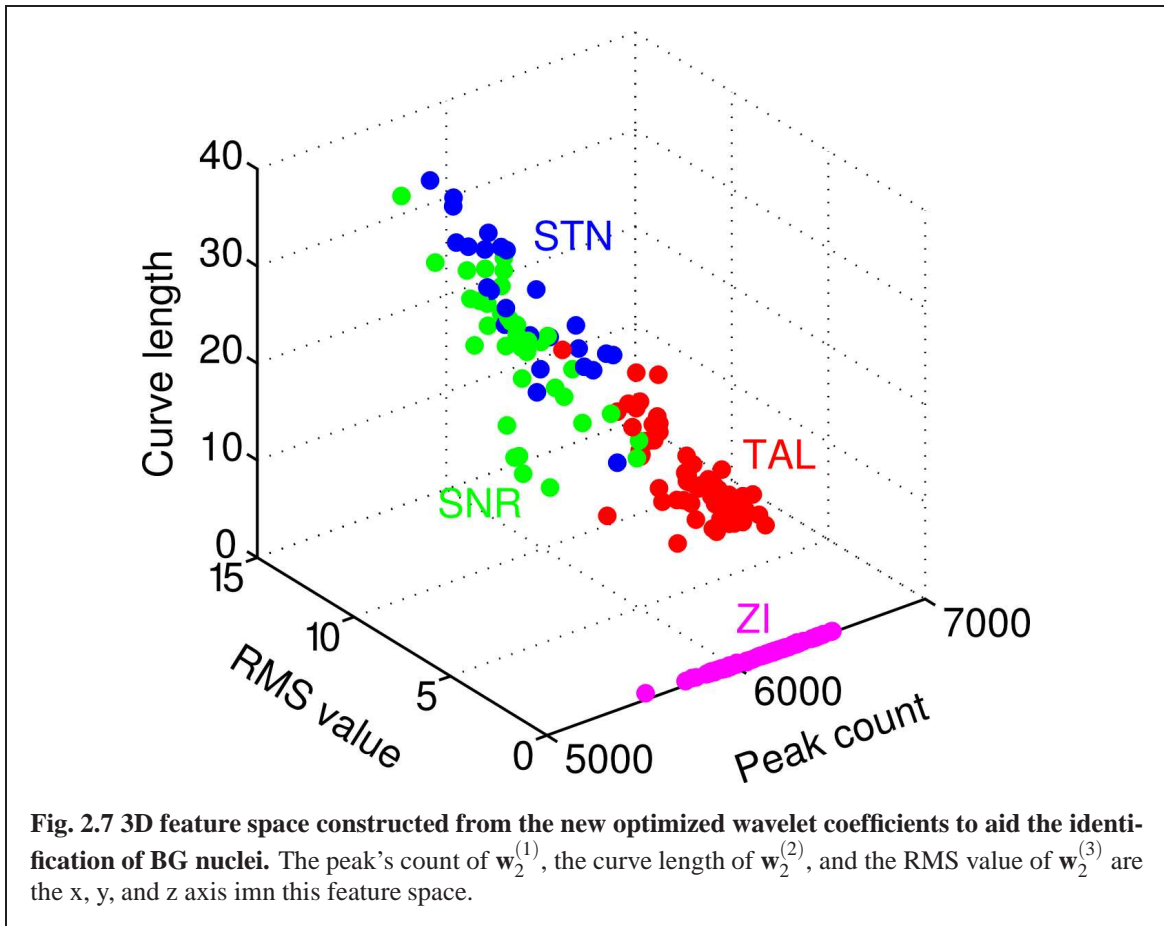


Fig. 2.7 3D feature space constructed from the new optimized wavelet coefficients to aid the identification of BG nuclei. The peak's count of $w_2^{(1)}$, the curve length of $w_2^{(2)}$, and the RMS value of $w_2^{(3)}$ are the x, y, and z axis imm this feature space.

presenting typical characteristics of the neural activity in the BG nuclei. In particular, it can be seen that the quiet zone ZI is reliable confined to one area of the 3D space, having low RSM and peak's count values. Since the feature measurements, generally, are presumed to have discriminatory power among ZI/quiet zone and STN/SNR/TAL, the activity from these regions is distant from each other and well separable. The SNR/SNR zones display the most challenging task for the classifier and reflect the difficulty in discriminating between the neural activity of glutamatergic and GABAergic neurons in these nuclei. The neural activity from the TAL relay neurons are located in the middle/lower part of the 3D space and can be easily separable from the other BG nuclei.

2.3.3 Automatic identification of Basal Ganglia with MER, LFP and spikes

The aim of this experiment is to determine the discrimination potential of LFP, spikes, and raw MER using the morphological features extracted from the new wavelet's coefficients.

Table 2.1 Classification in terms of sensitivity (E) and specificity (F) using LFP, spikes, and raw MER signals 3D spaces generated with the optimal wavelet function.

		TAL	STN	SNr	ZI
LFP	E	65.00±7.82	41.25±18.68	32.50±13.86	100.00±0.00
	S	90.00±3.62	87.12±6.65	91.27±4.68	93.25±2.9
Spikes	E	95.00±4.08	85.00±16.43	82.50±7.30	100.00±0.00
	S	97.87±2.01	97.80±1.40	96.36±2.84	100.00±0.00
Raw MER	E	96.50±3.37	88.75±12.43	85.83±7.91	100.00±0.00
	S	97.87±2.01	98.47±1.25	97.45±2.60	100.00±0.00

Classification performance using the linear Bayesian classifier is given in terms of sensitivity (E) and specificity (S), corresponding to the percentage of MER signals belonging to “a” nucleus correctly classified as “a” and the percentage of MER signals different from “a” correctly classified as not belonging to “a”, respectively. **Table 2.1** summarizes the results using LPF, spikes, or the MER signal.

The most discriminant 3D space is generated with the raw MER signal, that is, unfiltered. The number of missed observations in this feature space is less than 3%, while the rate of correctly classified observations is higher than 95%. These rates suggest that splitting the microelectrode signals into its components of high and low frequency reduces the power of discrimination of the BG nuclei. Therefore, the MER recordings do not include filtering during the following experiments.

Table 2.2 shows classification performance of the bi-class problem, that is, classification of one nucleus against another nucleus. The second column shows the Area-Under-the Curve (AUC) of the receiver operating characteristic (ROC) curve when estimated for different paired nuclei, which are typically found in the trajectory to the STN during the DBS procedure¹⁶⁴. An AUC value close to 1 means perfect classification, whereas the contrary happens with AUC value equal to 0. Classes TAL/STN/SNR versus ZI present near perfect classification. TAL/ZI case shares the same position at the peak’s count axis since both nuclei present majority background neuronal noise. As a result, the peak’s count feature failed the statistical test, which is presented in the third column (p-value). In the case of STN versus SNR, the test outcome for each feature should be assumed as not statistical significant because of reduced representative data, that is, the low quantity of samples in both cases and the similar dynamics in both nuclei. However, as in the previous case, the 3D space allows the classifier to discriminate both classes with accuracy superior to 85%.

2.4 Discussion

The following remarks are made in order to allow the discussion to be more organized:

Table 2.2 Classification and statistical analysis of the bi-class classification problem

Classes	Feature	AUC	<i>p</i> -value	95% C.I.	
TAL vs Zi	Peak's Count	0.539	0.198	0.44783	0.63176
	Curve Length	1.000	0.000	100.000	100.000
	RMS	1.000	0.000	100.000	100.000
STN vs Zi	Peak's Count	0.932	0.000	0.887	0.977
	Curve Length	1.000	0.000	100.000	100.000
	RMS	1.000	0.000	100.000	100.000
STN vs SNR	Peak's Count	0.627	0.035	0.488	0.765
	Curve Length	0.661	0.009	0.526	0.795
	RMS	0.580	0.136	0.437	0.722
SNR vs. Zi	Peak's Count	0.953	0.000	0.905	100.000
	Curve Length	1.000	0.000	100.000	100.000
	RMS	1.000	0.000	100.000	100.000

1. The first observation is that the raw microelectrode recording proved to be a better source of discriminant information to identify the BG nuclei than its components. The 3D space constructed with the raw MER signals depicts the best separability among four BG nuclei.
2. Despite the abundant repertoire of wavelet functions in the literature, selection of the appropriate wavelet to the application is one of the most important tasks when using the wavelet transform. In this work, rather than selecting one of the existing wavelet a completely new wavelet was built using the neural signal from the BG itself. The performance of the new wavelet was higher than the one reached with other standard wavelets.
3. The classification-oriented fitness function used in the GA process, which is an extended form of the one-dimensional case presented in¹⁶⁰ to the multidimensional case, provided the computational method with wavelet operators that produces 3D spaces with maximum class separability.
4. What is more, friendly visualization tools of the neural activity of the BG are constructed by extracting 3D feature spaces from the wavelet coefficients and might be possible to use it as a supporting tool during the procedure for DBS implantation.
5. Finally, the complexity of the proposed methodology was measured. Tests were carried out on a computer equipped with an Intel Core 2 Due CPU processor @3.00 GHz, memory RAM 3.4 GiB, MATLAB 7.6.0.324(R2008b) and Ubuntu 10.04 (Linux kernel 2.6.32-22 generic). Execution times were measured using the profile tool in MATLAB. For reference purposes we used a computational unit (CU) as the time that takes to add 100 times a matrix of 10×10 filed with ones. This CU in above computer was

Table 2.3 Computational time of the proposed computational method. $CU = 0.0010$ seconds on the test-bench computer.

Procedure/stage	CU
LS Block	119
Wavelet decomposition (LSx3)	357
Feature Extraction	15
Classification	8

0.0010 s on average. Computational time of the proposed method is given in terms of this unit and for ten tests carried out.

As shown in **Table 2.3**, the computational time of the proposed method is mainly due to wavelet decomposition with the LS block. In general, for an 1 s signal our approach gives a decision in about 1.90085 s. Additionally, the LS Block complexity is $\mathbf{O}(N)$ ¹⁴⁹ since on every decomposition stage only sums and one order polynomial multiplications are performed on half the input signal due to the down sampling operation. Regarding the other stages, the feature extraction is also $\mathbf{O}(N)$ complex. Additionally, once the classifier is trained its complexity is reduced to multiplications. This stage is also $\mathbf{O}(N)$ complex. In overall the complexity of the proposed methodology is $\mathbf{O}(N)$.

In this chapter a computational method for identification of BG nuclei in Parkinsonian patients based on a novel wavelet optimization was presented. It takes inspiration on the neural activity of the BG to create a new wavelet function especially suitable for analyzing the BG activity. This method introduces several improvements. Firstly, construction of unique mother wavelets from the signal's information itself with adaptable spectral characteristics that outperform several existing wavelet in about 5% in classification. Secondly, identification performance of four BG nuclei can be achieved with 95% of confidence. Thirdly, interpretability is gained with the 3D feature spaces generated. Then, low computational cost is obtained with the lifting schemes based wavelet decomposition and basic classifiers. Finally, pre-filtering stages are not included since the raw MER recording provides more information than LFP and spikes^{121;126}.

3

Model of the cerebellum for adaptive robot control

COMPUTATIONAL models inspired by the brain have been shown to provide both efficient solutions to engineering problems and insights into the function of the biological system^{79;123}. One brain structure extensively studied and modeled is the cerebellum⁶⁹, which is involved in cognition^{102;115;153} and in motor learning and coordination^{57;69;101;145;152}. Here we present a neural network model of the cerebellum with realistic climbing fiber input and learning algorithm. The cerebellar model is developed with the purpose of providing similar capabilities as the real cerebellum in engineering applications such as robotics. In this chapter, the cerebellar model is employed in three different control scenarios including two real control plants with one and two degrees of freedom (DoFs) and a simulated plant with six DoFs. Results showed that the cerebellar model adapts and controls all of the plants considered, outperforming a classical controller. Later in the next chapters we aim at exploring some unanswered questions in the cerebellar research literature by retrospectively analyzing the cerebellar model.

3.1 Introduction

Computational models of the cerebellum and their successful interpolation into engineering applications have extensively been reported. Moreover, applications in robotic setups are also prominent and include control of the eye plant⁸³, pneumatic muscles⁹⁰, robotic arms^{39;46;81}, mobile robots^{63;158}, and inverted pendulum systems^{124;135}. One characteristic commonly exploited in these models is the plasticity of the cerebellum. The cerebellum adaptively changes the efficacy of its synaptic connections given the activity of a teaching signal⁷⁰. By incorporating a plastic mechanism, cerebellar models have shown adaptable capacities as well.

This chapter presents a neuronal network model of the cerebellum as an adaptive controller for engineering applications. In particular, we test the control of real world and simulated plants with different degrees of freedom and show that the cerebellar model adapts to the control task and outperforms a classical proportional controller.

3.2 General description of the neuronal network model of the cerebellum

Inspired by the neuronal circuit of the cerebellar cortex, we have developed a neuronal network model of the cerebellum^{122;123} (**Fig. 3.1A**). As the cerebellar cortex has a homogeneous structure all over its volume, and it has vast connections to the most important structures of the central nervous system, including brain-stem, spinal cord, BG, and Thalamus, its basic learning algorithm is sometimes called a generic algorithm of the cerebellum^{25;69}. We focused on the vestibulocerebellum because they have been widely studied in anatomy and physiology⁶⁹. This model is freely available via a GIT repository^a and its architecture is presented in detail in **Appendix A**. Briefly, the network contains the same neuron types and synaptic convergence/divergence ratios reported in the cerebellar cortex (**Table 3.1**, **Fig. 3.1B**). Principally the cerebellar model includes granule cells (GCs), Golgi cells (GOs), basket and stellate cells (BCs), and Purkinje cells (PCs). Nonetheless there are other less studied cerebellar cells that might have a role in the cerebellar algorithm such as Lugano cells and unipolar brush cells³³. Synaptic connectivity includes excitatory projection from mossy fibers (MFs) to GCs and GOs, and from GCs to BCs and GOs via parallel fibers (PFs) of the GCs. Inhibitory feedback loop between GCs and GOs, and BCs and GOs, and mutual inhibitory loop between BCs and PCs^{34;97;112;124} (**Fig. 3.1B**). A uni-hemispheric

^a<https://bitbucket.org/rdpinzonm/the-bicnn-model>

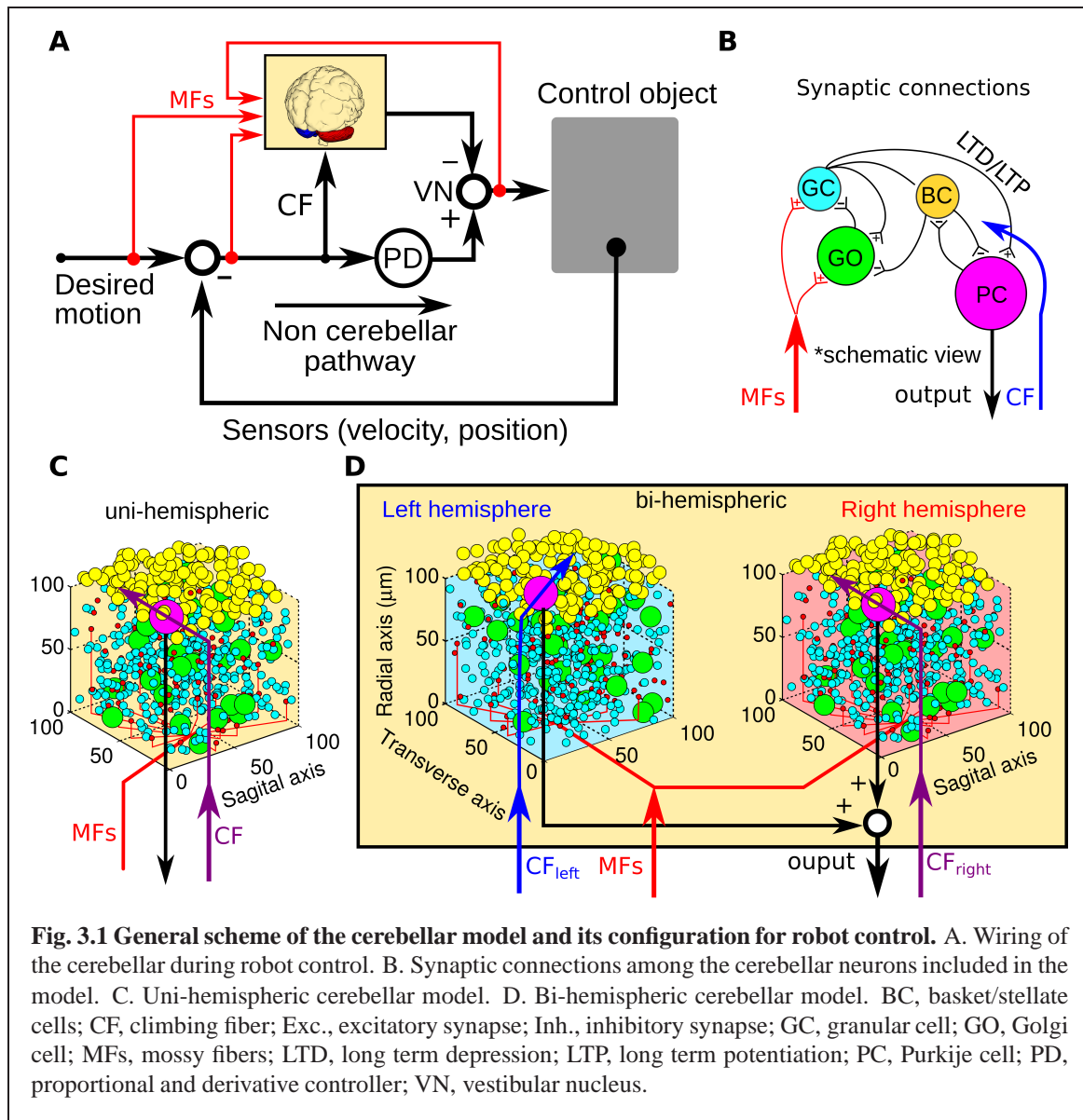


Fig. 3.1 General scheme of the cerebellar model and its configuration for robot control. A. Wiring of the cerebellar during robot control. B. Synaptic connections among the cerebellar neurons included in the model. C. Uni-hemispheric cerebellar model. D. Bi-hemispheric cerebellar model. BC, basket/stellate cells; CF, climbing fiber; Exc., excitatory synapse; Inh., inhibitory synapse; GC, granular cell; GO, Golgi cell; MFs, mossy fibers; LTD, long term depression; LTP, long term potentiation; PC, Purkje cell; PD, proportional and derivative controller; VN, vestibular nucleus.

(**Fig. 3.1C**) and a bi-hemispheric (**Fig. 3.1D**) configuration of the model are presented as examples. The cerebellar model is incorporated into standard feedback control loops (**Fig. 3.1A**, PD) by extracting MFs and the CF from the error signals, the motor command sent to the control plant. The command to the control plant is computed at the VN as the subtraction of the PCs firing rate from the non-cerebellar pathway activity. The controller in the standard loop operating in parallel with the cerebellar model fill the role of the non-cerebellar pathway in the control loop in the real cerebellum. Mathematical models describing each neuron follow classical firing rate models^{122;124}, according to which the cell output is computed as the weighted summation of inputs passed through an activation function as follow:

Table 3.1 Convergence and divergence synaptic ratio of the cerebellar model

	Num. Cells	Divergence	Convergence	Ref.
Mossy fibers (MF)	562			
Golgi (GO)	56			
Granular (GC)	8192			
Basket/Stellate (BC)	548			
Purkinje (PC)	30			
MF → GC		1:59	4:1	69;143
MF → GO		1:7	66:1	"
PF → GO		1:12	1639:1	"
GO → GC		1:586	4:1	"
PF → BC		1:3	41:1	69;96
PF → PC		1:4	1024:1	69
BC → PC		1:7	110:1	143
PC → BC		1:55	3:1	138
BC → GO		1:3	28:1	33

*Number of MF inputs to the cerebellar model changes with the control plant.

$$\mathbf{x}_{\text{GC}} = \mathbf{y}_{\text{MF}} \cdot \mathbf{W}_{\text{MF-GC}} + \mathbf{y}_{\text{GO}} \cdot \mathbf{W}_{\text{GO-GC}} \quad (3.1)$$

$$\mathbf{y}_{\text{PF}} = \frac{1}{1 + e^{-\sigma(\mathbf{x}_{\text{GC}} - \mu)}} \quad (3.2)$$

$$\mathbf{x}_{\text{GO}} = \mathbf{y}_{\text{MF}} \cdot \mathbf{W}_{\text{MF-GO}} + \mathbf{y}_{\text{PF}} \cdot \mathbf{W}_{\text{PF-GO}} \quad (3.3)$$

$$\mathbf{y}_{\text{GO}} = \frac{1}{1 + e^{-\sigma(\mathbf{x}_{\text{GO}} - \mu)}} \quad (3.4)$$

$$\mathbf{x}_{\text{BA}} = \mathbf{y}_{\text{PF}} \cdot \mathbf{W}_{\text{PF-BA}} \quad (3.5)$$

$$\mathbf{y}_{\text{BA}} = \frac{1}{1 + e^{-\sigma(\mathbf{x}_{\text{BA}} - \mu)}} \quad (3.6)$$

$$\mathbf{x}_{\text{PC}} = \mathbf{y}_{\text{PF}} \mathbf{W}_{\text{PF-PC}} + \mathbf{y}_{\text{BA}} \mathbf{W}_{\text{BA-PC}} \quad (3.7)$$

$$\mathbf{y}_{\text{PC}} = \frac{1}{1 + e^{-\sigma(\mathbf{x}_{\text{PC}} - \mu)}} - 0.5 \quad (3.8)$$

where $\sigma = 8$, $\mu = 1/2$, $\mathbf{x}_{\text{GC}} \in \mathbb{R}_+$ is the activity vector of all GCs before being processed by the sigmoid activation function \mathbf{y}_{PF} (Eq. 3.2), $\mathbf{W}_{\text{MF-GC}} \in \mathbb{R}_+$, $\mathbf{W}_{\text{GO-GC}} \in \mathbb{R}_-$ are the

Table 3.2 Mossy fibers for each control plant

Object	Outputs (Sensors)	MFs	Scaling gain
DC motor	$\phi(t)$ shaft ang. pos. (rad)	1- ref. shaft ang. pos.	0.1 rad^{-1}
	$\dot{\phi}(t)$ shaft ang. vel. (rad/s)	2- ref. shaft ang. vel.	0.19 rad/s^{-1}
		3- shaft ang. pos. error	0.5 rad^{-1}
		4- shaft ang. vel. error	0.07 rad/s^{-1}
		5- efference copy	1 A^{-1}
Balancing Robot	$\phi(t)$ wheel angle (rad)	1- ref. wheel ang. pos.	0.03 rad^{-1}
	$\dot{\phi}(t)$ wheel ang. vel. (rad/s)	2- ref. wheel ang. vel.	0.04 rad/s^{-1}
	$\theta(t)$ body tilt ang. pos. (rad)	3- body tilt ang. pos. error	1 rad^{-1}
	$\dot{\theta}(t)$ body tilt ang. vel. (rad/s)	4- body tilt ang. vel. error	0.5 rad/s^{-1}
		5- wheel ang. pos. error	0.1 rad^{-1}
		6- wheel ang. vel. error	0.2 rad/s^{-1}
		7- efference copy	0.5 A^{-1}
Quadcopter	$x(t)$ hor. pos. (m)	1- ref. hor. pos.	0.05 m^{-1}
	$\theta(t)$ pitch (rad)	2- ref. pitch pos.	0.5 rad^{-1}
	$\dot{x}(t)$ hor. vel. (m/s)	3- hor. pos. error	0.05 m^{-1}
	$\dot{\theta}(t)$ pitch vel. (rad/s)	4- pitch error	0.6 rad^{-1}
		5- hor. vel. error	0.05 m/s^{-1}
		6- pitch vel. error	0.1 rad/s^{-1}
		7- efference copy	0.3 A^{-1}

Reference (ref.), angular (ang.). velocity (vel.), horizontal (hor.), and position (pos.).

Input for all control plants is in units of electric current (A).

MFs were repeated evenly to account for the 562 inputs in the cerebellar model.

synaptic weights between MFs-GCs and GOs-GCs. $\mathbf{x}_{\text{GO}} \in \mathbb{R}_+$, and $\mathbf{x}_{\text{BA}} \in \mathbb{R}_+$, $\mathbf{W}_{\text{MF-GO}} \in \mathbb{R}_+$, $\mathbf{W}_{\text{PF-GO}} \in \mathbb{R}_+$, $\mathbf{W}_{\text{PF-BA}} \in \mathbb{R}_+$, $\mathbf{W}_{\text{PF-PC}} \in \mathbb{R}_+$, $\mathbf{W}_{\text{BA-PC}} \in \mathbb{R}_-$ follow the same notation for GOs, BAs, and PCs, respectively. Where $\mathbb{R}_+ = \{x \in \mathbb{R} : 0 < x \leq 1\}$ and $\mathbb{R}_- = \{x \in \mathbb{R} : -1 < x \leq 0\}$ for excitatory and inhibitory synapses, respectively. Firing rate vectors are all \mathbb{R}_+ , but \mathbf{y}_{PC} is $\mathbb{R} = \{x : -0.5 < x \leq 0.5\}$ so that it can be subtracted from the motor command produced by a classical controller in the non-cerebellar pathway (**Fig. 3.1A**, PD) and sent to the plant. These vectors are embedded in the address event representation of the network proposed to efficiently implement the cerebellar model in LabVIEW (**Appendix A**).

In order to standardize the contribution of each MF input to the cerebellar model, pre-cerebellar gains were set as normalizing scaling constants for each MF. These values were taken from the maximum values in the description of the control plant's hardware. **Table 3.2** shows the scaling gains for each control plant. Then, the scaled MFs were passed through an activation function ($\mathbf{y}_{\text{MF}} = 1/(1 + e^{-\sigma(\mathbf{x}_{\text{MF}} - \mu)})$) to obtain firing rates compatible with the model (i.e., \mathbb{R}_+), where σ and μ are as defined previously.

The cerebellar model can be configured to include one (uni-hemispheric) or two (bi-hemispheric) networks. The construction of each network follows a 3D dimensional ap-

proach¹²³ presented in **Appendix A**. Random synaptic weights (**W**) are extracted from a normal distribution ($\mu = 0.9$ and $\sigma = 0.1 \in [0.8, 1]$) and multiplied by a normalizing constant (d) that is cell dependent. d is determined as the inverse of the number of inputs of the same nature (excitatory or inhibitory) of each cell¹²³. A proportional and derivative (PD) controller, which is a feedback controller widely used in industry and other applications, is included in tandem with the cerebellar model to provide the non-cerebellar and no-adaptive input to the vestibular nucleus (VN) that receives the firing rate of PCs from left and right hemispheres and then produces the motor command (**Fig. 3.1C, PD**).

Inputs to the cerebellar model are carried by MFs and a climbing fiber (CF). MFs are postulated to provide desired motion signals, efference copy of motor commands, and sensory error signals (i.e., desired trajectory - actual trajectory)^{8;60;66}. The CF input on the other hand, has been proposed to carry an error signal that drives plasticity at the cerebellar cortex⁷⁰, specially at synapses between PFs and PCs. The current configuration of the cerebellar model includes long term depression (LTD) and long term potentiation (LTP) at PF-PC synapses⁶⁹ as described below:

$$\Delta W_{\text{PF}_i-\text{PC}_j}(t) = \begin{cases} -\gamma_{\text{LTD}} c f(t) y_{\text{pf}_i}(t) & \text{if } c f(t) > c f_{\text{spont}} \\ \gamma_{\text{LTP}} y_{\text{pf}_i}(t) & \text{if } c f(t) < c f_{\text{spont}} \end{cases} \quad (3.9)$$

where $\Delta W_{\text{PF}_i-\text{PC}_j}(t)$ is the change in the synaptic weight between the i -th PF and the target j -th PC, $c f(t) \in \mathbb{R}_+$ is the climbing fiber activity, $y_{\text{pf}_i}(t)$ is the firing rate of the i -th PF (in the range $[0, 1]$), and $\gamma_{\text{LTD}} = 4 \times 10^{-6}$ and $\gamma_{\text{LTP}} = 0.3 \times 10^{-6}$ are the learning rates for LTD and LTP, respectively. The threshold value $c f_{\text{spont}} = 0.05$ represents the spontaneous activity in CF that has been shown to encode non preferred direction of sensory error^{58;59;123}. In the case of the bi-hemispheric network, each hemisphere is configured to receive a CF (**Fig. 3.1A,C**, $c f_{\text{right}}$ and $c f_{\text{left}}$) carrying information from mainly one direction of the motion of the control plant¹²³ (See **Chapter 5** for further details about the CF and its low-DC firing rate).

3.3 Robot control experiments with the cerebellar model

3.3.1 Characteristics of the control objects

Three control objects, a brushed DC motor, a two-wheel balancing robot, and a quadcopter are employed (**Fig. 3.2**). The 2 W brushed DC electric motor (RC-280SA, Mabuchi CO, LTD, Japan. **Fig. 3.2A**) generates a torque directly from DC current supplied. It is a control object with a single DoF. The motor's shaft is interfaced with an encoder circuit (ZMP INC.,

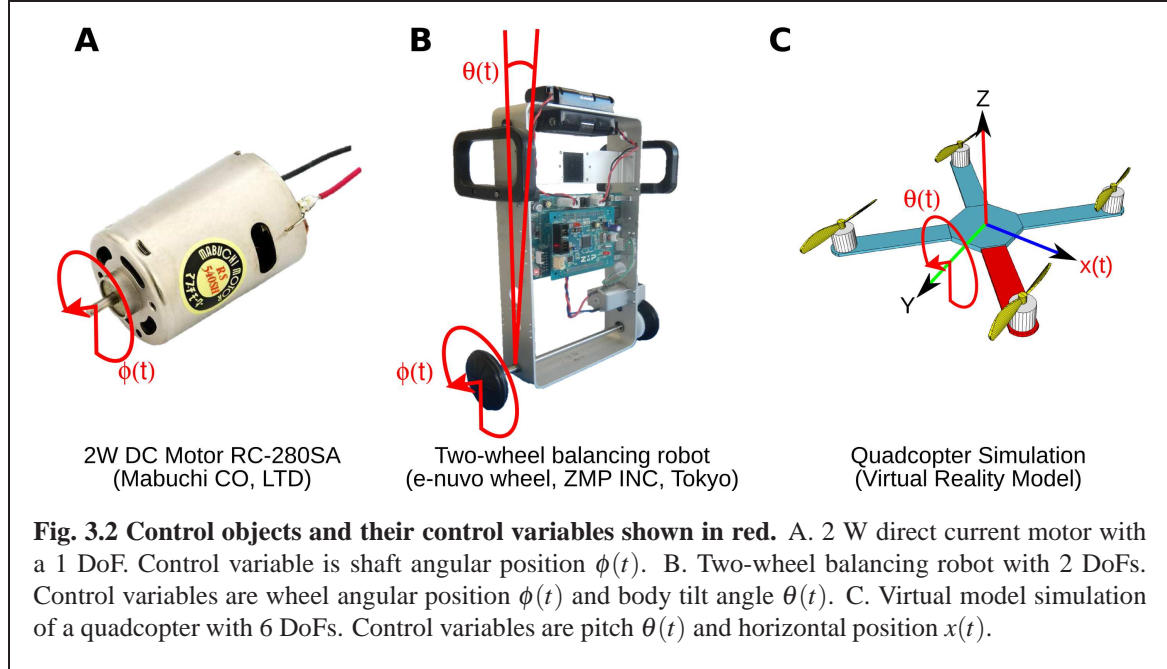


Fig. 3.2 Control objects and their control variables shown in red. A. 2 W direct current motor with a 1 DoF. Control variable is shaft angular position $\phi(t)$. B. Two-wheel balancing robot with 2 DoFs. Control variables are wheel angular position $\phi(t)$ and body tilt angle $\theta(t)$. C. Virtual model simulation of a quadcopter with 6 DoFs. Control variables are pitch $\theta(t)$ and horizontal position $x(t)$.

Japan) for providing angular position information ($\phi(t)$), and a microcontroller board (e-nuvo CPU board, ZMP INC., Japan) in charge of communication with the implementation computer via USART Serial protocol. The MF inputs to the cerebellar model for this control object are shown in **Table 3.2**. The PD controller for this plant is a position controller with $k_p = 0.8$ and $k_d = 0.01$ as proportional and derivative constants, respectively. A virtual model simulation for this motor has been included in the repository of the cerebellar model^b.

The two-wheel balancing robot (e-nuvo wheel, ZMP INC, Tokyo. **Fig. 3.2B**) is a 2 DoFs inverted pendulum system that is highly unstable and widely used in control engineering for testing control strategies⁹². It is equipped with a set of sensors including a motor encoder and a gyroscope, which provide wheel angle ($\phi(t)$) and body tilt angle ($\theta(t)$), respectively. The robot is also equipped with a USART chip to allow serial communication with the computer on which the cerebellar model was implemented. The motion of the robot is driven by a single DC motor connected to its wheels. The MFs inputs carry the signals described in **Table 3.2**. Sampling period for the two-wheel balancing robot alike the DC motor is 10 ms. The PD controller in this control object is a parallel configuration of two controllers (body position controller: $k_p = 5$ and $k_d = 0.5$ and wheel position controller: $k_p = 0.2$ and $k_d = 0.05$) designed by following optimal settings for automatic controllers^{92;172}, so that the addition of both outputs (i.e., PD controller output) alone can stably operate the robot during a simple task ($\phi_{ref}(t) = \pi \sin(2\pi 0.1t)$, where $\phi_{ref}(t)$ is the desired wheel angular

^b<https://bitbucket.org/rdpinzonm/the-bicnn-model>

position).

The quadcopter is a 6 DoFs system multirotor helicopter that is lifted and propelled by four brushless DC motors. The mathematical model describing its dynamics has been reported somewhere else^c. The MF inputs for this simulated quadcopter carry the signals described in **Table 3.2**. The four motors of the quadcopter are controlled by the action of four PD controllers corresponding to yaw, pitch, roll, and altitude, respectively. Controlling the displacement of the quadcopter in the X, Y, and Z plane is achieved by changing the reference point of pitch, roll and altitude controller, respectively. Here, we interface the cerebellar model in the control loop for pitch ($\theta(t)$). Parameters of the controllers can be found in the virtual dynamical model simulation included in the cerebellar model repository^d.

3.3.2 Experimental protocol

For the experiments presented in this chapter, the cerebellar model was configured with a bi-hemispheric structure (**Fig. 3.1D**) with the number of cells consigned in **Table 3.1**. A control task was configured for each control object comprising at least 100 repetitions of the desired motion. In the case of the DC motor, the desired shaft position ($\phi_{ref}(t)$) is a sinusoidal motion at $f = 0.5$ Hz (i.e., $\phi_{ref}(t) = \pi \sin(2\pi 0.5t)$). The balancing robot is commanded to follow a sinusoidal wheel motion ($\phi_{ref}(t) = \pi \sin(2\pi 0.25t)$) while the body tilt angle remained constant (90 degree with respect to the horizontal plane, $\theta_{ref}(t) = 0$), whereas the desired motion for the quadcopter is a sinusoidal horizontal (X-plane) motion with amplitude 2 m (i.e., $x_{ref}(t) = 2 \sin(2\pi 0.2t)$) hovering at 3 m (i.e., $x_{ref}(t) = 3$). Amplitude and frequency of the desired motions were chosen to be between 80 and 90 % of the maximum values that can be controlled for each plant in our setup. Since the attained motor performance might be affected by the initialization conditions of the cerebellar model such as the random values of the synaptic weights and the random synaptic connections, five different sets of random synaptic weights and five tables of random synaptic connections are created to conform a set of 25 permutations of initial conditions for the cerebellar model. Each control task was repeated at least 25 times. The yielded motor performance was measured cycle-by-cycle as the root mean square error (RSE) of the desired and yielded motion.

^c<https://github.com/dch33/Quad-Sim>

^d<https://bitbucket.org/rdpinzonm/the-bicnn-model>

3.4 Results

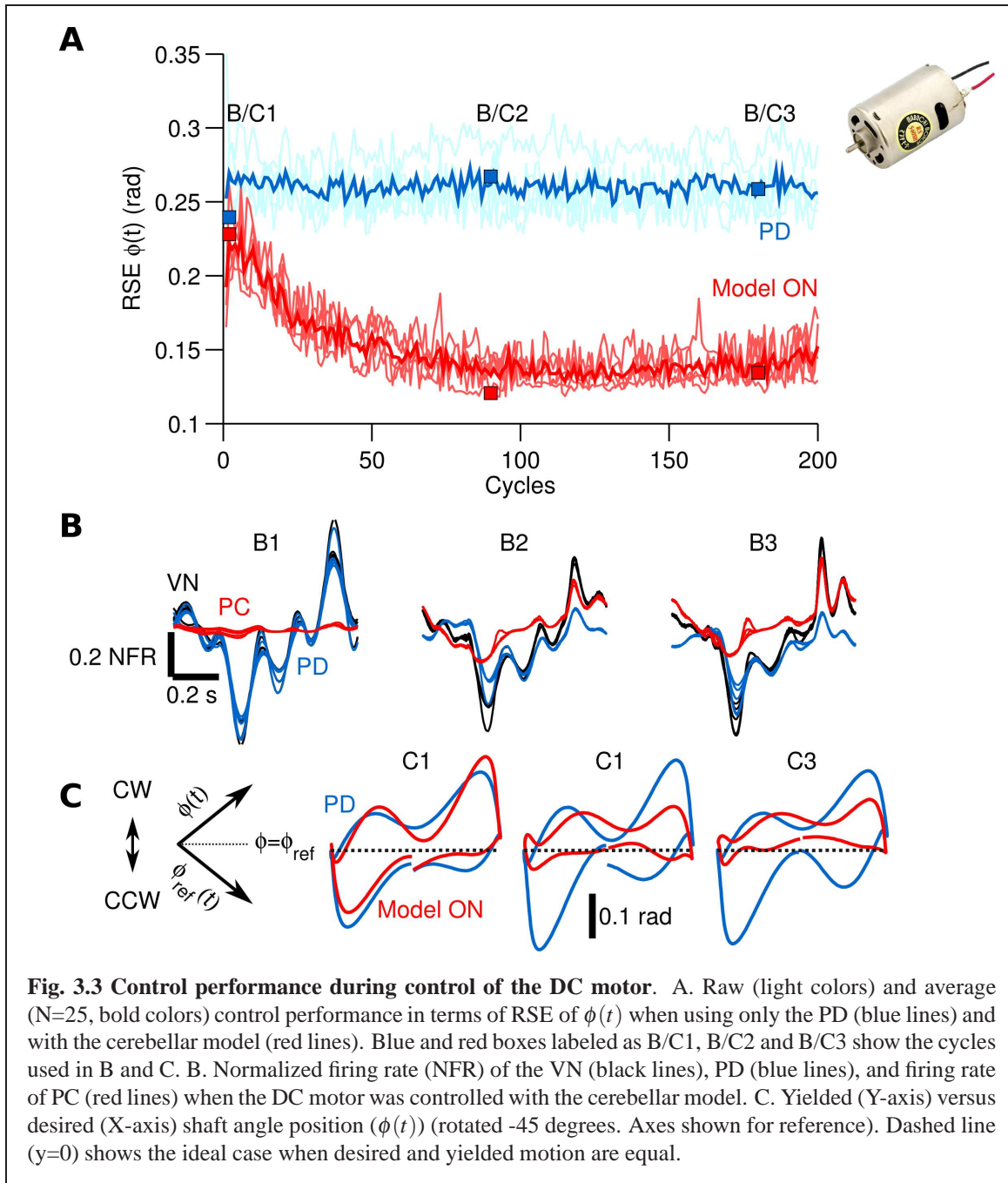
3.4.1 Control of a 1 DoF plant: a DC motor

Fig. 3.3 shows the control performance attained during control of the DC motor in terms of the RSE of the shaft angular position ($\phi(t)$) when the cerebellar model was enabled (red lines) and disabled (blue lines). When the cerebellar model is disabled the PD is the only controller acting on the control plant. Raw (light blue and red lines) and average ($N=25$, bold red and blue lines) RSE of $\phi(t)$ are shown (**Fig. 3.3A**). The RSE of $\phi(t)$ shows that the cerebellar model adapted and improved the motor performance (RSE value was reduced on average 0.1 rad, 40.2% of the initial error value 0.26 rad), meaning that the PC learned to produce the adequate motor commands to move the shaft of the DC motor to follow the desired motion. As expected, the performance when the cerebellar model was disabled showed no adaptation and lower performance. The output firing rate of the PC (red lines), the PD output (blue lines), and VN firing rate (black lines) are shown in **Fig. 3.3B**. Panels B1, B2, and B3 show five cycles super imposed of each output in the cycles marked in **Fig. 3.3A**. These panels show the adaptation of the cerebellar model output to the current control task. During the beginning of the experiment (panel B1), the PC output was small and presented little modulation of its firing rate. Then, by the middle of the experiment (panel B2) the PC shows adaptation and its firing rate follows the VN output. This behavior remains to the end of the experiment (panel B3).

These firing rates produced the shaft trajectories shown in **Fig. 3.3C**. The yielded trajectories are presented in a XY plane rotated -45 degrees where the x-axis corresponds to the desired shaft position ($\phi_{ref}(t)$) and the y-axis corresponds to the yielded motion ($\phi(t)$). In the ideal case the desired and yielded motions are equal, the corresponding trajectory is shown in the XY plane as a horizontal line at $y = 0$ (**Fig. 3.3C**, dashed lines). Erroneous motions in the clockwise (CW) and counterclockwise (CCW) rotations of the motor shaft are mapped in the planes $y > 0$ and $y < 0$, respectively. Panels C1 to C3, also marked in **Fig. 3.3A**, show the progressive reduction of the deviation from the ideal trajectory ($\phi = \phi_{ref}$) due to the adaptation in the cerebellar model. Panel C3 also evidences a small asymmetry in the output of the cerebellar model that produced an offset of the yielded motion towards the clockwise (CW) rotation of the motor.

3.4.2 Control of a 2 DoFs plant: a two-wheel balancing robot

Next, we show the results obtained with a more challenging control task, namely, the two-wheel balancing robot. **Fig. 3.4** in the same format as **Fig. 3.3**, shows the control perfor-

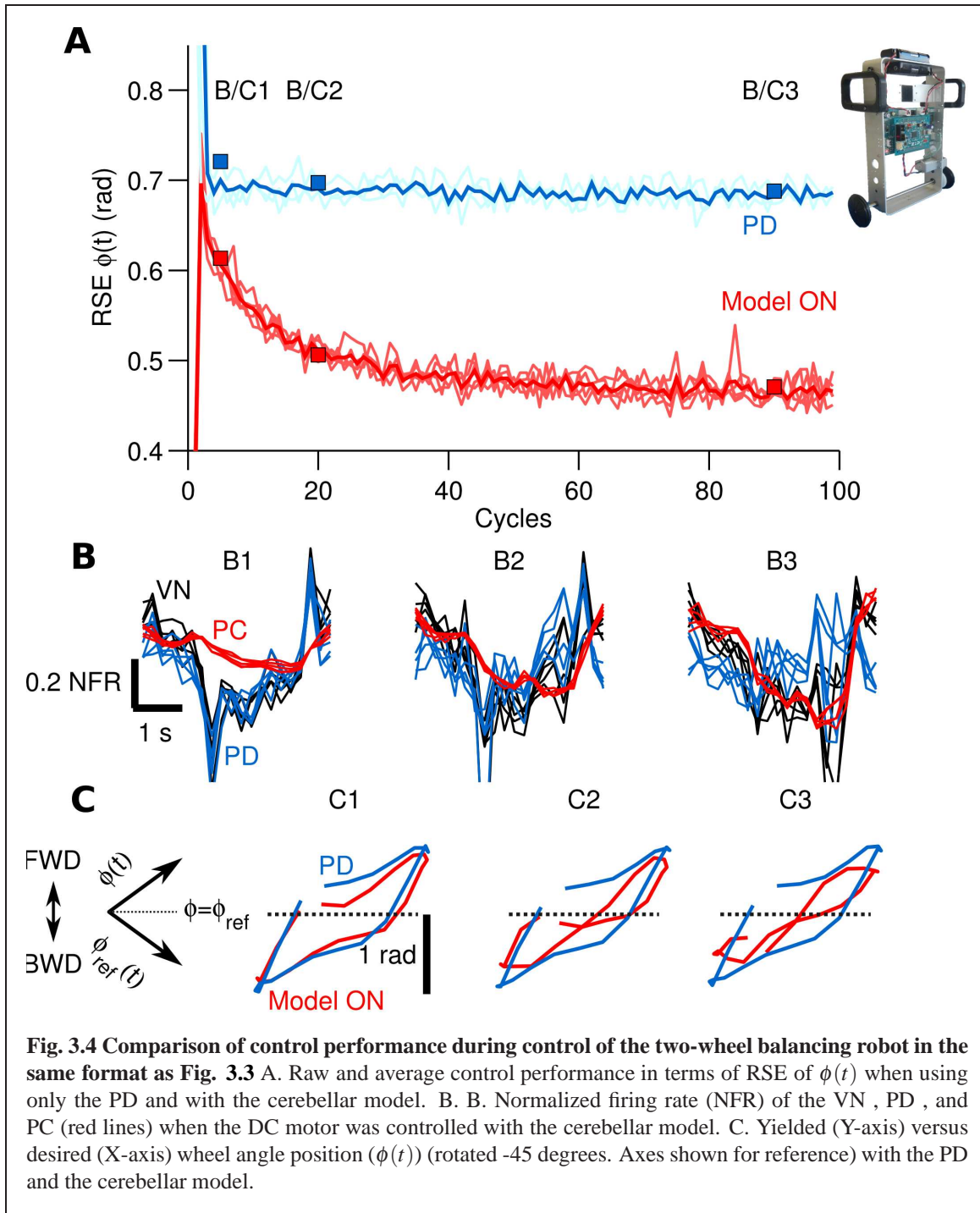


mance attained with the cerebellar model and the PD alone during control of the two-wheel balancing robot and sinusoidal desired motion ($\phi_{ref}(t)$) at 0.25 Hz. The average improvement in control performance by using the cerebellar model was 0.2 rad or 28.5% of the initial value (0.7 rad). Similar to the previous control scenario, the firing rate of the cerebellar model output (i.e., PC output) adapted to the control task (Fig. 3.4B, panels B1 to B3).

Panel B1 shows that at the beginning of the experiment the output of the cerebellar model was small compared with the PD and VN, however, the cerebellar output evolved and increased its amplitude to account for a large part of the VN input (panel B3). **Fig. 3.4C** in the same format as **Fig. 3.3C**, shows the improvements of the trajectories achieved with the robot when the cerebellar model was enabled (red lines). The hysteresis observed in panels C1 to C3 (i.e., the separation from the ideal motion in the forward (FWD) and backward (BWD) motions) show that the yielded motion is delayed with respect to the desired motion. This means that when the desired motion changes from BWD to FWD motions the robot responded late, producing a deviation of approximately 1 rad and 0.7 rad when using the PD and the cerebellar model, respectively. This hysteresis was corrected in an average of 30% by using the cerebellar model (panel C1 in comparison with C3).

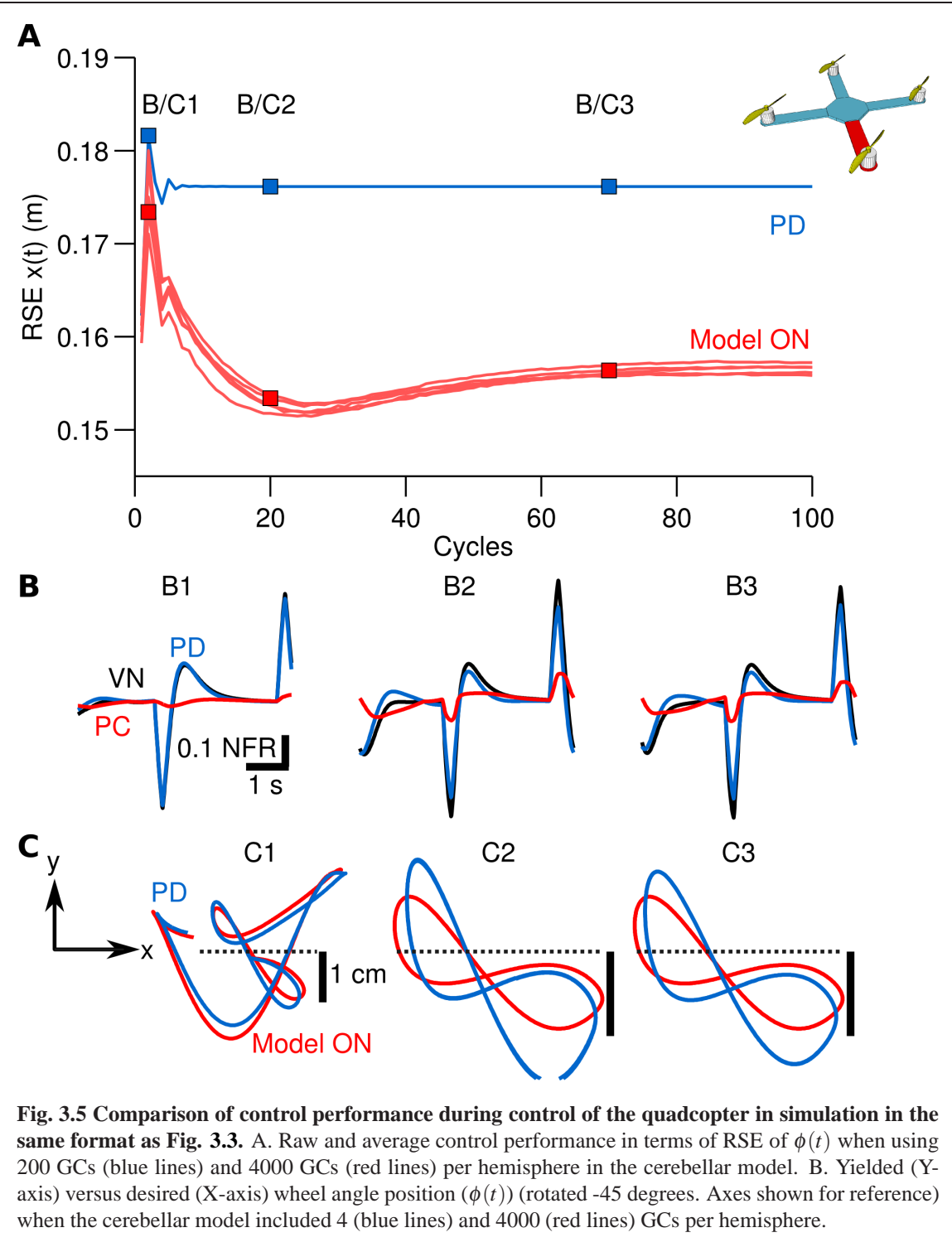
3.4.3 Control of a 6 DoFs plant: a simulated quadcopter

Lastly, we show that the cerebellar model can be interfaced with a 6 DoFs plant to improve its performance in a simulation study. The quadcopter (**Fig. 3.2C**) is commanded to hover at $z_{ref}(t) = 3$ m and follows a sinusoidal desired horizontal translation in the x-axis (See Sec. 3.3.2 for mode details about the experimental protocol). **Fig. 3.5** in the same format as **Fig. 3.4** summarizes the control performance attained with this control object. **Fig. 3.5A** depicting the RSE of $x(t)$ when the cerebellar model was enabled (red lines) and disabled (blue lines) evidences the improvement in performance achieved by incorporating the cerebellar model into the control loop of the quadcopter. The average improvement was 2 cm or 11 % of the initial value. Firing rates of the PC, PD and VN during control of the quadcopter with the cerebellar model enabled (**Fig. 3.5B**), show the adaptation of the PC output during this control task. In particular, panel B1 in comparison with panel B3 evidences the adaptation at the firing rate of the PC to accomplish higher control performance (**Fig. 3.5A**). Panels B1 to B3 also suggest that the firing rates, which are in the interval [0 1], could be further increased with an output gain so that the VN, PD and PC are in similar ranges. This would increase the contribution of the PC to the VN, and presumably improve control performance as shown in the previous two control scenarios with real world control plants. The trajectories generated with the cerebellar model and the PD alone are shown in **Fig. 3.5C**. This XY plane is not rotated as in **Fig. 3.3C** and **Fig. 3.4C**. Panels C1 to C3 show the improvement in the trajectory of the quadcopter with the cerebellar model. With the cerebellar model the generated trajectory gets closer to the ideal trajectory that lies in the x-axis (**Fig. 3.5C**, dashed lines).



3.5 Discussion

This chapter has introduced a realistic neuronal network model of the cerebellum and its application into control engineering. The model includes a realistic learning rule and a neu-



ronal architecture in-line with reported anatomical and physiological studies. We demonstrated how to incorporate the cerebellar model into classical control loops. Experimental

results obtained during three control tasks were stable and consistent while considering a basic control plant (DC motor) with a single DoF, one of the most challenging plants in control engineering (the two-wheel balancing robot)⁹² with 2 DoFs, and a simulation dynamic model of a quadcopter with 6 DoFs. These varieties of control objects demonstrate the generalization of the cerebellar model and provide a reference framework for future applications.

4

Error signals in the climbing fiber required for cerebellar motor learning

OTOR learning in the cerebellum is believed to entail plastic changes at synapses between parallel fibers and Purkinje cells, induced by the error information in the climbing fiber input. Despite the abundant research on the cerebellum, the type of error information is still a matter of debate. Two types of error information have been proposed to be plausible in theoretical and simulation studies: sensory error (SE) and motor command error (ME), however, their plausibility have not been tested in real world. Here we conducted a comparison of different types of climbing fiber error information in real world engineering applications by using the neuronal network model of the cerebellum presented in **Chapter 3**. We employ the direct current motor (simple task), and the two-wheel balancing robot (difficult task). We demonstrate that SE, ME, or a linear combination of the two is sufficient to yield comparable performance in the simple task. When the task is more difficult, although SE slightly outperformed ME these types of error information are all able to adequately control the robot. Thus, unlike previous theoretical and simulation studies that support only SE or ME, it is demonstrated for the first time in a real world engineering application that both SE and ME are adequate as the climbing fiber error signal, even when the control task is as difficult as stabilizing a

two-wheel balancing robot.

4.1 Introduction

The climbing fiber (CF) input to the cerebellum is considered to carry the error information required for improvements of motor skills as a basis for motor learning^{57;68;69;77;101;145;152}. There have been controversies about the nature of this error signal^{31;70;86;152}. In general, movement errors defined as the discrepancy between the movement to be performed and the movement actually produced are detected by sensory systems whose outputs are used to update motor commands so that the ongoing errors will be reduced in the future movement. Thus there are two types of potential error signals that can be used to drive the cerebellar synaptic plasticity. Namely, one from the sensory output encoding error in movement kinematics (sensory error: SE), the other from the output of premotor systems encoding error in motor command (motor error: ME)⁷⁰. For example, in the case of a tracking eye movement called smooth pursuit that is initiated when we try to follow a smoothly moving visual target with the eyes, the movement error is the deviation of the eye velocity from the target velocity. This movement error causes a slippage of the target image on the retina that is detected by the retinal neuronal network. Thus the output of the retina (ganglion cell activities) encoding the image slip kinematics is SE. Once the image slip is detected, the smooth pursuit system works to reduce it by modifying motor commands sent to the extra-ocular muscles. This modified motor command is ME. There are physiological evidence and computational studies supporting each error signal. In support of the notion that CF carries SE, CF activities highly correlated with retinal slip during optokinetic visual stimuli have been reported in rabbits⁵² and monkeys¹⁴⁷. In contrast, supports for CF carrying ME have been provided by single unit recording experiments using rabbits⁴¹ and monkeys⁸⁶. A major cause of these contradictory results about the information contents in the CF activities is that SE and ME signals are in most cases alike in simple movement controls employed in these behavioral and neurophysiological experiments, and thus hard to dissociate each other. Appropriate experimental conditions enabling dissociation of SE and ME are required to evaluate the CF information content.

Computational models of the cerebellum that include CF dependent motor learning scheme have been widely used in engineering applications^{18;46;63;124;151;168}. These models may provide a potential framework in which the CF content could be evaluated by testing them in appropriate movement control tasks. However, there has not been any evaluation of the CF content by using these cerebellar computational models. Here we conduct a real-world testing of our cerebellar neuronal network model in robot control that enable dis-

sociation of SE and ME, and compare the performance of the robot when the different error signals are used. We employ the uni-hemispheric configuration of the model presented in **Chapter 3**. For this cerebellar model, we configure adequate control tasks in which SE and ME are clearly dissociated. We demonstrate that SE and ME yield equivalent performance when the control task is simple, while SE yielded slightly higher performance when the control task is more complex. Possible mechanisms underlying these results in cerebellar neural network are discussed.

4.2 Configuration of the model to test the CF error content

4.2.1 Nature of the two types of error information in CF

Sources of SE and ME are generated from the non-cerebellar pathway. That is, SE signal is computed from the difference between the desired and actual movement^{61;69}. It carries position and velocity error components in kinematic coordinates (expressed in angle unit: rad), whereas ME is computed as the output of the PD feedback controller in the non-cerebellar pathway (**Fig. 3.1A**), which represents error in motor command dynamic coordinates (expressed in electric current unit: A) as used in previous modeling studies^{78;80}. Additionally, the linear combination of the two types of the signals (SE + ME) is also tested, as it has been suggested to be a plausible case in the real cerebellum⁸⁵. The equations of SE and ME for each of the control plant are as follows:

$$\text{SE}_{\text{DC motor}} = a_1\phi(t)_e + a_2\dot{\phi}_e(t) \quad (4.1)$$

$$\text{SE}_{\text{robot}} = a_1\phi(t)_e + a_2\dot{\phi}_e(t) + b_1\theta_e(t) + b_2\dot{\theta}_e(t) \quad (4.2)$$

$$\text{ME} = c_1\text{PD}(t) \quad (4.3)$$

where subscript “e” denotes error and corresponds to the difference between the desired and yielded motion (e.g., $\phi_e(t) = \phi_{ref}(t) - \phi(t)$), constants $a_1 = 0.5 \text{ rad}^{-1}$, $a_2 = 0.02 \text{ rad/s}^{-1}$, $b_1 = 5 \text{ rad}^{-1}$, $b_2 = 0.5 \text{ rad/s}^{-1}$, and $c_1 = -0.4 \text{ A}^{-1}$ are scaling values intended to equalize the contribution of each error component to the SE and ME signals so that all have the same importance. These values were calculated with the cerebellar model disabled (i.e., plant controlled only by the feedback controller and desired motion $\phi_{ref}(t) = \pi \sin(2\pi 0.1t)$). ME in **Eq. 4.3** remained the same for both control plants. Combination of SE and ME is computed directly from **Eq. 4.1-4.2** and **Eq. 4.3**.

4.2.2 Experimental protocol

For the experiments presented in this chapter, the cerebellar model was configured with the uni-hemispheric structure (**Fig. 3.1C**) including 755 GCs, 5 GOs, 15 BAs, and 1 PCs. The desired motion $\phi_{ref}(t)$ for the control plants employed to assess the performance of the cerebellar model is a sinusoidal motion. The sinusoidal wave was generated at frequencies ranging from 0.2 Hz to 0.4 Hz and amplitude of π (maximum angular velocity: 7.89 rad/s). The frequencies of the stimulus were chosen below the maximum controllable velocity of the robot (9.82 rad/s). The desired body tilt angle $\theta_{ref}(t)$ was set to zero degree (90 degrees with the ground), so that the robot is commanded to remain vertical while following the desired wheel trajectory. Each stimulus was repeated up to 100 cycles. Considering that the random initialization of synaptic weights in the cerebellar neuronal network can be a source of variability in the performance of the model, five different initial sets of random synaptic weights were created for each set of weighted connections (\mathbf{W}_{PF-PC} , \mathbf{W}_{MF-GC} , \mathbf{W}_{MF-GO} , \mathbf{W}_{GO-GC} , \mathbf{W}_{PF-GO} , \mathbf{W}_{PF-BA} , and \mathbf{W}_{BA-PC}) extracted from a normal distribution in \mathbb{R}_+ and \mathbb{R}_- with standard deviation 1 and mean value 0.5 and -0.5 for excitatory and inhibitory synapses, respectively. Special care is required to avoid over inhibition of the PC cell when \mathbf{W}_{BA-PC} is large, or instability in the PC cell output when the feedback loop formed by \mathbf{W}_{PF-GO} and \mathbf{W}_{GO-GC} are large. Excluding \mathbf{W}_{PF-PC} that presented LTD and LTP, all the synaptic weights remained fixed during the experiments to evaluate the roles of PF-PC LTD and LTP that are considered a major synaptic plasticity contribution to cerebellar motor learning^{69;133}. Performance of the cerebellar neuronal network controller was measured as the root mean square error (RSE) of each control variable. In the case of the DC motor there was one control variable (the shaft angle $\phi(t)$, **Fig. 3.2C**), whereas there were two control variables for the two-wheel balancing robot (wheel angle $\phi(t)$ and body tilt angle $\theta(t)$, **Fig. 3.2D**).

4.3 Results

4.3.1 Simple control scenario

First, we tested the different CF information contents in the easiest control scenario in our setup, that is, control of the angular position $\phi(t)$ of a metal shaft directly connected to the DC motor (**Fig. 4.1A**) with a sinusoidal desired motion ($\phi_{ref}(t) = \pi \sin(2\pi 0.5t)$). Three types of CF to the cerebellar model were tested separately. Namely, CF carrying SE (**Eq. 4.1**), ME (**Eq. 4.3**), and the combination of the two, i.e., SE + ME.

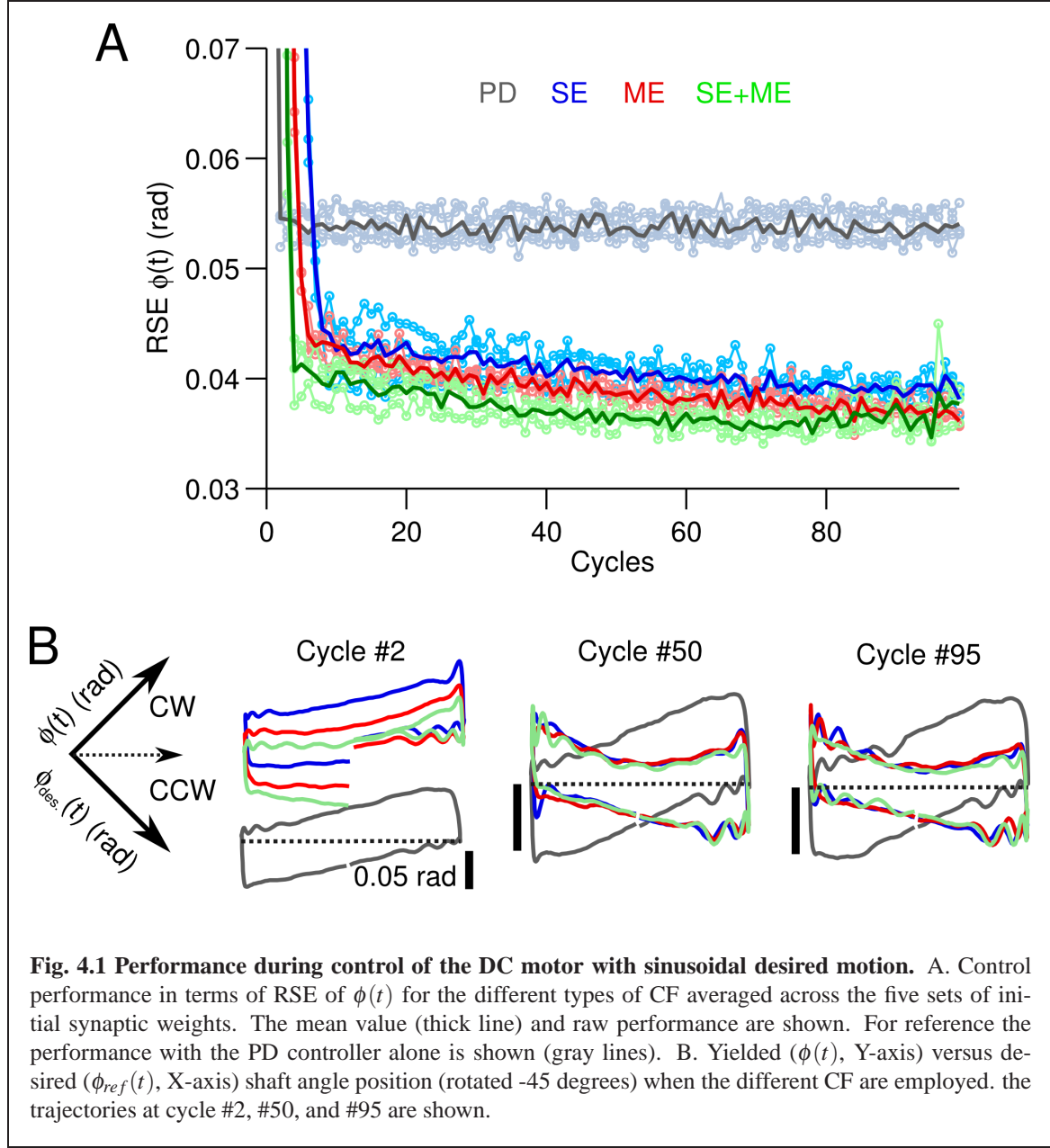
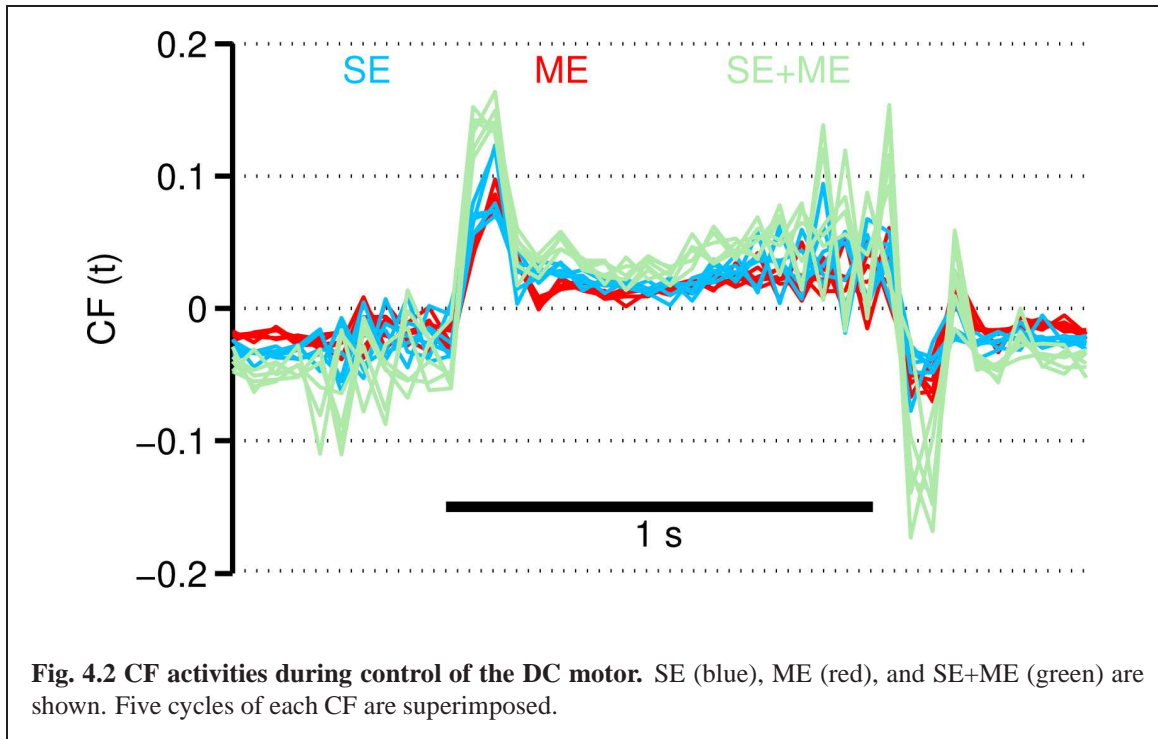
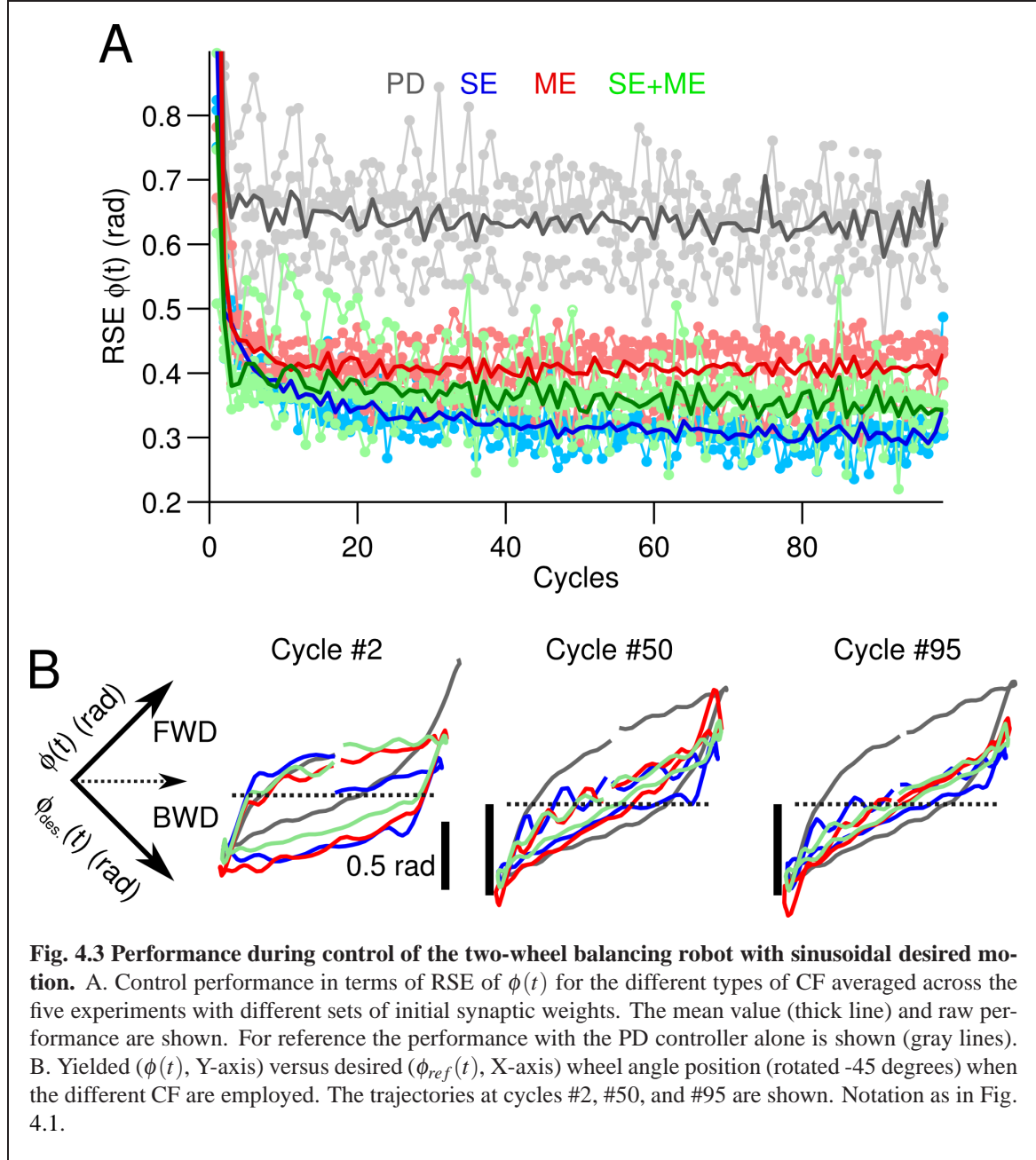


Fig. 4.1 shows the behavioral consequences in control performance under each CF condition (SE, blue lines; ME, red lines; SE + ME, green lines) in terms of RSE of $\phi(t)$ and yielded shaft motions. The performance obtained when the cerebellar model was disabled, i.e., the DC motor is controlled only by the PD, is included as “PD” in gray lines. The RSE of $\phi(t)$ (**Fig. 4.1A**) shows that the performance with the cerebellar model disregarding the CF content outperformed the PD. This improvement was in average 0.015 rad or 30% of the initial value 0.05 rad. Thus, using a CF with SE, ME or the combination of both



produces similar performance in this simple control scenario. Not surprisingly the temporal profiles of these CFs also look alike (**Fig. 4.2**). Differences between the motion caused in the DC motor by the cerebellar model and the PD can be seen in the XY planes shown in **Fig. 4.1B**. These XY planes are constructed as introduced in **Chapter 3** by positioning the desired (X-axis) and yielded (Y-axis) motions in a XY plane rotated -45 degrees. To show the adaptation in the cerebellar model, the motions produced at cycles #2, #50, and #95 are shown. Cycle #2 shows that the cerebellar model caused the DC motor to rotate in excess in the CW direction ($y > 0$). This temporary deviation that lasted for the first 5 cycles was produced by the initialization conditions and number of GCs in the cerebellar model. XY planes corresponding to cycles #50 and #95 show that the PD caused the DC motor to rotate in excess when transitioning from CW to CCW and from CCW to CW. In contrast, the cerebellar model caused the opposite effect in the shaft motion by reducing the rotation speed just before the CW/CCW, CCW,CW transitions. As exemplified here, CF inputs carrying SE, ME, or their combination are adequate error signals to drive plasticity at the cerebellar model and make little difference in control performance if the control scenario is very simple (a shaft with single DoF driven by a DC motor to follow a 0.5 Hz sinusoid).



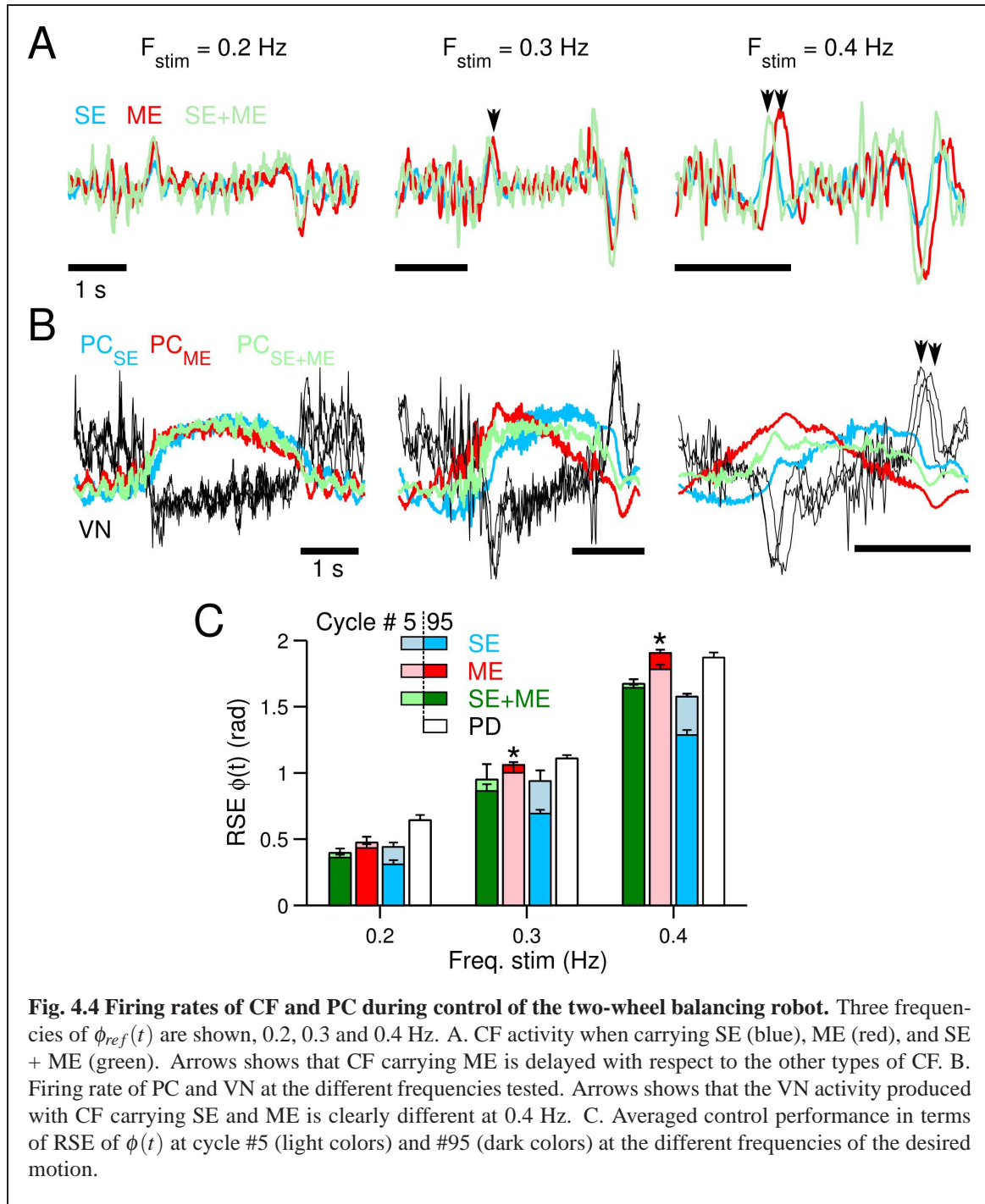
4.3.2 Complex control scenario

After testing the easiest control scenario in our setup, the CF signals on each control scenario seemed to have similar temporal profiles, and thus, the relationship between the error signal used and the control performance attained is yet to be clarified. In this section we tested our setup in a more difficult control scenario to elucidate this relationship. The control scenario employs the two-wheel balancing robot with sinusoidal desired motions for the

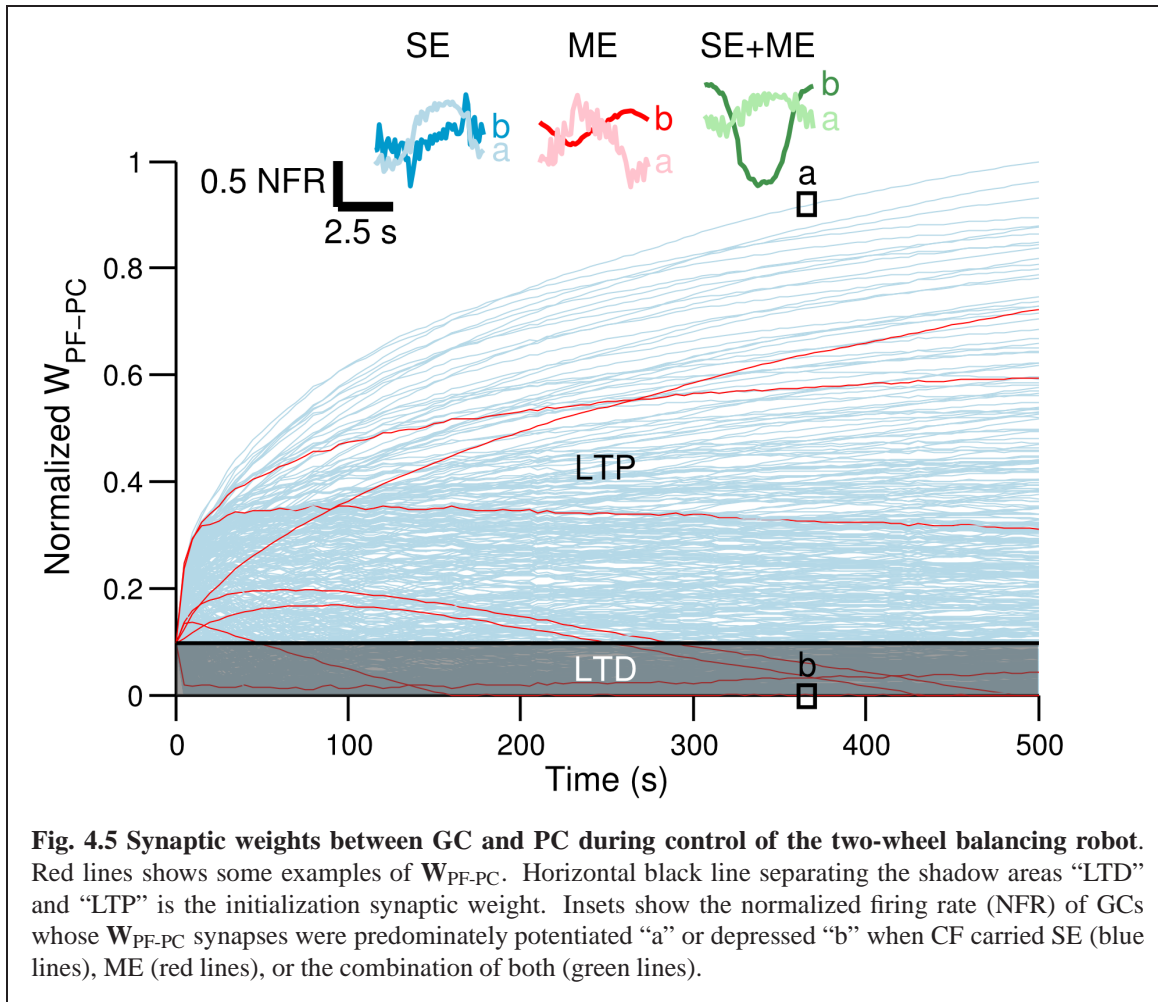
wheel angle. The frequencies of the sinusoidal motion $\phi_{ref}(t)$ ranges from 0.2 Hz to 0.4 Hz (experimental protocol described in Materials and Methods). **Fig. 4.3** in the same format as **Fig. 4.1**, summarizes the control performance achieved at 0.2 Hz. Similarly to the previous case, controlling the two-wheel balancing robot with the cerebellar outperforms the PD alone. The wheel positions generated at cycles #2, #50, and #95 are shown in **Fig. 4.3B**. These trajectories evidence that the cerebellar progressively improve the yielded wheel motion so that the yielded wheel motion approaches the desired wheel motion ($\phi_{ref}(t)$). On the contrary, the wheel motion generated by the PD controlled shows considerably larger hysteresis (**Fig. 4.3B** gray lines). Subtle differences can be seen in the control performance obtained by using SE, ME, or their combination. Nonetheless, increasing the frequency of the desired motion from 0.2 to 0.3 and 0.4 Hz strengthen these differences. **Fig. 4.4** shows the temporal profile of the different CFs, firing rate of PCs, and average control performance at the three frequencies of $\phi_{ref}(t)$. The temporal profiles of CF carrying SE (**Fig. 4.4A**, blue lines), ME (red lines), and SE+ME (green lines) show that at 0.2 Hz all the CFs look alike. However, increasing the frequency of $\phi_{ref}(t)$ reveals that ME lacks with respect to the other types of CFs (**Fig. 4.4A**, black arrows). The firing rates of the PC and the VN (**Fig. 4.4B**) also evidence clear differences in using SE or ME in the CF. At 0.4 Hz the firing rate of the PC caused by ME and SE are out of phase and presents distinctive shapes. The VN output due to these PC contributions also differ due to the CF types (**Fig. 4.4B**, black arrows). **Fig. 4.4C** summarizes the control performance in terms of average RSE of $\phi(t)$ at each one of the frequencies tested at the beginning (cycle #5) and the end (cycle #95) of the experiments. This figure shows that as the frequency increase the performance with ME deteriorates (**Fig. 4.4C**, red bars), to such extend that at 0.3 and 0.4 Hz there is not improvement over the initial error (**Fig. 4.4C**, asterisks). On the contrary, the performance with SE always reduced the initial error and is better than using the PD or the combination SE+ME. Thus, SE is the best error signal in our setup during control of a highly unstable two-wheel balancing robot.

4.3.3 Neural consequences of the CF error content

We analyzed the neural consequences of using SE, ME or SE+ME in the cerebellar model during the control scenario with the two-wheel balancing robot, which showed behavioral differences caused by these CFs. We show the adaptation produced at PF-PC synapses, the firing rate of GCs, and the correlation of MFs, GCs, and the CF used. **Fig. 4.5** shows the 755 PF-PC synaptic weights ($\mathbf{W}_{\text{PF-PC}}$) during one of the experiments with CF carrying SE. $\mathbf{W}_{\text{PF-PC}}$ with the other CF contents showed similar trends. Gray area shows the weights decreased by LTD from the initial value (black line). Those weights increased by LTP are shown above the black line. Some typical $\mathbf{W}_{\text{PF-PC}}$ are presented in red lines. The number



of potentiated and depressed weights varied across the types of CF. With CF carrying SE, ME, and SE+ME, 65%, 71%, and 68% of the $W_{\text{PF-PC}}$ weights were depressed. Across all the experiments the same trend was observed, namely, the number of depressed GCs were larger by using ME than SE. The insets in **Fig. 4.5** show the normalized firing rate (NFR)



of the GCs whose PF-PC synaptic weights were the most potentiated (labeled as “a”) and most depressed (labeled as “b”) for each type of CF. Firing rate of potentiated GCs are negative correlated with the CF, whereas those depressed are positive correlated with the CF. **Fig. 4.6A** shows the coefficient of correlation of the CF and the GCs activity. The moving average ($N=13$) is shown in bold lines. GCs have been sorted in the x-axis from the most depressed ($x=0$) to the most potentiated GC ($x=755$). Shadowed area shows those GCs whose activity was depressed via LTD at the PF-PC synapses. The coefficient of correlation when using SE, ME, or SE+ME show that those GCs potentiated are negatively correlated with the CF, meaning that increasing their activity reduces the error signal, whereas those GCs depressed are positively correlated with the error signal. This figure confirms our assumption about the cerebellar mechanism of motor learning by LTD and LTP at PF-PC synapses.

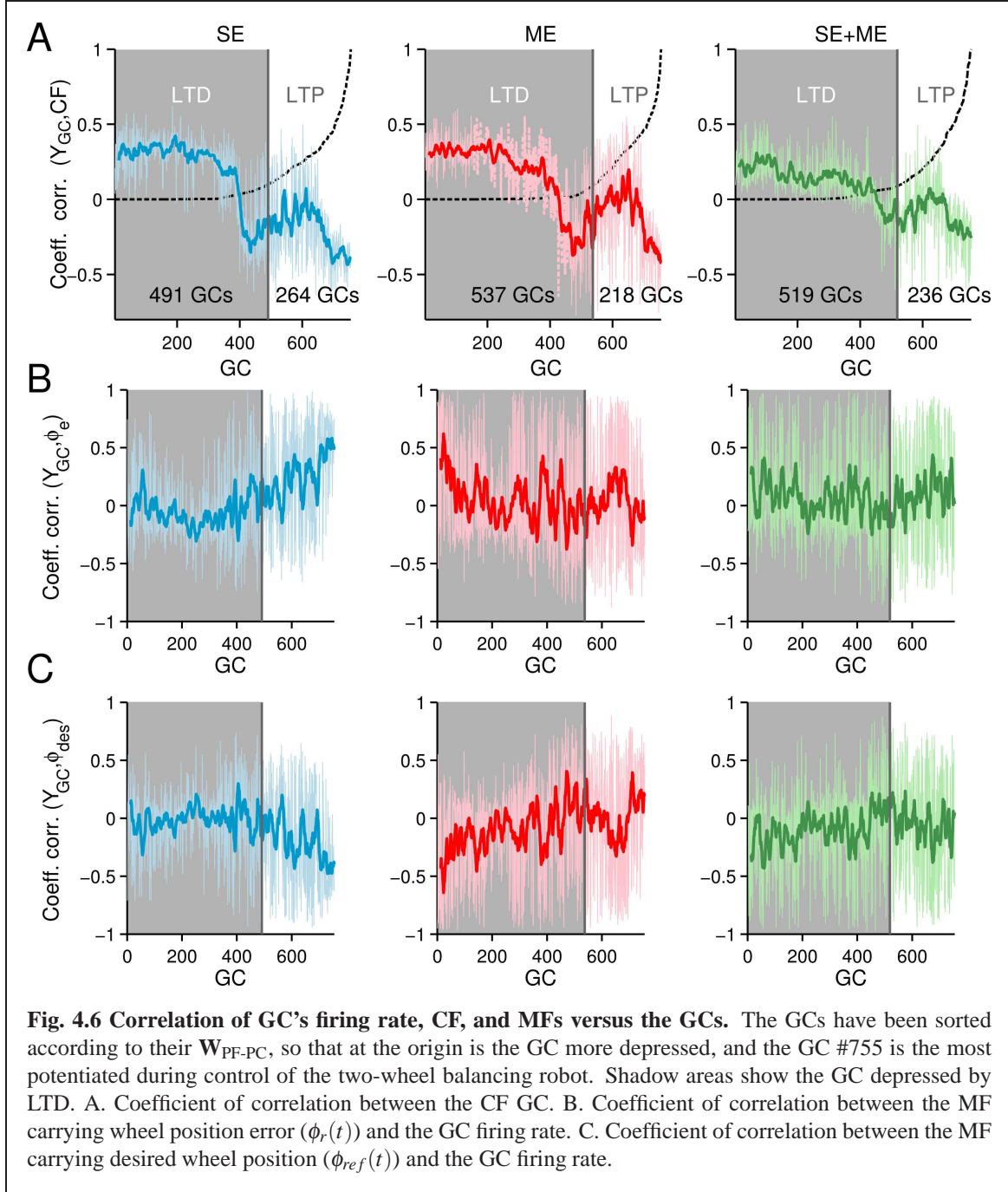
Correlation of the GCs activities with the MF inputs reveals intrinsic differences when

using SE (blue lines) and ME (red lines). **Fig. 4.6B** shows the coefficient of correlation of the MF carrying wheel position error ($\phi_e(t)$) and the activities of GCs. In this correlation, those GCs positively correlated were preferably potentiated when using SE, contrary to when using ME. **Fig. 4.6C** shows the coefficient of correlation of the MF carrying wheel desired position ($\phi_{ref}(t)$) and the activities of GCs. In this correlation, those GCs negatively correlated were preferably potentiated when using SE, contrary to when using ME. These two correlations evidence intrinsic differences when using SE and ME. GCs with firing activity in-phase with error components (i.e., $\phi_e(t)$ and $\dot{\phi}_e(t)$), and out of phase with desired motions (i.e., $\phi_{ref}(t)$ and $\dot{\phi}_{ref}(t)$) were preferably engaged to produce the PC activity when using SE. When using ME the opposite relationship was more prominent among the GCs potentiated. Other MFs, such as the efference copy did not show differences between SE and ME. Employing the combination of SE and ME, seems to soften the correlations observed with SE and ME to an intermediate point (**Fig. 4.6**, green lines), thus, it is not surprising that using SE+ME as CF produced intermediate control performance (**Fig. 4.4**, green lines).

4.4 Discussion

Debate about the error information encoded in the CF input to the cerebellum has been going on for several years^{31;70;86;152}. Two types of error have been greatly defended: SE and ME. Behavioral and neurophysiological support has been presented for SE in rabbits⁵² and monkeys¹⁴⁷, and similarly for ME in rabbits⁴¹ and monkeys⁸⁶. Consensus has been difficult to reach because these behavioral and neurophysiological experiments employ simple movement tasks where the temporal patterns of SE and ME are alike. To the best knowledge of the authors, this study is the first direct comparison of the types of error information encoded in the CF input to a cerebellar neuronal network model and with the motor performance attained during a real-world engineering application. Our setup allowed us to configure the difficulty of the control task, change the type of error encoded by the CF, and evaluated the yielded control performance, thus, allowing us to effectively disassociate SE and ME.

Our experimental results showed that both SE and ME despite producing unique behavioral and neural changes in the cerebellar model, specially at the PC cell output (**Fig. 4.4B**), are adequate error signals to govern successfully the plants in a diversity of control tasks (simple, and complex task)(**Fig. 4.1-4.4**). This is the first direct demonstration that both SE and ME can be an adequate error signal to teach the cerebellar model in real world engineering applications. These results are in agreement with biological evidence from the horizontal VOR and OKR systems, a feedforward and a feedback system sharing the same



controller (i.e., cerebellar microcomplex) and the same control object (i.e., eye plant) with CF carrying SE and ME, respectively⁷⁰. However, further evaluation using the two-wheel balancing robot with sinusoidal desired motion at different frequencies revealed quantitative differences in control performance caused by SE and ME (Fig. 4.4). Namely, SE yielded better control performance than ME (Fig. 4.4C). This might be trivial because we eval-

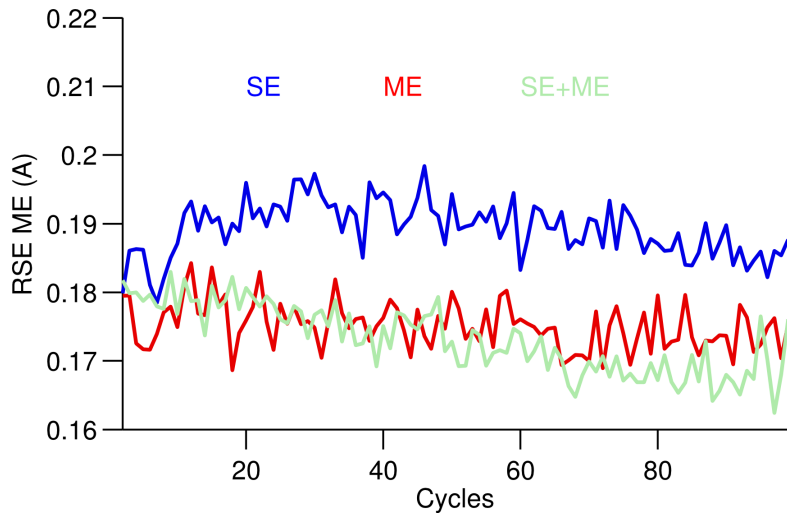


Fig. 4.7 Control performance during control of the two-wheel balancing robot in terms of RSE of ME. It is calculated as the root mean square error between the PD and the PC output. The RSEs of ME when CF carried SE, ME and SE+ME are shown.

ated the control performance in terms of RSE of SE (i.e., RSE of $\phi(t)$) and the cerebellar model was trained to reduce SE. Since the ultimate goal of a control task is to reduce the error between the desired motion and the yielded motion (i.e., reduce SE) in biological systems and engineering applications, we employed RSE of SE as a measure of goodness of control performance. The follow up premise is that measuring the control performance in terms of ME would prompt that encoding ME in CF is better. This is actually the case as shown in **Fig. 4.7**. Yet, RSE of ME is an indirect measure of control performance that can be in opposition to the goal of a control task, that is, to reduce SE. Because different ME could produce the same SE depending on the nature of the control object, choosing RSE of ME could be counterproductive. For example, if the ME is larger than the maximum input range of the control object, the state of the control object would not change with the motor command, and thus, the produced SE is the same as the one produced by a different ME twice larger. Coefficients of correlation of the firing rate activity of GCs, CF, and MFs also revealed intrinsic differences caused by using SE, ME or their combination (**Fig. 4.6**). In particular, GCs activity preferably potentiated by LTP at PF-PC synapses with SE and ME differed in their correlation coefficients with the MF inputs. This means that to produce the PC activities shown in **Fig. 4.6** with SE and ME, GCs with different MF inputs were engaged, and thus the differences in control performance. In particular, GCs carrying error information and GCs carrying desired motions were preferably potentiated with SE and ME, respectively.

We have employed a PD controller as the non-cerebellar pathway that produces ME not only because it is one of the most flexible, effective, and popular feedback controllers^{92;172}, but because it has been previously used in other cerebellar models as the non-cerebellar pathway^{81;135;163} as well. The PD may be actually physiologically plausible since its computation requires sensory information and its first derivative (e.g., eye velocity and eye acceleration), which are available at brain stem⁹ and the cerebellum¹⁵⁰. Increasing the frequency of the desired motion produced a delayed ME signal and performance weakened (**Fig. 4.4A**). This is produced by the frequency characteristics of the PD controller. An important implication of this result is that the neural circuit implementing the feedback controller converting SE into ME⁸¹ is required to be adequately tuned otherwise the ME signal can produce erroneous learning in the cerebellar circuit. Choosing a different feedback controller in our setup would require the adjustment of the difficulty of the control task (i.e., control objects and desired motions) to allow the disassociation of SE and ME as presented here, but should provide the same conclusions.

Our results also showed that a linear combination of SE and ME encoded in the CF is an adequate error signal in our cerebellar model to control successfully the plants. Performance attained was always better than when the cerebellar model was disabled (**Fig. 4.1-4.3H**, magenta lines). These results are in-line with physiological evidence in monkeys during arm reaching experiments that has suggested that CF encodes both SE and ME at different times of the arm movement⁸⁵, and thus, CF carries the error signal required for real-time control and learning of movements.

5

Mechanisms of asymmetrical cerebellar motor learning

 O acquire and maintain precise movement controls over a lifespan, changes in the physical and physiological characteristics of muscles must be compensated for adaptively. The cerebellum plays a crucial role in such adaptation. Changes in muscle characteristics are not always symmetrical. For example, it is unlikely that muscles that bend and straighten a joint will change to the same degree. Thus, different (i.e., asymmetrical) adaptation is required for bending and straightening motions. To date, little is known about the role of the cerebellum in asymmetrical adaptation. Here, we investigate the cerebellar mechanisms required for asymmetrical adaptation using the neuronal network model of the cerebellum presented in **Chapter 3** with a bi-hemispheric structure. The bi-hemispheric structure is inspired by the observation that lesioning one hemisphere reduces motor performance asymmetrically. The cerebellar model interfaced to the two-wheeled balancing robot. The load of the robot and its environment were modified to create asymmetrical perturbations. This CF input was configured to increase and decrease its firing rate from its spontaneous firing rate (approximately 1 Hz) with sensory errors in the preferred and non-preferred direction of each hemisphere, as demonstrated in the monkey cerebellum. Our results showed that asymmetrical conditions were successfully

handled by the cerebellar model, in contrast to a single hemisphere model or a classical non-adaptive proportional and derivative controller. Further, the spontaneous activity of the CF, while relatively small, was critical for balancing the contribution of each cerebellar hemisphere to the overall motor command sent to the robot. Eliminating the spontaneous activity compromised the asymmetrical learning capabilities of the cerebellar model.

5.1 Introduction

Development, aging, and injuries are common conditions that prevent the neural centers governing the muscles from being rigid and hard-wired. Thus, a key feature of these centers is adaptation. The cerebellum is one example of a neural center where adaptation is crucial. The cerebellum is involved in cognition^{102;115;153}, motor learning, and coordination^{57;69;101;145;152}. Adaptation in the cerebellum has been widely studied in eye movements such as smooth pursuit^{5;147}, the vestibuloocular reflex (VOR)^{8;15;60;67;94}, and saccades^{64;87} because these adaptations can be evoked easily under experimental conditions. For example, VOR gain, defined as eye velocity divided by head velocity during head turn, can be tuned up using a visual-vestibular mismatch stimulus^{3;77;108;116}. Under normal circumstances, the cerebellum exerts symmetrical control over the muscle plant of the eyes³²; however, when the muscle plant is changed by aging, lesions, or asymmetrical optics, the cerebellum must compensate for the abnormal conditions by adapting asymmetrically¹⁰⁴. Asymmetrical adaptation can also be elicited in the laboratory. The Vertical VOR gain can be increased in the up direction (i.e., downward head turn) and decreased in the down direction (i.e., upward head turn) simultaneously in monkeys^{61;155} and humans¹⁰⁴. In goldfish, the same type of asymmetrical VOR adaptation can be induced in the horizontal system¹⁶⁹. Saccades have also been shown to be asymmetrically tunable^{38;64;89;141}.

Despite these lines of experimental evidence, the loci and the neural mechanisms underlying asymmetrical adaptation are a matter of debate. Several possible loci have been proposed involved in VOR asymmetrical adaptation, including direction-sensitive and non-linear firing responses of gaze-velocity floccular Purkinje cells¹⁰⁴, or the floccular target neurons in the vestibular nucleus and the dorsal Y group^{7;61}. These loci constitute partially independent mechanisms for adaptive control of vertical VOR gain, whereas the bilateral pool of motor neurons innervating the muscles of the eye has been proposed to be the locus of dis-conjugate adaptation in saccades⁷⁶. A different hypothesis proposes that the asymmetrical mechanisms are closely related to the bi-hemispheric structure of the cerebellum^{22;113;117}. Lesions to the left cerebellar hemisphere lobule H-VII of the monkey significantly impair motor performance in the ipsiversive direction but also to a less degree in the

contraversive direction during smooth pursuit¹¹³. In a similar way, the adaptation of post-saccadic smooth pursuit velocity affects the ipsiversive direction¹¹³. Ipsilesional saccadic adaptation was significantly reduced following unilateral cerebellar hemisphere infarctions in humans²². These results suggest that a bi-hemispherical structure is necessary for asymmetrical motor adaptation and that the hemispheres are not completely independent.

Climbing fiber (CF) input is an important mechanistic link between the two cerebellar hemispheres. CF input has been proposed to carry the error signal required for long-term changes in the sensitivity of Purkinje cells to specific inputs from mossy fibers^{1;71;103}, for the more immediate and short-term effects on the simple spikes of Purkinje cells^{100;106}, and for the rapid and strong (phasic) override commands to Purkinje cells⁹⁵. Monkey experiments during horizontal VOR gain adaptation showed that the CF input encoded information about the amount and direction of the error^{58;59}. The major type of CF input in the left hemisphere increased its firing rate with ipsidirectional retinal error, whereas it decreased its firing rate below its spontaneous firing rate (approximately 1 Hz), with contradirectional retinal error. The CF input also showed similar characteristics during smooth pursuit experiments in monkeys¹⁴⁷. Therefore, assuming that CF input drives motor learning in the cerebellar circuit, adaptation in one hemisphere takes into account both the error information in its preferred direction and its non-preferred direction (i.e., in the preferred direction of the contralateral hemisphere).

5.2 Configuration of the model to produce asymmetrical adaptation

5.2.1 Low-DC firing rate in the CF

The CF input to the cerebellar model, which has been proposed to carry the error information required for driving plasticity at parallel fiber (pf)-Pk synapses as a basis for motor learning^{70;103}, is calculated in the model from the difference between the desired and actual motion^{61;69;70;124} (**Fig. 5.1B**). The CF input carries position and velocity error components in kinematic coordinates (expressed in angle units, rads). Sensory error (shown in **Fig. 5.1A**) was split into forward and backward errors (**Fig. 5.1B**) (sensory error > 0 , and sensory error < 0 , respectively) and spontaneous activity ($cf_{spont} = 0.05$) was added (**Fig. 5.1**). A reduction of the CF activity below its spontaneous rate (approximately 1 Hz) has been shown to correlate with sensory errors produced in the non-preferred direction^{58;59}. Thus, each hemisphere was configured to receive a CF input carrying information from mainly one direction of robot motion, i.e., the left hemisphere received mainly forward sensory er-

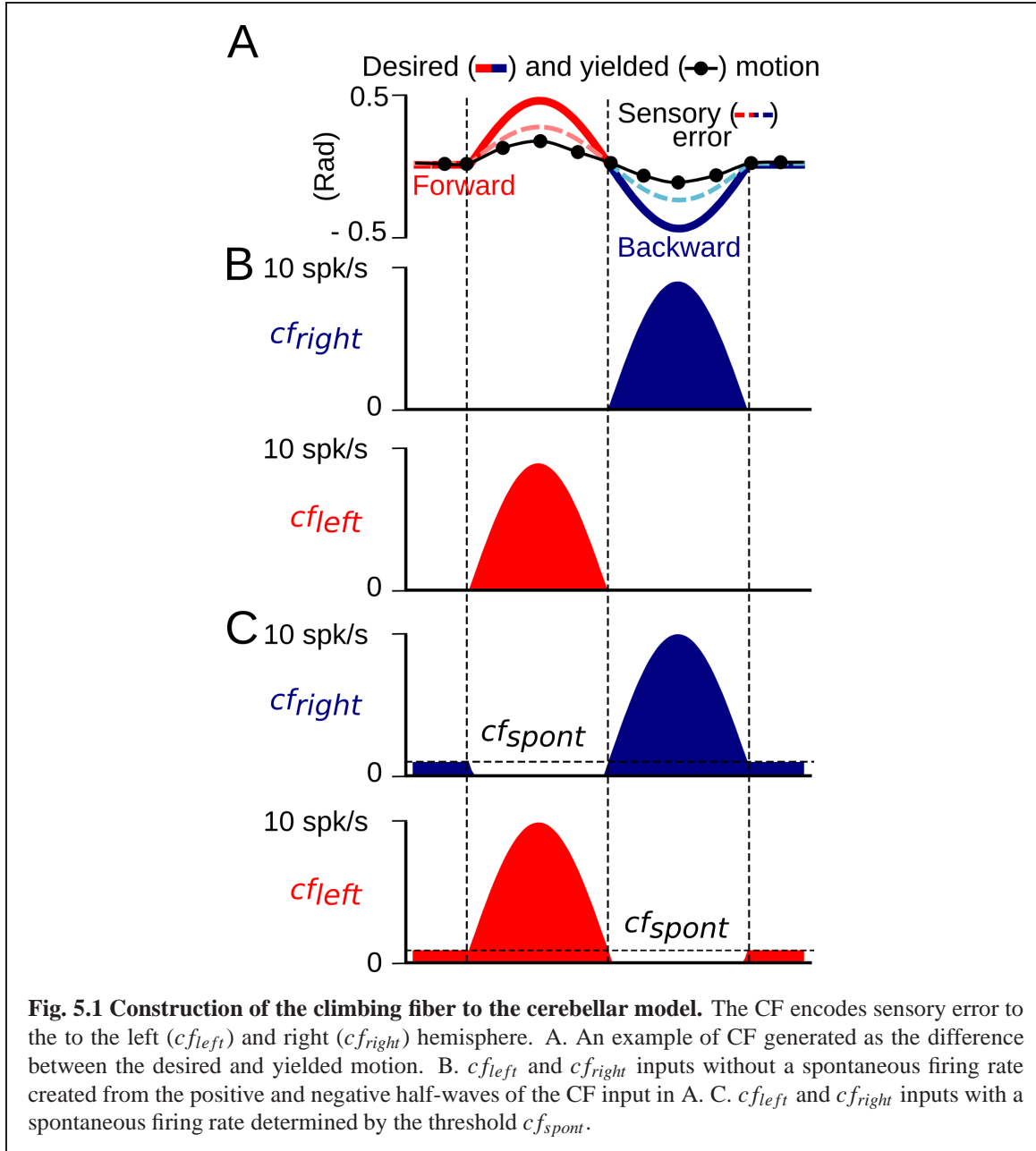
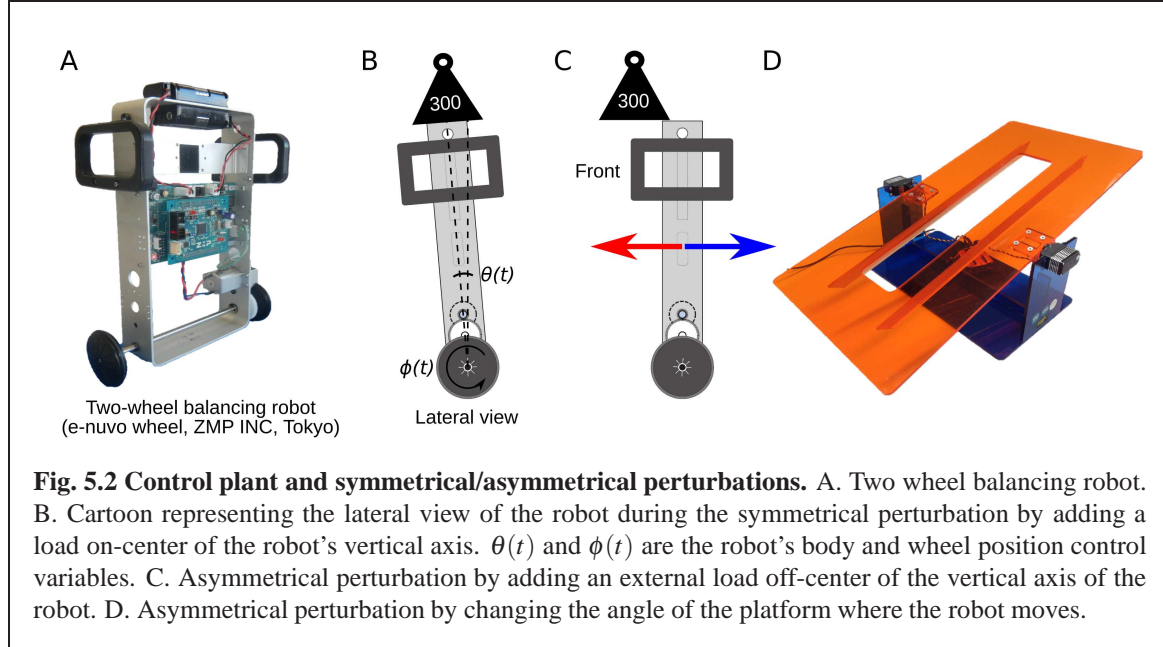


Fig. 5.1 Construction of the climbing fiber to the cerebellar model. The CF encodes sensory error to the left (cf_{left}) and right (cf_{right}) hemisphere. A. An example of CF generated as the difference between the desired and yielded motion. B. cf_{left} and cf_{right} inputs without a spontaneous firing rate created from the positive and negative half-waves of the CF input in A. C. cf_{left} and cf_{right} inputs with a spontaneous firing rate determined by the threshold cf_{spont} .

rror (Fig. 5.1B cf_{left}), whereas the right hemisphere receives backward sensory error (Fig. 5.1B cf_{right}). In this way, the CF increases its firing rate above the cf_{spont} level with erroneous motion in the preferred direction, whereas, erroneous motions in the non-preferred direction causes a reduction of the CF firing rate below the value cf_{spont} .



5.2.2 Experimental protocol

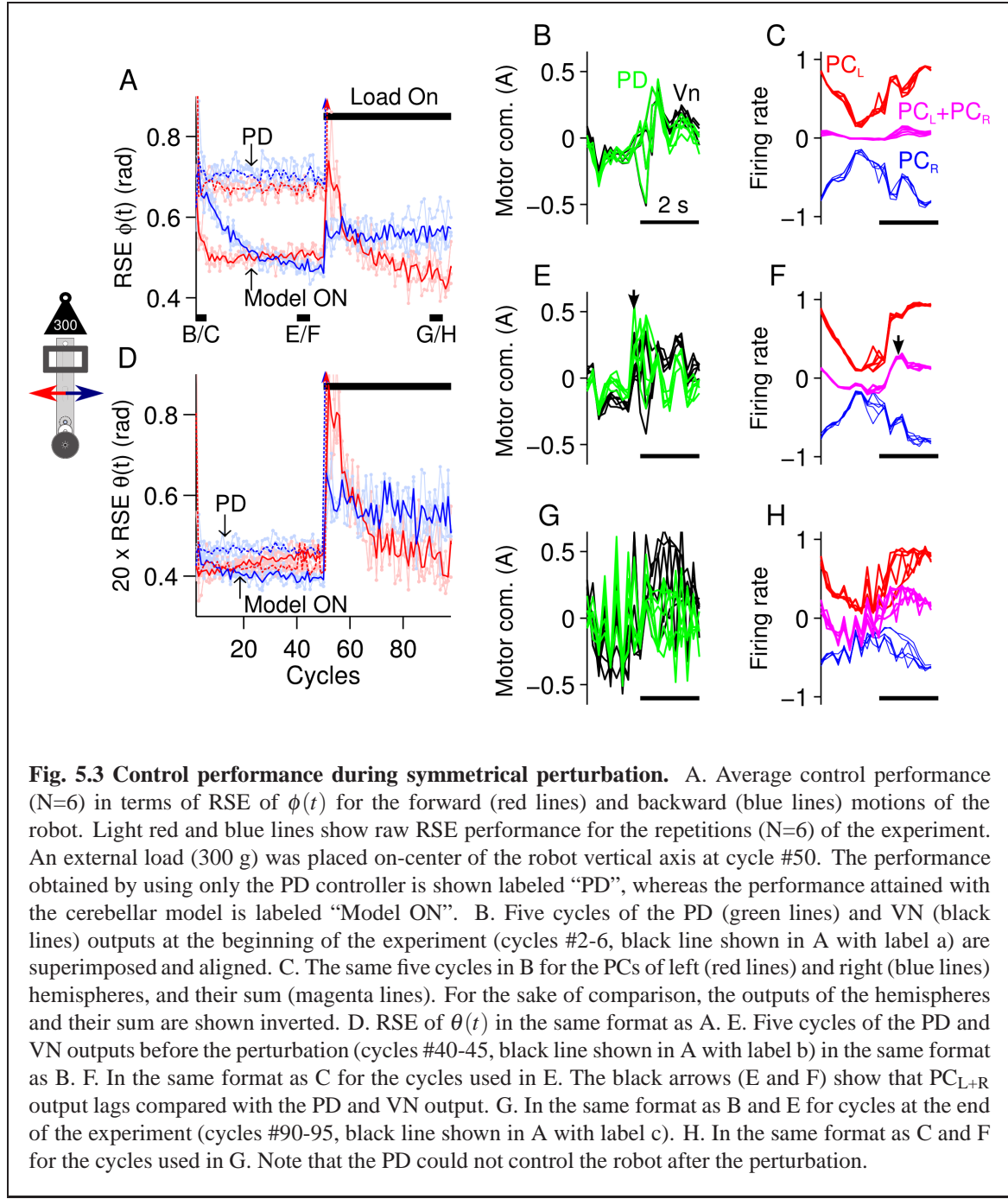
For the experiments presented in this chapter, the cerebellar model was configured with a bi-hemispheric structure (**Fig. 3.1D**) with the number of cells consigned in **Table 3.1**. The two-wheel balancing robot (e-nuvo wheel, ZMP INC, Tokyo) (**Fig. 3.2B**) is used here. The robot is considered one of the most challenging control plants⁹². The desired body tilt angle $\theta_{ref}(t)$ and velocity $\dot{\theta}_{ref}(t)$ were set to zero radians, so that the robot is commanded to remain vertical while following the desired wheel angle trajectory, which was set to a sinusoidal motion $\phi_{ref}(t) = \pi \sin(2\pi 0.25t)$. These seven MFs of these control plant (**Table 3.1**) were repeated 81 times to generate the 562 MFs required in the cerebellar model. Perturbations to the robot, symmetrical and asymmetrical, were created by placing an external load (300 g, 50% of robot's mass) on the top and center of the vertical axis of the robot (symmetrical load depicted in **Fig. 5.2B**), off-center on the front/back (asymmetrical load depicted in **Fig. 5.2C**), or by changing the angle of the platform on which the robot was moving (depicted in **Fig. 5.2D**).

5.3 Results

5.3.1 Symmetrical control scenario

Before exploring the asymmetrical capabilities of the cerebellar model, in this section, a symmetrical control scenario was tested to contextualize the need for a bi-hemispherical structure. The control scenario employed consisted of 100 cycles of the sinusoidal desired motion ($\phi_{ref}(t) = \pi \sin(2\pi 0.25t)$, $\theta_{ref}(t) = 0$) for the robot. Control of the robot remained undisturbed until cycle #50, when an external symmetrical perturbation, a load of 300 g or 50% of the robot's mass, was placed on-center of the vertical axis of the robot (depicted in **Fig. 5.2B**), thus causing a close-to-symmetrical perturbation to the robot. **Fig. 5.3** summarizes the control performance attained and shows that the cerebellar model was able to control the robot and compensate for the external perturbation. The control performance, measured as the root mean square error (RSE) of $\phi(t)$ (**Fig. 5.3A**) and $\theta(t)$ (**Fig. 5.3D**) of the forward (red lines) and backward (blue lines) motions of the robot (positive and negative half-rectified waves of $\phi_{ref}(t + 10 \text{ sec})$, respectively), shows that during the initial 20 cycles of the desired motion, the cerebellar model adapted to reduce the RSE on each of the robot's control variables (highly marked in the RSE of $\phi(t)$). The benefit of using the cerebellar model in this control scenario is clearly recognized by comparing the RSE with the one achieved by using only the PD controller (**Fig. 5.3A,D** lines labeled as "PD"). The average improvement (along a total of 6 repetitions of the experiment) was $0.229 \pm 0.010 \text{ rad}$ (forward), $0.277 \pm 0.016 \text{ rad}$ (backward) and $(0.0348 \pm 0.010)/20 \text{ rad}$ (forward), $(0.0809 \pm 0.022)/20 \text{ rad}$ (backward) for $\phi(t)$ and $\theta(t)$, respectively. Furthermore, the PD controller alone always failed to control the robot after the external load was added (**Fig. 5.3A** PD arrows towards infinity after cycle #50). In contrast, **Fig. 5.3A,D** show that after the external load was placed on-center along the robot's vertical axis (cycle #50-100), the cerebellar model re-adapted its output to maintain adequate control of the robot and reduced the RSE. In this control scenario, the RSE of $\theta(t)$ was more affected than $\phi(t)$ because the extra inertia produced by the perturbation made it more difficult to achieve vertical alignment of the robot's body (i.e., $\theta(t) \neq 0$). In addition, the RSE performances shown in **Fig. 5.3A,D** (cycles #1-50) imply that the forward (red lines) and backward (blue lines) motions of the robot are inherently different. These differences are mainly due to the intrinsic asymmetries of the mechanics of the robot, which were more accentuated when the perturbation was added (**Fig. 5.3A,D**, cycles #50-100).

The changes to the cerebellar model output produced by the adaptation in the left and right hemispheres are shown in **Fig. 5.3C, F and H** (magenta, red and blue lines, respec-



tively). These figures show five superimposed cycles of the firing rate of the cerebellar model, left and right hemisphere, at the beginning (**Fig. 5.3C**, cycles #2-6, black line shown in **Fig. 5.3A** with label B/C), before the perturbation (**Fig. 5.3F**, cycles #40-45, black line shown in Fig. 5.3A with label E/F), and at the end of the experiment (**Fig. 5.3H**, cycles #90-95, black line shown in **Fig. 5.3A** with label G/H). For the sake of comparison, **Fig.**

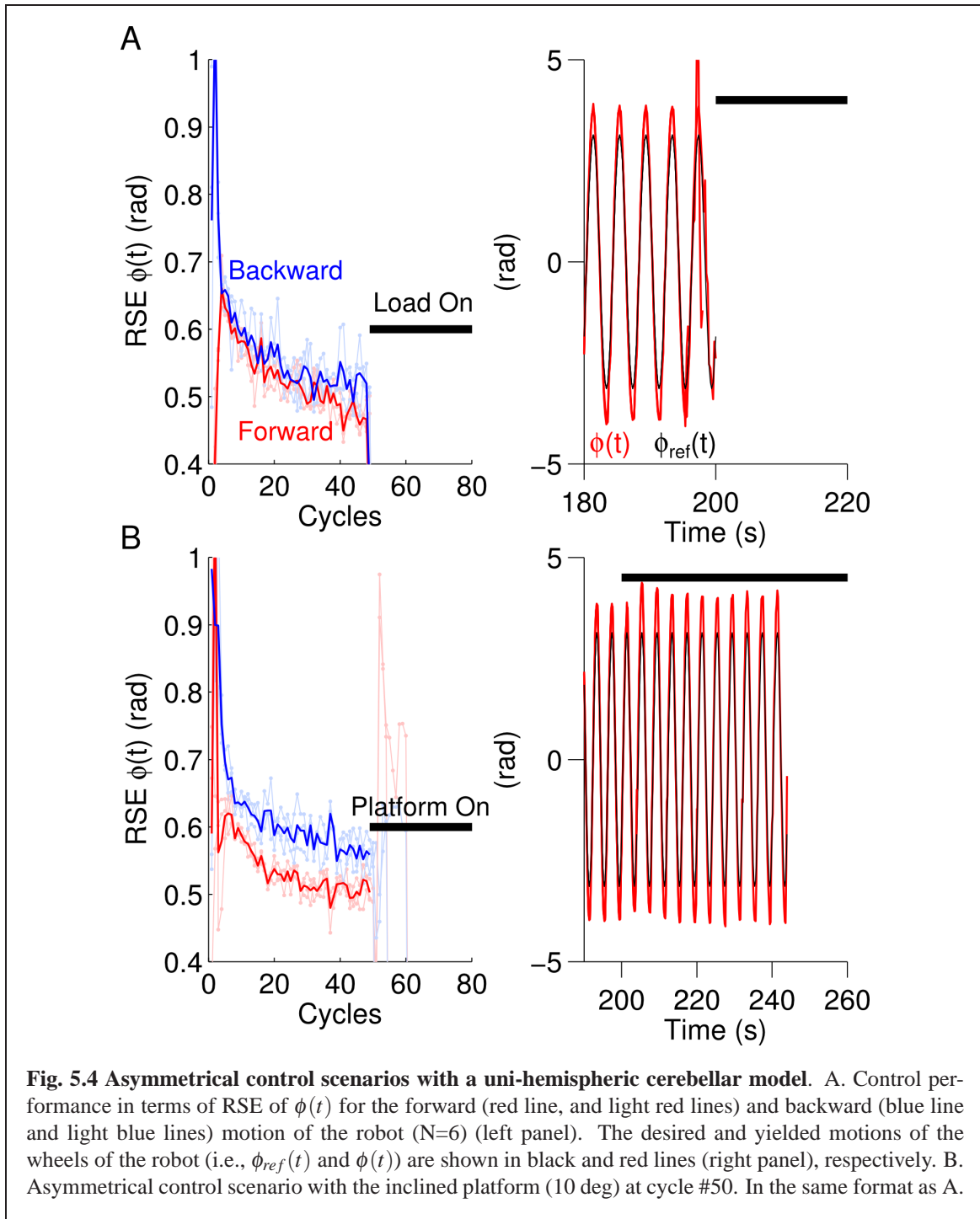


Fig. 5.4 Asymmetrical control scenarios with a uni-hemispheric cerebellar model. A. Control performance in terms of RSE of $\phi(t)$ for the forward (red line, and light red lines) and backward (blue line and light blue lines) motion of the robot ($N=6$) (left panel). The desired and yielded motions of the wheels of the robot (i.e., $\phi_{ref}(t)$ and $\phi(t)$) are shown in black and red lines (right panel), respectively. B. Asymmetrical control scenario with the inclined platform (10 deg) at cycle #50. In the same format as A.

5.3B, E and G show the corresponding five cycles of the PD (green lines) and VN (black lines) outputs. At the beginning, when the PC cells were untrained, the default hemisphere outputs canceled each other out, resulting in a small cerebellar output (**Fig. 5.3C**). During

this period, the non-cerebellar pathway (i.e., the PD output) was the output contributing the most to the VN (**Fig. 5.3B**, PD and VN lines are almost equal). Then, by cycles #40-45, plasticity at the pf-PC synapses driven by the CF input caused different modulations of the firing rate of each hemisphere (i.e., average firing rate of the PC cells), reflecting the intrinsic differences of the forward and backward motions of the robot (**Fig. 5.3F**, red and blue lines). The addition of these two outputs produced the cerebellar model output (**Fig. 5.3F**, magenta lines), which contributed with the PD controller (**Fig. 5.3E**, green line) to the VN output, i.e., the motor command sent to the robot. Note that the PD and the VN outputs were no longer equal, meaning that the cerebellar model was contributing to the VN output. The apparent phase lag between the cerebellar model and the PD output (**Fig. 5.3E,F** black arrows) is a direct cause of using a sensory error signal as the CF input in our model¹²⁴. This phase difference suggests that the cerebellar model output adapted to cooperate with the non-cerebellar pathway input to the VN (i.e., the PD output) to generate the motor command to the robot¹²⁴. At the end of the experiment (**Fig. 5.3G,H**), the PD output was severely affected by the external perturbation, whereas the cerebellar model output increased its amplitude by 60% (in comparison with the value before the perturbation). Interestingly, this net increase in the cerebellar model output was caused by changes in the shape of the outputs of the hemispheres, which reflected a reduction of their peak-to-peak firing rate (17% and 23% left and right hemispheres, with respect to the values before the perturbation), reflecting the LTD occurring with the increase in the error signal produced by the external load. As a result of the adaptation in the cerebellar model, the motor command remained adequate to compensate for the extra load and reduced the RSE (**Fig. 5.3A,D** (cycles #50-100)).

In the present close-to-symmetrical control scenario, the cerebellar model hemispheres successfully learned the control sequences that reduced the error signal in the CF input and successfully controlled the robot at different frequencies of the desired motion (**Fig. 5.5**). However, a bi-hemispheric structure is not essential for this control scenario, because a uni-hemispheric cerebellar model is also able to control the robot and compensate for the external perturbation when the load is placed on-center of the robot¹²⁴. Thus, the performance attained with the cerebellar model was not different from the one attained with a uni-hemispheric configuration in this control scenario. However, when asymmetrical loads are considered, the uni-hemispheric model is not able to control the robot (**Fig. 5.4**). In the next section the capability of the cerebellar model to handle asymmetrical conditions is tested.

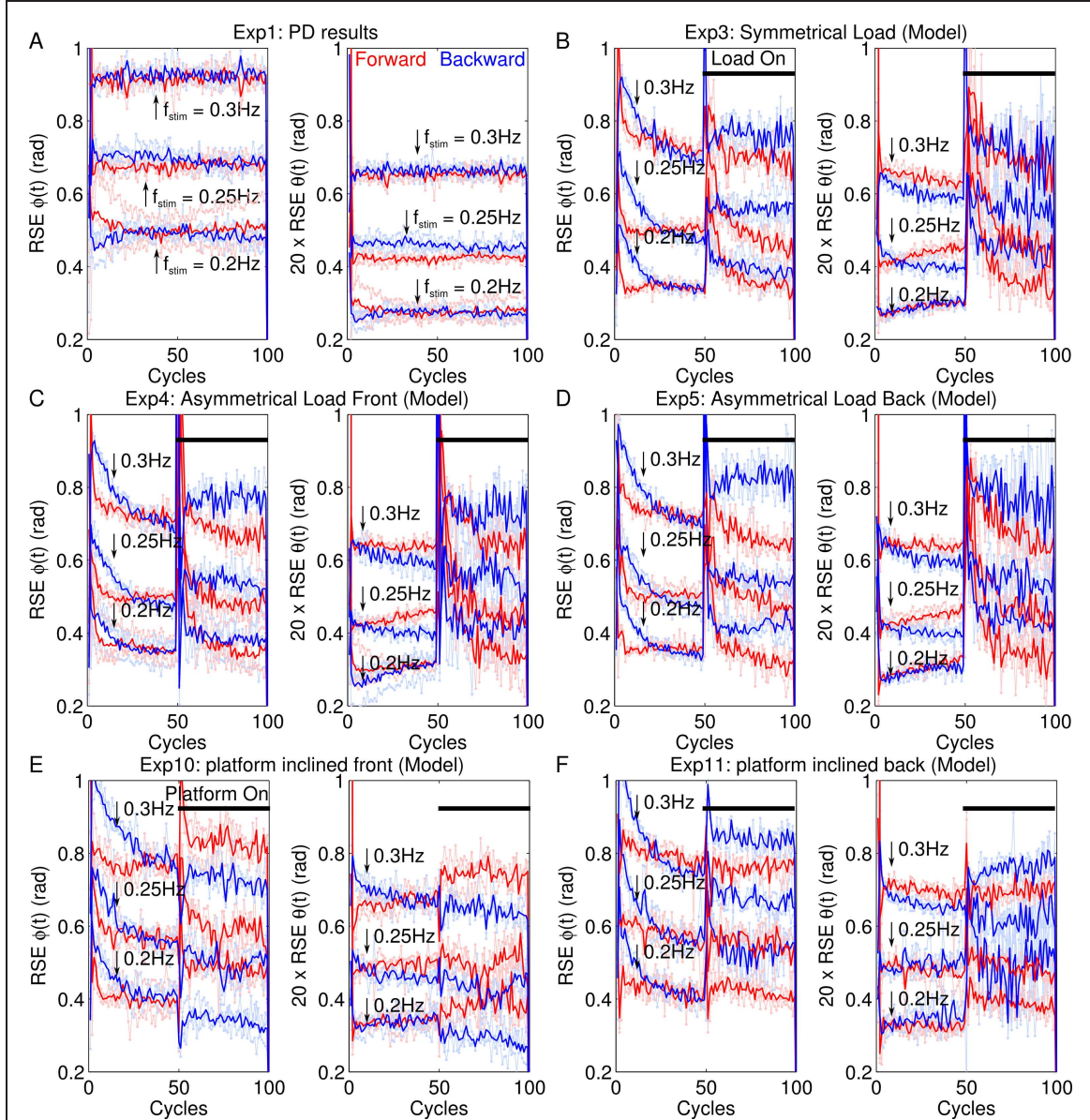
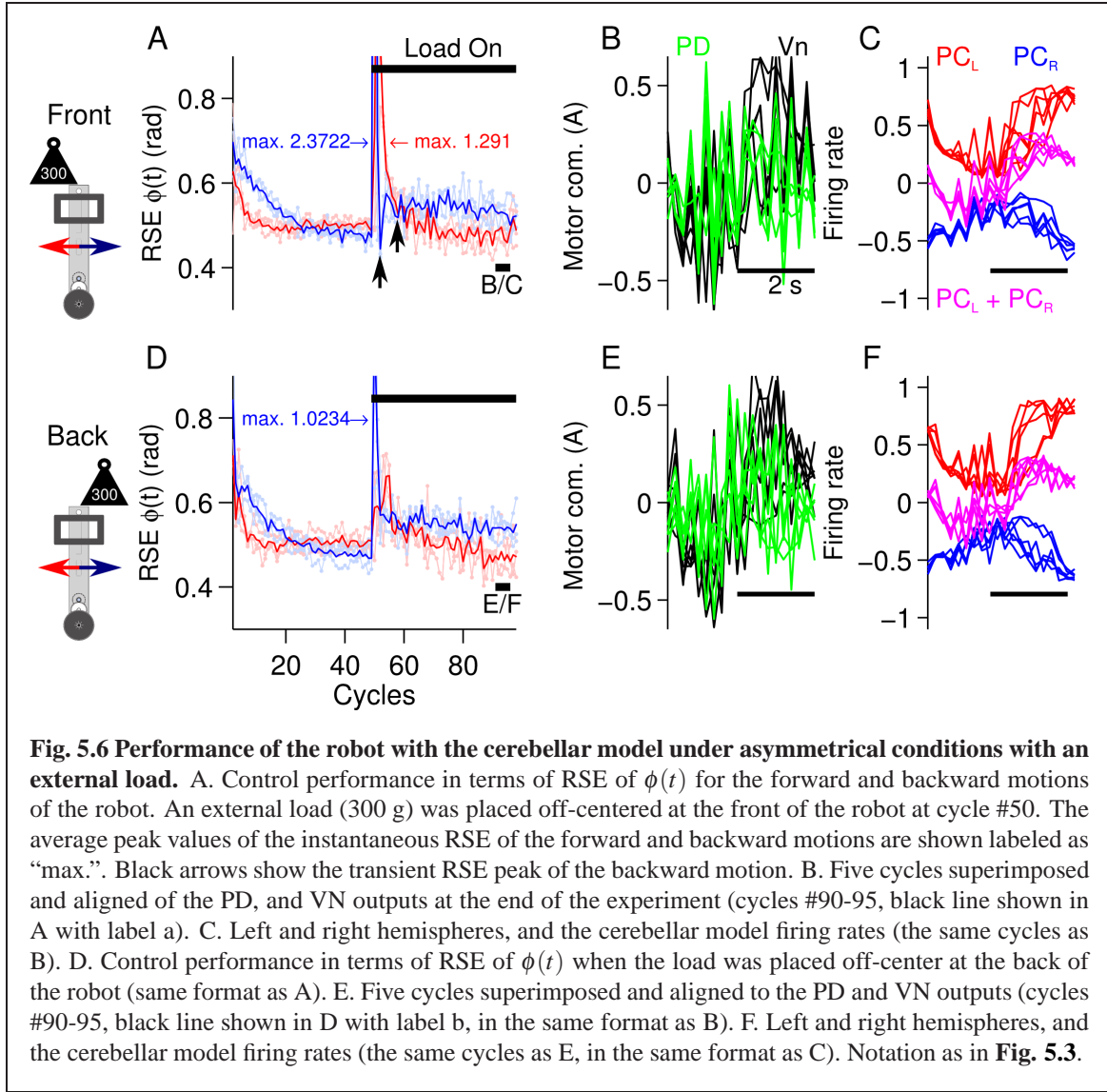


Fig. 5.5 Comparison of the performance achieved during control of the robot at different frequencies of the desired motion and different perturbations (symmetrical and asymmetrical). A. Baseline performance obtained when using only the PD controller. Average control performance (total number of repetitions of the experiment $N=6$) and raw performances in terms of RSE of $\phi(t)$ for the forward (red line, and light red lines) and backward (blue line and light blue lines) motion of the robot. The frequency of the stimulus ranged from 0.2 to 0.3 Hz as indicated in each figure. B. Performance during the close-to-symmetrical control scenario. C. Performance during the asymmetrical scenario (load to the front). D. Performance during the asymmetrical scenario (load to the back). E. Performance when the platform where the robot moved was inclined 10 degrees. F. Performance when the platform was declined 10 degrees.

5.3.2 Asymmetrical control scenario

To evaluate the cerebellar model during asymmetrical control scenarios, the previous stimulus was repeated. The cerebellar model was commanded to follow a sinusoidal ($\phi_{ref}(t) = \pi \sin(2\pi 0.25t)$, $\theta_{ref}(t) = 0$) motion for 100 cycles. In the first asymmetrical condition, the same external load as used in the symmetrical control scenario (300 g, which corresponds to 50% of the robot's mass) was placed on the robot off-center to the front or back from its vertical axis (depicted in **Fig. 5.2C**) at cycle #50, producing an asymmetrical control scenario for the cerebellar model. The second asymmetrical scenario was constructed by changing the angle of the platform on which the robot was moving (see below, depicted in **Fig. 5.2D**). In the case of the external load, the perturbation was added to the front or back of the robot in two separate experiments (each experiment was repeated three times) to account for the intrinsic differences in the forward and backward motions of the robot. **Fig. 5.6** shows that the cerebellar model was able to learn to produce the motor commands required for compensating for the first asymmetrical scenario. **Fig. 5.6A** is the same format as **Fig. 5.3A** and shows the RSE of $\phi(t)$ for the forward and backward motions of the robot when the load was placed off-center to the front of the robot, demonstrating that forward motion was more affected than backward motion. The backward motion showed a larger average instantaneous peak RSE (2.372 rad) than the forward motion (1.292 rad). However, backward motion rapidly fell below the RSE of the forward motion (**Fig. 5.6A** black arrows). The reduction in the forward motion of the robot can be easily observed by comparing the RSE of the forward motion during the symmetrical control scenario (**Fig. 5.3A** red line, cycles #50-60). In contrast, when the load was placed off-center to the back of the robot (**Fig. 5.6D**), the backward motion was more affected (average peak RSE 1.023 rad). These results confirm that the conditions in this first control scenario were asymmetrical.

Fig. 5.6A,D also show that the cerebellar model was able to adapt and reduce the transitory error produced by the asymmetrical perturbation, so that by the end of the experiment, the RSE values (**Fig. 5.6A-D**, cycles #90-100) were close to those before the external load was added (**Fig. 5.6A-D**, cycles #40-45). The outputs of the PD, the Vn, left and right hemispheres, and the cerebellar model firing rates (**Fig. 5.6B, C, E, and F**) reflected the external perturbations. During either condition (load to the back or front), the PD output showed large peaks. With respect to the values before the perturbation, the cerebellar model increased its output by 79% and 73% when the load was off-center to the back and front, respectively. On the contrary, the average peak-to-peak firing rate of the left hemisphere (**Fig. 5.6C, F**, red lines), which mainly received error information from the forward motion via c_{left} , decreased by 16% and 17%, respectively, indicating the preference of this hemisphere to forward motion (a larger reduction caused by LTD). The right hemisphere, which



mainly received error information from the forward motion via cf_{right} , decreased by 36% and 28%, showing the opposite preference.

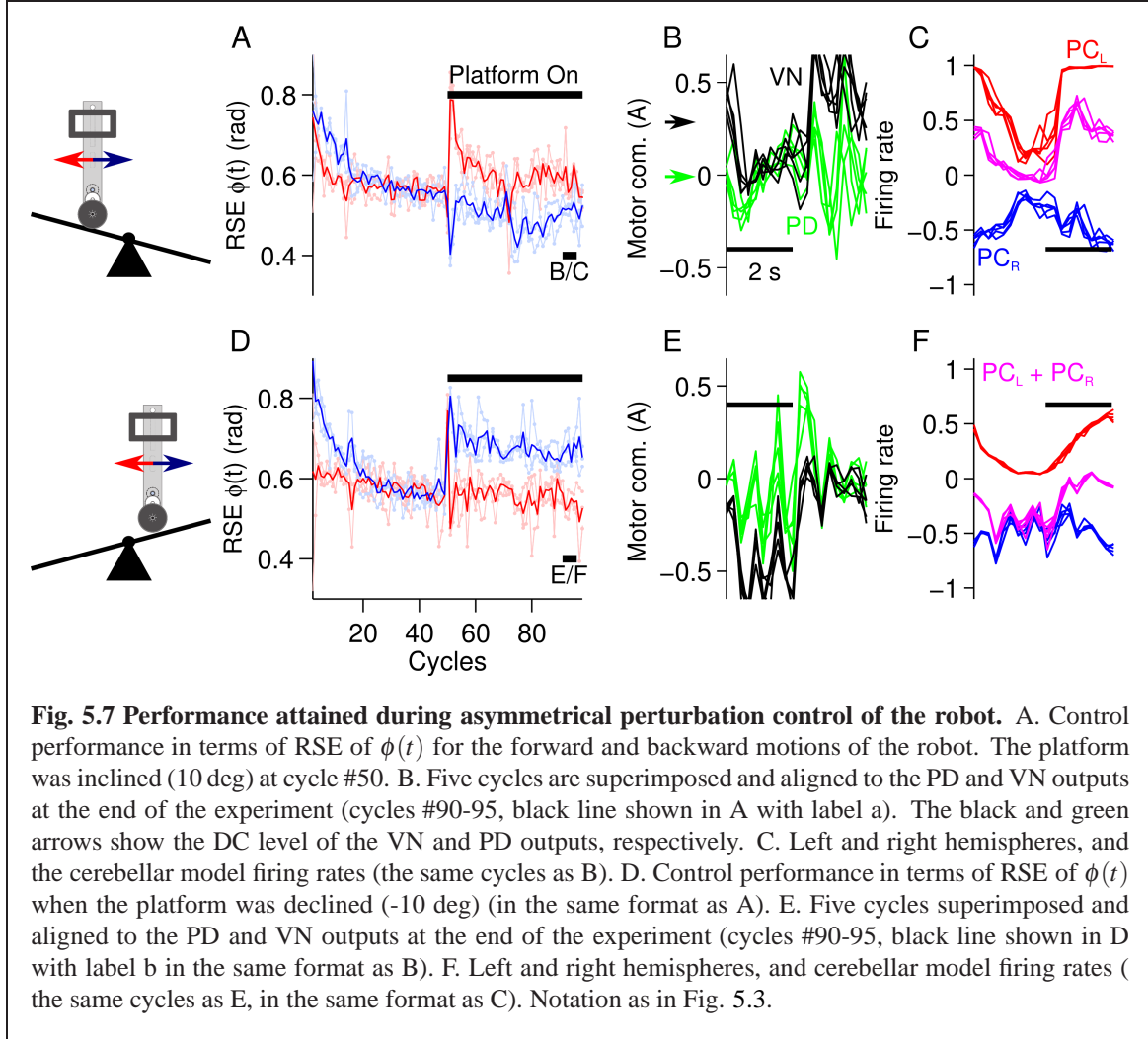
In this first asymmetrical control scenario, the cerebellar model was able to account for the asymmetrical condition, despite the change in the dynamics of the control plant. Similar results were found at different frequencies of the desired motion (**Fig. 5.4**). A uni-hemispheric cerebellar model was not able to control the robot (**Fig. 5.4**). In the second asymmetrical control scenario (i.e., using the platform shown in **Fig. 5.2D**), we further studied the capabilities and generalization of the cerebellar model during a more challenging asymmetrical motor control task.

The second asymmetrical scenario consisted of changing the environment of the robot by

inclining or declining the platform where the robot moved (**Fig. 5.2D**). Following the same experimental protocol as in the previous scenarios, the angle of the platform was changed ± 10 degrees at cycle #50, and the desired motion was maintained for 100 cycles in total. **Fig. 5.7** shows the results in the same format as **Fig. 5.6**. In general the cerebellar model was able to account for inclinations of ± 10 degrees by adapting its output. **Fig. 5.7A,D** show the performance in terms of RSE of $\phi(t)$. There is clear evidence of causation between the motion affected and the asymmetrical conditions, that is, the forward motion was more affected than the backward motion when the robot had to climb the platform in the forward direction (platform inclined), whereas the backward motion was more affected when the robot had to climb in a backward motion (platform declined). This result confirmed our intention of constructing an asymmetrical control scenario for the cerebellar model. **Fig. 5.7A,D** also indicated that the cerebellar model adapted and reduced its error in the forward direction (**Fig. 5.7A** red lines) to a larger extent than in the backward direction (**Fig. 5.7D** blue lines), reflecting once more the intrinsic differences in the mechanics of the robot (also shown in **Fig. 5.3**). **Fig. 5.7B,E** show the PD and VN outputs, and **Fig. 5.7C,F** show the outputs of the left and right hemispheres and the cerebellar model firing rates in the same format as **Fig. 5.6B,C**. These data demonstrate the active role of the cerebellar model in producing the VN output. When the robot climbed the platform in the forward direction, the VN output (**Fig. 5.7B** black lines and black arrow) produced a positive DC value (approx. 0.3 A) to compensate for the asymmetrical environment. This value was not produced by the PD output because it remained at a zero DC level (**Fig. 5.7B** green lines and green arrow) but was produced by the increased DC level of the cerebellar model firing rate (**Fig. 5.7C** magenta lines). The same behavior occurred when the robot climbed in the backward direction (**Fig. 5.7F**). **Fig. 5.7C,F** show the changes in the modulation of the output of the left and right hemispheres (i.e., the average firing rate of the PC cells) that occurred with the different asymmetrical conditions. The left hemisphere changed from a square-like modulation when the platform was inclined (**Fig. 5.7C**) to a sinusoidal-like modulation when the platform was declined (**Fig. 5.7F**). These results demonstrate the asymmetrical adaptation that occurred in the cerebellar model to compensate for asymmetrical perturbations to the control plant. Similar results were obtained at different frequencies of the desired motion (**Fig. 5.4**).

5.3.3 Effect of the CF low-DC firing rate in the model

A critical component of the cerebellar model is the CF input that drives plasticity at the pf-PC synapses. The CF input in the current model is sensitive to errors happening in a specific direction and also includes spontaneous (cf_{spont}) activity. The CF input increases its firing



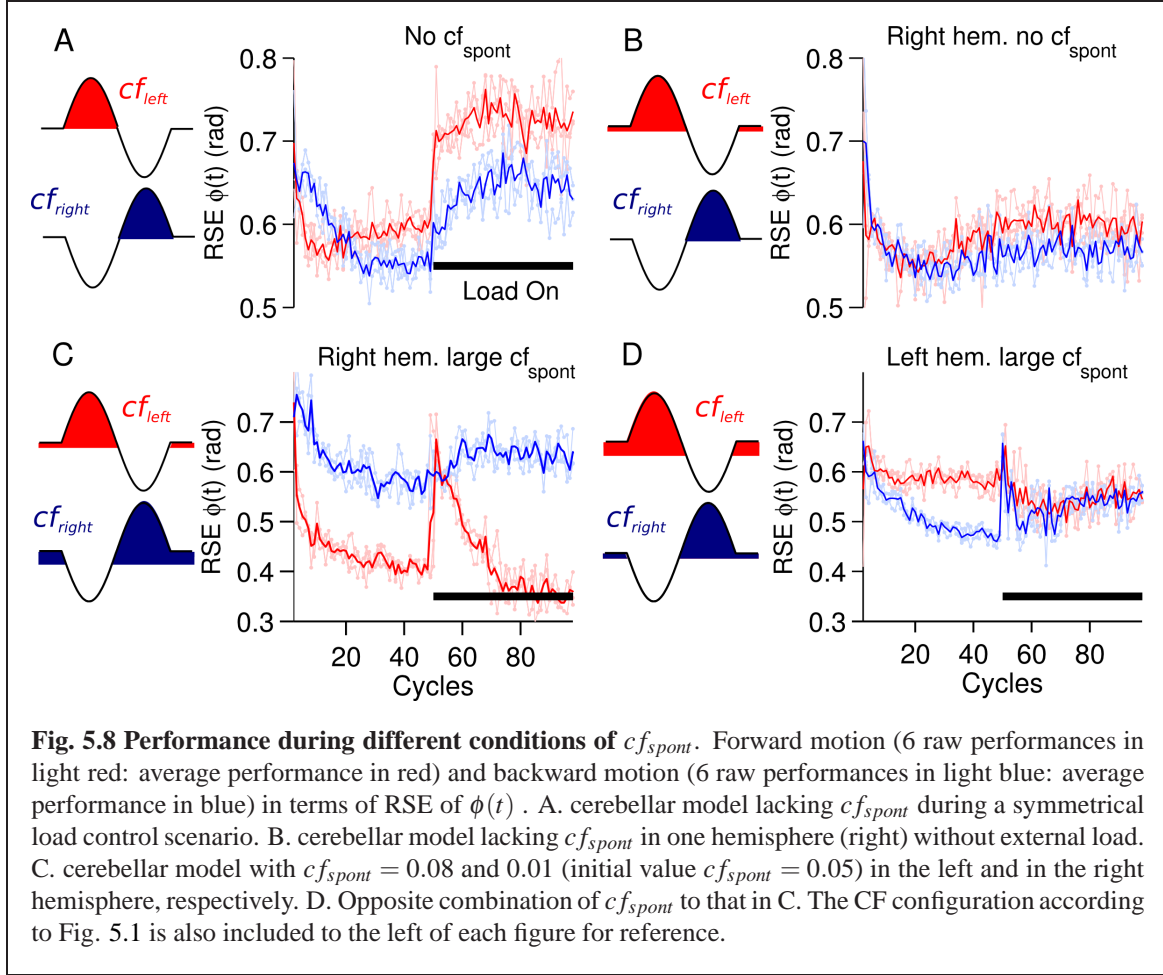
rate with motion errors in the preferred direction (ipsidirectional) and decreases its firing rate below the $c_{f,spont}$ to a zero minimum with motor errors occurring in the non-preferred direction (contradirectional) of each hemisphere. To assess the importance of $c_{f,spont}$, we performed a comparison between a CF input lacking spontaneous activity and the results obtained thus far. The cerebellar model lacking $c_{f,spont}$ was able to control the robot during the close-to-symmetrical control scenario. The control performance in terms of RSE of $\phi(t)$ is shown in **Fig. 5.8A** in the same format as **Fig. 5.3A**. However, the cerebellar model lacking $c_{f,spont}$ could not decrease the RSE after perturbations during the asymmetrical condition (data not shown). Thus, the performance obtained with the cerebellar model lacking the spontaneous firing rate in CF is similar to that obtained with a uni-hemispheric cerebellar model¹²⁴. These results suggest that the $c_{f,spont}$ is critical for asymmetrical control with the cerebellar model. To further evaluate the importance of $c_{f,spont}$, an additional test including

the cf_{spont} in only one of the hemispheres (left) was carried out. The control performance attained in terms of RSE of $\phi(t)$ is shown in **Fig. 5.8B**. The result, which corresponds to 100 cycles of the sinusoidal desired motion without any external perturbation, shows that the cerebellar model initially reduced the RSE (cycle #1-30) but could not sustain this reduction for long. This is because the left hemisphere lacked the contralateral error information in CF and could not change its output to account for inadequate outputs produced by the intact hemisphere, thus endangering the balance of the hemispheres and the overall output of the cerebellar model. If such a relationship were true, the balance between the hemispheres and the performance of the model should be tunable by changing the value of the cf_{spont} in each hemisphere. **Fig. 5.8C, D** show that this is the case. **Fig. 5.8C** was obtained by setting the value of $cf_{spont} = 0.08$ and 0.01 (the initial value of cf_{spont} was 0.05) in the right and left hemisphere, respectively. Performance was compromised in the backward direction, which is mainly driven by the right hemisphere receiving the CF with large cf_{spont} . **Fig. 5.8D**, which was obtained by setting the values in the opposite order, shows the opposite relationship. The performance of the backward direction was affected but the forward direction was severely decreased. Therefore, the CF input, which is direction sensitive in the cerebellar model, is critical for asymmetrical control because it balances the contribution of each hemisphere. The information about errors occurring in the non-preferred direction conveyed by the CF input via a reduction of its firing rate below its spontaneous rate proved to be critical for the cerebellar model during the asymmetrical control scenario.

5.4 Discussion

We developed a bi-hemispheric neuronal network model of the cerebellum (the cerebellar model) that closely mimics anatomical and physiological characteristics of the cerebellar cortex. We included a direction-sensitive climbing fiber (CF) input that encoded sensory error information by altering its spontaneous firing rate to investigate the mechanisms required for asymmetrical motor learning. Our results showed that the bi-hemispheric structure is critical for asymmetrical motor learning, but it also requires a mediator to balance the contribution of the two hemispheres. Here, that role is filled by the CF input, as discussed below.

The cerebellar hemispheres are asymmetric in macrostructure and function^{65;144;167}. The level of asymmetry is subject dependent and has been proposed to be correlated with the level of skill that is required for a particular task¹⁴². Unilateral hand movement tasks without learning components activate the ipsilateral cerebellum, whereas moving the non-dominant hand or complex hand movements are associated with a more bilateral activa-



tion pattern in the cerebellum, which supports the suggestion that non-dominant or complex hand movements require more coordinated control from the cerebellum^{65;72}. Cerebellar asymmetries have also been found to correlate with handedness for tool use in apes¹⁶. The results of the control engineering experiments carried out here with the cerebellar model are in line with this evidence. On one hand, the asymmetrical conditions imposed on the robot demanded the generation of motor commands compensating for the unbalanced dynamics induced in the robot. These motor commands were adequately generated by the cerebellar model (**Fig. 5.6** and **Fig. 5.7**). On the other hand, control of the two-wheel balancing robot in response to a close-to-symmetrical external perturbation was well handled by the cerebellar model (**Fig. 5.3**) or by uni-hemispheric version¹²⁴. More complex control scenarios, including asymmetrical conditions, were handled only by the cerebellar model (**Fig. 5.6** and **Fig. 5.7** and **Fig. 5.4**). Thus, the bi-hemispherical structure reproduced a form of asymmetrical motor learning observed in the real cerebellum, and also proved to be critical

for compensating for complex control tasks (i.e. asymmetrical control conditions) during our control engineering experiments.

Lesioning of the cerebellar hemispheres compromises both the ipsilateral and contralateral motor performance. Monkey experiments have shown that the speed of saccadic eye movements was affected in the ipsiversive and contraversive directions when one cerebellar hemisphere (H-VII) was lesioned¹¹³. Unilateral cerebellar hemisphere infarction in humans also significantly reduced ipsilateral saccadic adaptation²². The results presented here demonstrate that the control performance in the forward and backward motion of the robot, which was directly related with the left and right hemisphere outputs, respectively, were affected not only when the asymmetrical perturbation was added to the ipsidirectional side of the robot but also (albeit in a lesser degree) when the perturbations were located on the contradirectional side of the robot (**Fig. 5.6A, D** and **Fig. 5.7A, D** red and blue lines). Furthermore, the results of the present model suggest a mechanism that explains the interaction observed between the cerebellar hemispheres. This mechanism involves the CF input, which drove the plasticity at PF-PC synapses in each hemisphere. This inputs increased its firing rate above its spontaneous firing rate with ipsidirectional erroneous motions, whereas it reduced its firing rate with contradirectional erroneous motions. This configuration of CF input has been suggested in monkey experiments, where complex spike activity of PC cells is highly correlated with CF activity. In the monkey, CF input conveys direction-sensitive motor error by increasing its firing rate and also information of the non-preferred direction by reducing its firing rate or presenting firing pauses during horizontal VOR adaptation^{58;59}. Our results reinforce the relevance of this configuration of the CF input (**Fig. 5.8**). The CF worked as a differential link that balanced the contribution of each hemisphere to the overall input to the Vn. Removing or adjusting the spontaneous firing rate of the CF resulted in a reduction of motor performance or completely abolished the system's ability to compensate for an asymmetrical perturbation of the robot. Therefore, a bi-hemispheric structure with direction selective CF input and adequate spontaneous CF activity is critical for cerebellar asymmetrical motor learning.

6

Role of the abundant number of cerebellar granule cells

HE cerebellar granule cells (GCs) have been proposed to perform lossless, adaptive spatio-temporal coding of incoming sensory/motor information required by downstream cerebellar circuits to advocate motor learning, motor coordination, and cognition. Here we use the neuronal network model of the cerebellum presented in **Chapter 3** to selectively enable/disable the output of GCs and evaluate the behavioral and neural consequences during three different control scenarios. The control scenarios are the simple direct current motor, the unstable two-wheel balancing robot, and the simulation model of a quadcopter. Results showed that adequate control was maintained with a relatively small number of GCs (< 200) in all the control scenarios. However, the minimum number of GCs required to successfully govern each control plant increased with their complexity. It was also shown that increasing the number of GCs resulted in higher robustness against changes in the initialization parameters of the cerebellar model (i.e., synaptic connections and synaptic weights). Therefore, we suggest that the paramount number of GCs in the cerebellar cortex might provide the computational power during the large repertoire of motor activities and motor plants the cerebellum is involved with, and might bring robustness against changes in the cerebellar microcircuit (e.g., neu-

ronal connections).

6.1 Introduction

Cerebellar granule cells (GCs) are the smallest and most numerous neurons in the central nervous system of vertebrates⁶⁹. Four dendrites and a long axon that bifurcates in two parallel fibers characterize the GCs^{6:69}. Due to this specialized morphology, theoretical works and computational studies have suggested that the GCs perform high dimensional lossless sparsification of incoming information, which is required at downstream cerebellar circuits to perform associative learning^{1;26;103;107;140}, adaptive filtering^{31;42}, binary addressing⁷⁵, and motor acquisition and consolidation⁴³. Yet, reaching a consensus has been hampered by the outstanding challenges at isolating, recording, and stimulating these cells. Pioneer experiments with animal models have attempted at clarifying the role of the GCs by abolishing completely or partially their output by blocking neurotransmitter release from all GCs^{84;159}, eliminating all GCs²⁹, or knocking down of calcium channels from a majority of GCs⁴³. Nonetheless, these works cannot address directly the role of the abundant GCs because they alter the balance at the input layer of the cerebellum and compensatory mechanism might affect their conclusions. Thus, a different framework is required.

Understanding the functional consequence of the abundant GCs is not only important for deepening our knowledge of the biological system, but also for engineering applications that employ computational models of the cerebellum^{18;46;63;124;151;158;168}. Adequate selection of the number of GCs could improve the ratio of energy consumption and control performance, improve robustness, and gain generalization of the cerebellar model¹¹¹. Yet, there has not been any evaluation in real world engineering application. Thus we tested the role of the GCs in real world engineering application using our bi-hemispherical neuronal network model of the cerebellum that incorporates realistic cerebellar network architecture and learning algorithm whose validity has been proved in both simulation and real-world experiments^{122;123}. The cerebellar model enables us to isolate the GCs, knock down their output while maintaining the integrity of the cerebellar circuit, and evaluate the motor performance attained during control of different plants. Using this framework we can clearly conclude on the role of the numerous GCs in an engineering point of view.

We demonstrate that the abundant number of GCs is relevant for accomplishing adequate control performance across a diverse set of control plants and bringing robustness to the cerebellar model against changes in its initialization parameters (i.e., synaptic weights and synaptic connections). We also show that not all the GCs are required to govern each control plant. What is more, the minimum number of GCs required to maintain adequate

control increases with the complexity of the control object (i.e., DoFs). Discussion about the relation between the number of GCs, motor performance attained, complexity of the control object, and robustness is presented.

6.2 Experimental protocol

For the experiments presented in this chapter, the cerebellar model was configured with a bi-hemispheric structure (**Fig. 3.1D**). A control task was configured for the brushed DC motor, the two-wheel balancing robot, and the simulated quadcopter objects (**Fig. 3.2**) comprising at least 100 repetitions of the desired motion. In the case of the DC motor, the desired shaft position ($\phi_{ref}(t)$) is a sinusoidal motion at $f = 0.5$ Hz (i.e., $\phi_{ref}(t) = \pi \sin(2\pi 0.5t)$). The balancing robot is commanded to follow a sinusoidal wheel motion ($\phi_{ref}(t) = \pi \sin(2\pi 0.25t)$) while the body tilt angle remained constant (90 degree with respect to the horizontal plane, $\theta_{ref}(t) = 0$), whereas the desired motion for the quadcopter is a sinusoidal horizontal (X-plane) motion with amplitude 2 m (i.e., $x_{ref}(t) = 2 \sin(2\pi 0.2t)$). Amplitude and frequency of the desired motions were chosen to be between 80 and 90 % of the maximum values that can be controlled for each plant in our setup. The number of active GCs in each hemisphere of the cerebellar model was modified by knocking down the initial GC population (4000 GCs). Twelve sizes were considered i.e., 4, 10, 20, 40, 80, 200, 400, 800, 1,000, 1,600, 2,000, or 4,000 GCs. The numbers of GO (27), MFs (257), BC (267) and PC (1) in each hemisphere were kept constant. A scaling synaptic constant (1/number of knocked down GCs) was employed to compensate for the missing excitatory input to BC, GO, and PC. Since the attained motor performance might be affected by the initialization conditions of the cerebellar model such as the random values of the synaptic weights and the random synaptic connections, five different sets of random synaptic weights and five tables of random synaptic connections are created to conform a set of 25 permutations of initial conditions for the cerebellar. Each control task was repeated 25 times for a given number of knocked down GCs (i.e., $25 \times 12 = 300$ experiments per control object). The yielded motor performance was measured cycle-by-cycle as the root mean square error (RSE) of the desired and yielded motion.

6.3 Results

We divided the experimental results into two parts with the purpose of studying the consequences of the number of GCs in the cerebellar model during robot control. First, we show the behavioral consequences in terms of motor performance, and second, we show the

neural consequences at PC firing rates, PF-PC synaptic weights, and inputs to the GCs.

6.3.1 Behavioral consequences of the number of GCs

Fig. 6.1A shows the control performance of the DC motor in terms of the RSE of the shaft angular position ($\phi(t)$) with 4 and 4,000 GCs (blue, and red lines) in each hemisphere of the cerebellar model as two examples of the GC size. Average RSE of $\phi(t)$ (N=25) is shown in bold blue and red lines. The RSE of $\phi(t)$ shows that the cerebellar model with 4,000 GCs adapted and improved the motor performance (RSE value was reduced on average 0.07 rad, 33.2% of the initial error value 0.20 rad), meaning that the PC learned the adequate motor commands to move the shaft of the DC motor to follow the desired motion. On the contrary, using 4 GCs produced highly variable performance and small improvement. **Fig. 6.1B** summarizes the motor performance for the twelve sizes of GCs considered and for reference the performance when the cerebellar model was disabled (i.e., DC motor controlled only by the PD) is shown as “PD”. This figure shows the average RSE (lines) and the standard deviation (error bars) across 25 different initialization conditions of the cerebellar model at the beginning (cycles #5-15, shown in red) and the end (cycles #180-190, shown in black) of the experiment. These cycles are marked in **Fig. 6.1A** as “a” and “b”, respectively. This result demonstrates that control performance of a DC motor with 1 DoF is improved by using the cerebellar model in comparison with a PD controller alone. The best performance was produced with 1,000 GCs (average RSE of $\phi(t)$ was reduced to 0.11 rad, 41.5% of the initial error value 0.25 rad). Using less than 40 GCs resulted in notably irregular performance and little improvement (difference between initial and final average RSE was less than 0.007 rad). **Fig. 6.1B** also shows that increasing the number of GCs was accompanied by a reduction in the standard deviation of the RSE (e.g., with 80 and 1,000 GCs the standard deviation of RSE was 0.14 rad and 0.041 rad, respectively) caused by changing the initial conditions of the model. Therefore, increasing the number of GCs in the cerebellar model during control of a single DoF system improves performance and reduces the variability due to changes in the initialization conditions.

Fig. 6.1C shows a XY-plane constructed by plotting the yielded ($\phi(t)$) against the desired ($\phi_{ref}(t)$) shaft position rotated by 45 degrees (axis included for reference). Panels C1 to C3, which correspond to the cycles shown in **Fig. 6.1A** with equal labels, show the behavioral effects on the yielded shaft motion when 4 (blue lines) and 4,000 (red lines) GCs were used. 4 GCs resulted in trajectories that diverged from the ideal trajectory (**Fig. 6.1C** gray lines) both in the positive (clockwise) and in the negative (counterclockwise) rotation of the shaft (shown in **Fig. 6.1C**). On the contrary, the trajectories generated by using 4,000 GCs progressively improved, especially in the clockwise direction.

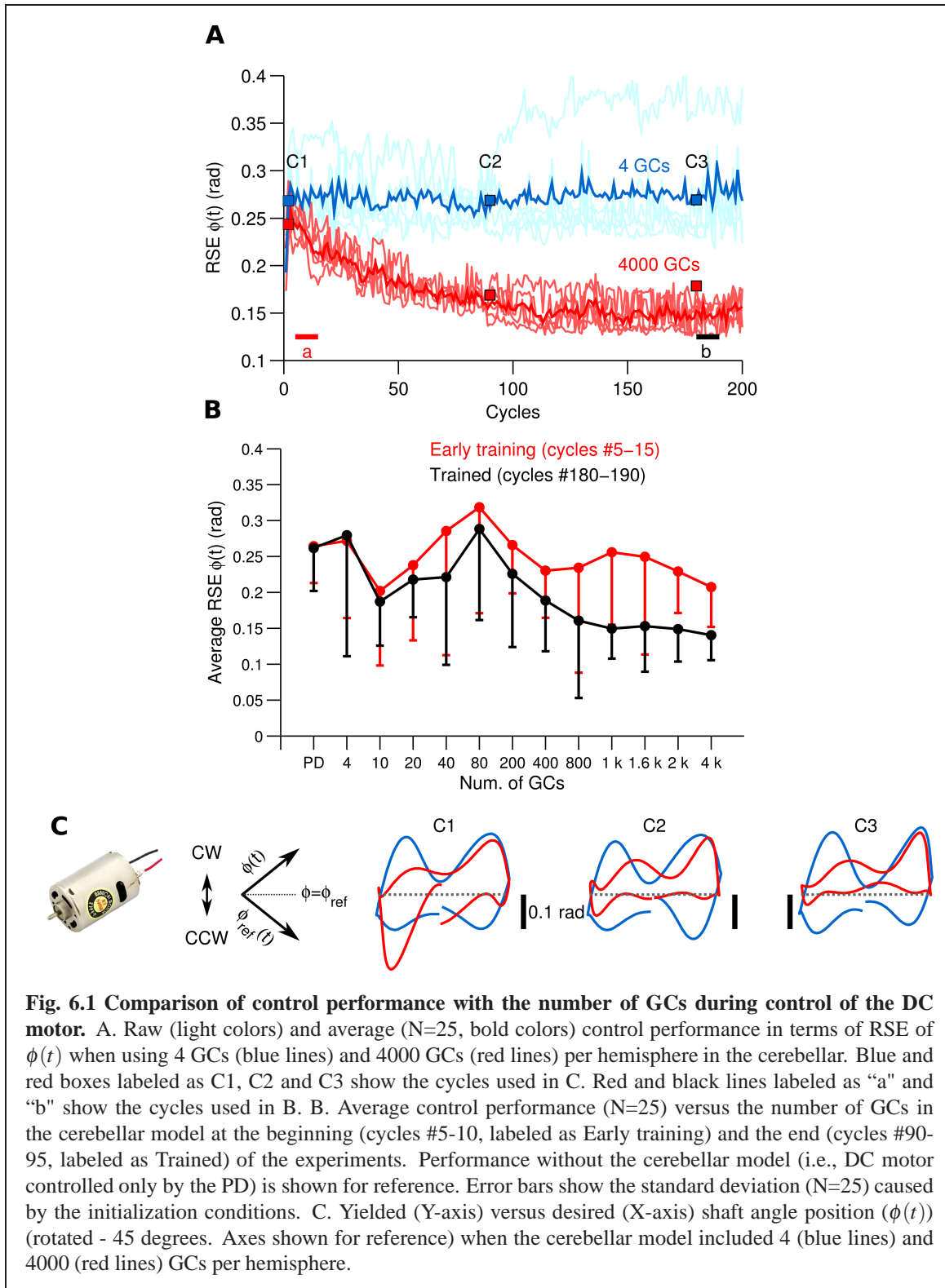
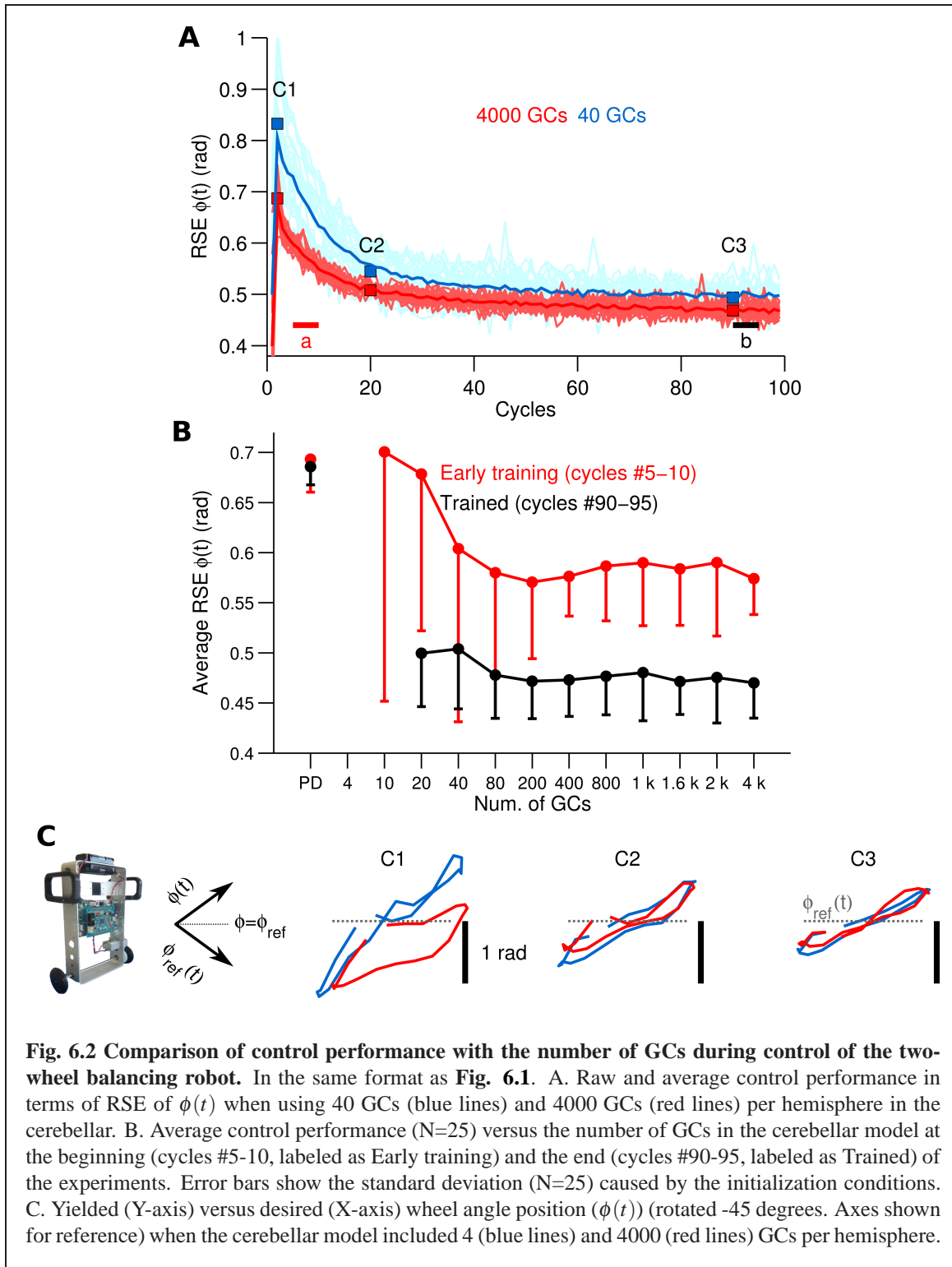


Fig. 6.1 Comparison of control performance with the number of GCs during control of the DC motor. A. Raw (light colors) and average ($N=25$, bold colors) control performance in terms of RSE of $\phi(t)$ when using 4 GCs (blue lines) and 4000 GCs (red lines) per hemisphere in the cerebellar. Blue and red boxes labeled as C1, C2 and C3 show the cycles used in C. Red and black lines labeled as "a" and "b" show the cycles used in B. B. Average control performance ($N=25$) versus the number of GCs in the cerebellar model at the beginning (cycles #5-10, labeled as Early training) and the end (cycles #90-95, labeled as Trained) of the experiments. Performance without the cerebellar model (i.e., DC motor controlled only by the PD) is shown for reference. Error bars show the standard deviation ($N=25$) caused by the initialization conditions. C. Yielded (Y-axis) versus desired (X-axis) shaft angle position ($\phi(t)$) (rotated - 45 degrees. Axes shown for reference) when the cerebellar model included 4 (blue lines) and 4000 (red lines) GCs per hemisphere.

The next experiment consisted in verifying the behavioral consequences observed in a simple 1 DoF system with a more challenging control plant. For this purpose, the cerebellar model is used for controlling a two-wheel balancing robot, which is a system with 2 DoFs. **Fig. 6.2A**, in the same format as **Fig. 6.1A**, shows the control performance attained in terms of RSE of wheel angular position ($\phi(t)$) with 40 and 4,000 GCs (blue, and red lines). In this control scenario, using 4 GCs and 10 GCs resulted in the robot falling in 15 out of 25 and 5 out of 25 repetitions, respectively. The control performances attained with 40 and 4,000 GCs look alike except for the lower variability of the RSE of $\phi(t)$ achieved with 4,000 GCs. This figure shows the adaptation capability of the cerebellar model and the improvement in motor performance during control of a system with 2 DoFs. Similar to the previous control scenario, these results evidence that the PCs learned the adequate motor commands to move the two-wheel balancing robot to follow the desired motion.

Fig. 6.2B, in the same format as **Fig. 6.1B**, summarizes the motor performance for the 12 sizes of GCs considered. It shows the average and the standard deviation (error bars) of the RSE of $\phi(t)$. This figure shows the improvement in motor performance by using the cerebellar model with 20 or more GCs. In average the RSE was reduced by 0.5 rad or 45.5% of the initial error value of 1.1 rad. Little improvement in average motor performance was achieved beyond a certain number of GCs (80 to 200 GCs, **Fig. 6.2B** black line). Nonetheless, increasing the number of GCs was accompanied by a reduction in the standard deviation of the RSE (error bars), especially during the early training (red lines). The cerebellar model with more than 20 GCs always outperformed the PD (shown as “PD” in **Fig. 6.2B**). **Fig. 6.2C** in the same format as **Fig. 6.1C**, presents the yielded wheel ($\phi(t)$) motions when 40 (blue lines) and 4,000 (red lines) GCs were used. Panel C1 shows that the wheel position trajectories during the beginning cycles were different for 40 and 4,000 GCs. With 4,000 GCs, the yielded wheel position presented relatively large deviation towards negative values, which corresponds to the backward motion of the two-wheel balancing robot. We have studied the asymmetry between forward and backward motion in the two-wheel balancing robot in our previous work¹²³ to produce asymmetrical adaptation in the cerebellar model as in the real cerebellum. However, the cerebellar model evolved and the two-wheel balancing robot gradually approached to the ideal trajectory (gray line) disregarding the number of GCs (panel C3).

Thus far we have shown the behavioral consequences of the number of GCs in the cerebellar during control of a 1 DoF and a 2 DoFs real world systems. Next we evaluate the behavioral consequences in a simulated model with 6 DoFs. **Fig. 6.3A**, in the same format as **Fig. 6.1A**, shows the control performance in terms of RSE of $x(t)$ when 200 and 4,000 GCs (blue, and red lines, respectively) during control of the simulated quadcopter. In this



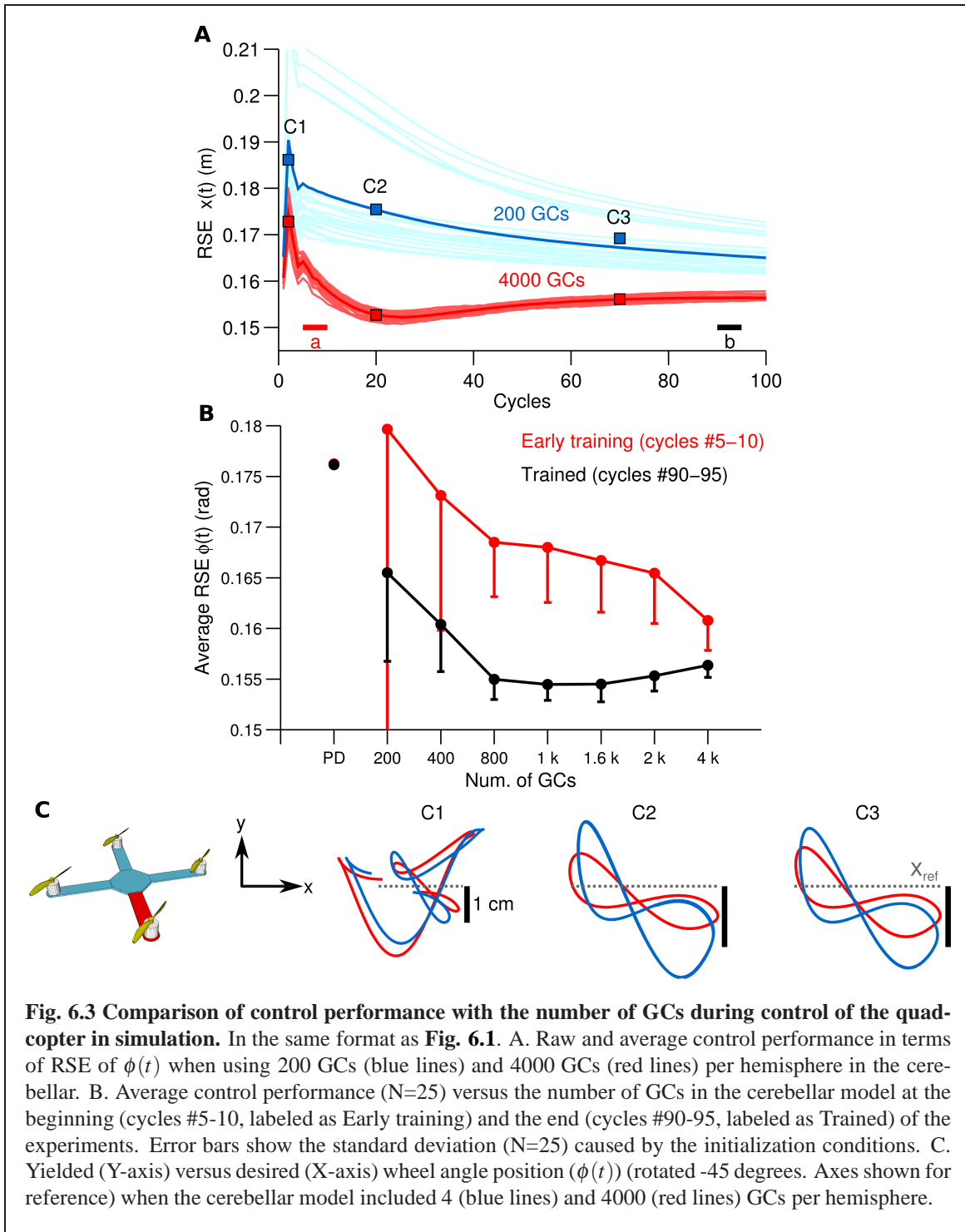


Fig. 6.3 Comparison of control performance with the number of GCs during control of the quadcopter in simulation. In the same format as **Fig. 6.1**. A. Raw and average control performance in terms of RSE of $\phi(t)$ when using 200 GCs (blue lines) and 4000 GCs (red lines) per hemisphere in the cerebellar. B. Average control performance ($N=25$) versus the number of GCs in the cerebellar model at the beginning (cycles #5–10, labeled as Early training) and the end (cycles #90–95, labeled as Trained) of the experiments. Error bars show the standard deviation ($N=25$) caused by the initialization conditions. C. Yielded (Y-axis) versus desired (X-axis) wheel angle position ($\phi(t)$) (rotated -45 degrees. Axes shown for reference) when the cerebellar model included 4 (blue lines) and 4000 (red lines) GCs per hemisphere.

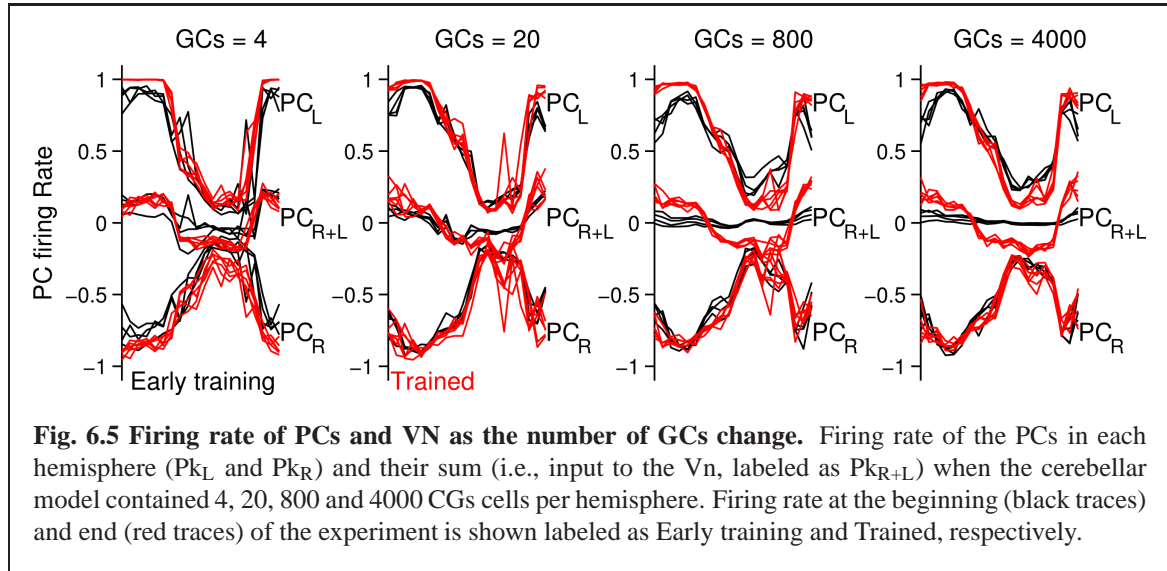
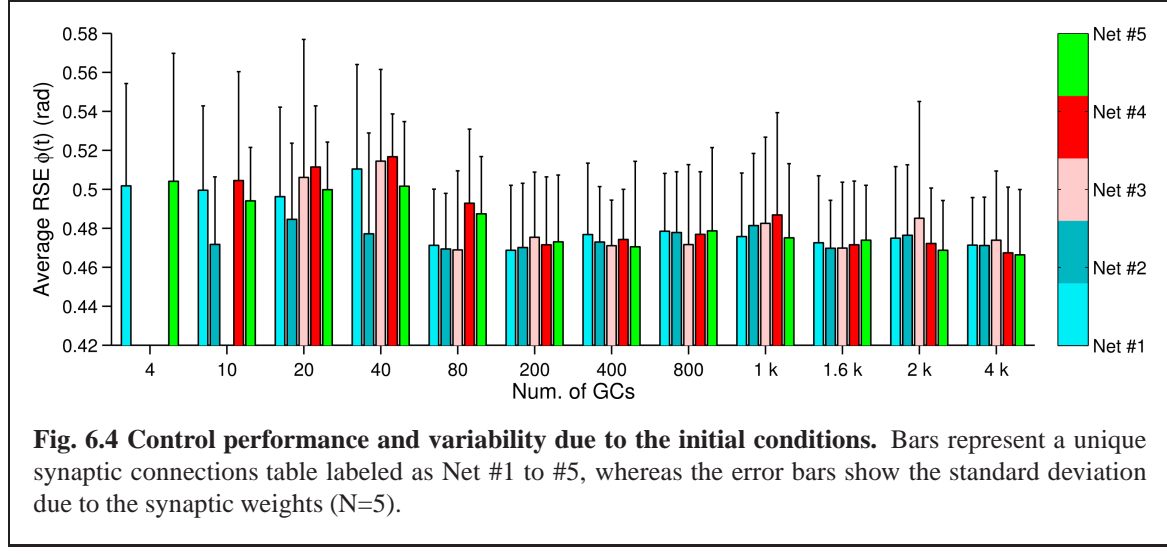
control scenario, using less than 200 GCs resulted in convergence errors happening during the simulation. Similar to the control scenarios in real world, the cerebellar model increased the control performance (average improvement of 0.02 m, 15% of the initial value 0.2 m)

and reduced the variability (i.e., standard deviation of RSE of $x(t)$) in the yielded motion of the 6 DoFs system. **Fig. 6.3B**, in the same format as **Fig. 6.1B**, summarizes the motor performance for the 12 sizes of GCs considered. The cerebellar model with 200 GCs or more outperformed the control performance achieved by using only the PD controller. **Fig. 6.3C** shows the XY-plane in which the quadcopter hovers. The desired trajectory is shown in gray and the yielded motion with 200 (blue lines) and 4,000 (red lines) GCs are shown. This result shows that increasing the number of GCs was accompanied by limited displacement in the y-axis (panel C1 in comparison with panel C3) away from the ideal trajectory (**Fig. 6.3C** gray lines). Therefore, in this simulated system with 6 DoFs larger numbers of GCs in the cerebellar model increase the control performance and reduce variability caused by the initial conditions as in the real world control objects tested above.

We have shown in **Fig. 6.1B**, and **Fig. 6.2B** (error bars) that the motor performance is affected by the number of GCs and also by the initial conditions. The initial conditions cause large variations in the control performance when using small numbers of GCs (< 1000 GCs). There are two initial conditions in the cerebellar model responsible for this variation, namely, synaptic weights and synaptic connections. Here, we evaluate the contribution of each initial condition to the overall variability in motor performance during control of the two-wheel balancing robot (variability with the DC motor and the quadcopter showed similar results). The 300 experiments were separated into 5 groups (referred to as Net #1-5) of 60 experiments each. The 60 experiments belonging to a given group share the same synaptic connections but differ in the number of GCs and set of random initial synaptic weights (12×5 sets of synaptic weights = 60, 60×5 Nets = 300 experiments). **Fig. 6.4** shows the average (bars) and standard deviation (error bars) of the RSE of $\phi(t)$ for each Net and number of GCs. This figure shows that three (Net #2, 3, and 4) out of five groups with 4 GCs failed to control the two-wheel balancing robot. Similarly, with 10 GCs Net #3 failed to control the robot. **Fig. 6.4** shows that increasing the number of GCs reduced the variability caused by changing the synaptic connections (average RSE, i.e., difference between bars height) and to a lesser degree the variability caused by the initial synaptic weights (standard deviation of RSE: error bars). Therefore, the synaptic connections produced the major part of the variability of the control performance with small numbers of GCs (< 800). When the cerebellar model included more than 1,000 GCs disregarding of the control object, the variability due to both initial conditions was compensated.

6.3.2 Neural consequences of the number of GCs

Up to now we have investigated the behavioral consequences of the number of GCs in the cerebellar model. In this section we evaluate the neural consequences, namely, PC firing



rates, PF-PC synaptic weights, and the MF and GO inputs to GCs. The particular results for the two-wheel balancing robot are shown here. Results with the DC motor and quadcopter followed similar trends to those of the two-wheel balancing robot. First, we studied the effects in the firing rate of the PCs. **Fig. 6.5** shows the firing rate of the PCs in the left (Pk_L) and right (Pk_R) hemisphere, and their sum (Pk_{R+L}), which corresponds to the cerebellar input to the Vn with 4, 20, 800 and 4,000 GCs. For the sake of comparison this figure presents five cycles aligned and superimposed at the beginning (same cycles shown in **Fig. 6.1A** as “a”, here labeled as Early training) and the end (same cycles shown in **Fig. 6.1A** as “b”, labeled as Trained) of the experiment. Comparison of the firing rates evidences a

change in the cerebellar input to the Vn (i.e., Pk_{R+L}) caused by the number of GCs. When fewer (< 80) GCs were used, the default firing rates of Pk_L and Pk_R at the beginning of the experiment did not cancel each other (**Fig. 6.5**, 4 and 20 GCs black lines labeled as Pk_{R+L}), contrary to the case when more than 200 GCs were used. This means that the cerebellar input to the Vn was carrying a default modulation in its firing rate with less than 200 GCs. Such a modulation was not learned and probably unrelated to the control task. On the contrary, with more than 200 GCs, Pk_{R+L} did not present any modulation, meaning that the cerebellar input to the Vn was neutral to the control task. The default information in Pk_{R+L} (**Fig. 6.5** red traces) endured to the last cycles of the experiments. With 4 or 20 GCs the evolved Pk_{R+L} presented similar shape as the firing rate in the early training (i.e., a bias information). With 800 or 4,000 the evolved Pk_{R+L} corresponded to the motor command required during the control of the two-wheel balancing robot.

Next we evaluate the PF-PC synapses, which are the soles plastic loci in the current configuration of the cerebellar model. To observe additional neural changes the desired wheel motion (see Sec. 2.3 for more details about the experimental protocol) was changed at cycle #50 to a more difficult motion corresponding to a sum of sines ($\phi_{ref}(t) = \pi \sin(2\pi 0.2t) + \sin(2\pi 0.7t)$, $\theta_{ref}(t) = 0$) and leave it for 50 more cycles. The sum of sines is a much more difficult motion for the robot. In fact, disabling the cerebellar model output (i.e., robot controlled only by the PD) completely abolished the control of the robot. We analyze the synaptic weights between GCs and PC (\mathbf{W}_{PF-PC}) in search of extra insights into the role of the GCs (**Fig. 6.5A** with 1,000 GCs in the right hemisphere; other GCs and left hemisphere presented similar behavior). During the first 50 cycles corresponding to the single sinusoidal task, the PC-PF synapses diverged from the initial value by action of LTD (48.6 % of GCs) and LTP (51.4 % of GCs). Those GCs that carried relevant information to reduce the error signal in the cf input had their synaptic weight presumably increased, whereas those not relevant to reduce the error had their weight unchanged or decreased. Interestingly, at cycle #50 when the desired motion was changed, some GCs that had their synaptic weight decreased started to be potentiated (10.3 %) and others further depressed (in total 75.1 %). Similarly, some of the GCs that presented large synaptic weights had their weights decreased (34.0 %) or more potentiated (in total 24.9 %). To discard the effect of the random initial synaptic weight in this result, **Fig. 6.5D** shows the five different initial synaptic weights belonging to three representative GCs sharing the same synaptic connectivity (i.e., same Net). This figure demonstrates that despite the random initial values the global behavior of the synaptic weights follows a similar trend.

Next we investigated the MF and GO inputs to the GCs that had their \mathbf{W}_{PF-PC} synaptic weight preferably potentiated (referred here as “best GCs”) during control of the two-wheel

balancing robot because those GCs are presumably best suitable for the control task. Once the best GCs were identified based on their evolved $\mathbf{W}_{\text{PF-PC}}$ synaptic weight, we analyzed their patterns of MF inputs and asked if those patterns are exclusively presented in the best GCs. Such a relationship would indicate that a particular pattern of MF inputs is well suited for the control task. The GCs were sorted from largest to smallest $\mathbf{W}_{\text{PF-PC}}$ synaptic value at cycle #50. Each GC makes synapses with the four closest MFs in the 3D cube of cerebellar cortex in the cerebellar model (see Material and Methods for details about the network construction), and thus, each GC has a random combination of MFs inputs. **Fig. 6.6B** shows the four MF inputs of the 14 best GCs (i.e., 14 largest $\mathbf{W}_{\text{PF-PC}}$) found, and the seven different types of MFs derived from the two-wheel balancing robot coded by colors. The color matrix suggests that each of the 14 best GCs have a unique pattern of MF inputs. For instance, the GC with the 4th largest $\mathbf{W}_{\text{PF-PC}}$ receives MF inputs carrying desired wheel angle (dark blue, $\phi_r(t)$), wheel angle error (yellow, $\phi_e(t)$), and two MFs carrying efference copy (dark red, EC(t)). However, this pattern of MF inputs is not unique to the 4th best GC. **Fig. 6.6A** shows in red the $\mathbf{W}_{\text{PF-PC}}$ of all the GCs (13 out of 1,000) that share the same pattern of MF inputs as the 4th best GC. It can be observed that some GCs were depressed and others were potentiated during the initial 50 cycles of the experiment. Therefore, the MFs inputs are not the only discriminant characteristic of those GCs preferably potentiated. The only option remaining to determine the convergent value of $\mathbf{W}_{\text{PF-PC}}$ is the GO inputs to the GCs. Each GC receives four GO inputs connected in the same fashion as the MF inputs (i.e., the fourth closest GOs). **Fig. 6.6C** shows the four GO inputs (out of 27 available) for each of the GCs that share the same MF inputs as the best 4th GC. The order of the GCs follows the numeration shown in red in **Fig. 6.6A**. This figure shows that each of the 13 GCs sharing the same MFs has different GO inputs, and therefore, each GCs is processing a unique combination of inputs that yielded the different $\mathbf{W}_{\text{PF-PC}}$ values based upon the relevance of each GCs to the control task.

6.4 Discussion

GCs are small, densely packed, and have a unique morphology with four dendrites and an axon that bifurcates in two parallel fibers. This is a set of remarkable features that suggest GCs have a high input sensibility required for processing incoming information^{1;6;26;103;107}. There has been a popular theory proposing that GCs transform the incoming information into a higher dimensional, sparse representation^{69;103;131}, which allows the downstream cerebellar circuits to perform associative learning^{1;26;103;107;140}, adaptive filtering^{31;42}, and binary addressing⁷⁵. Furthermore, the limited number of input synaptic connections (i.e.,

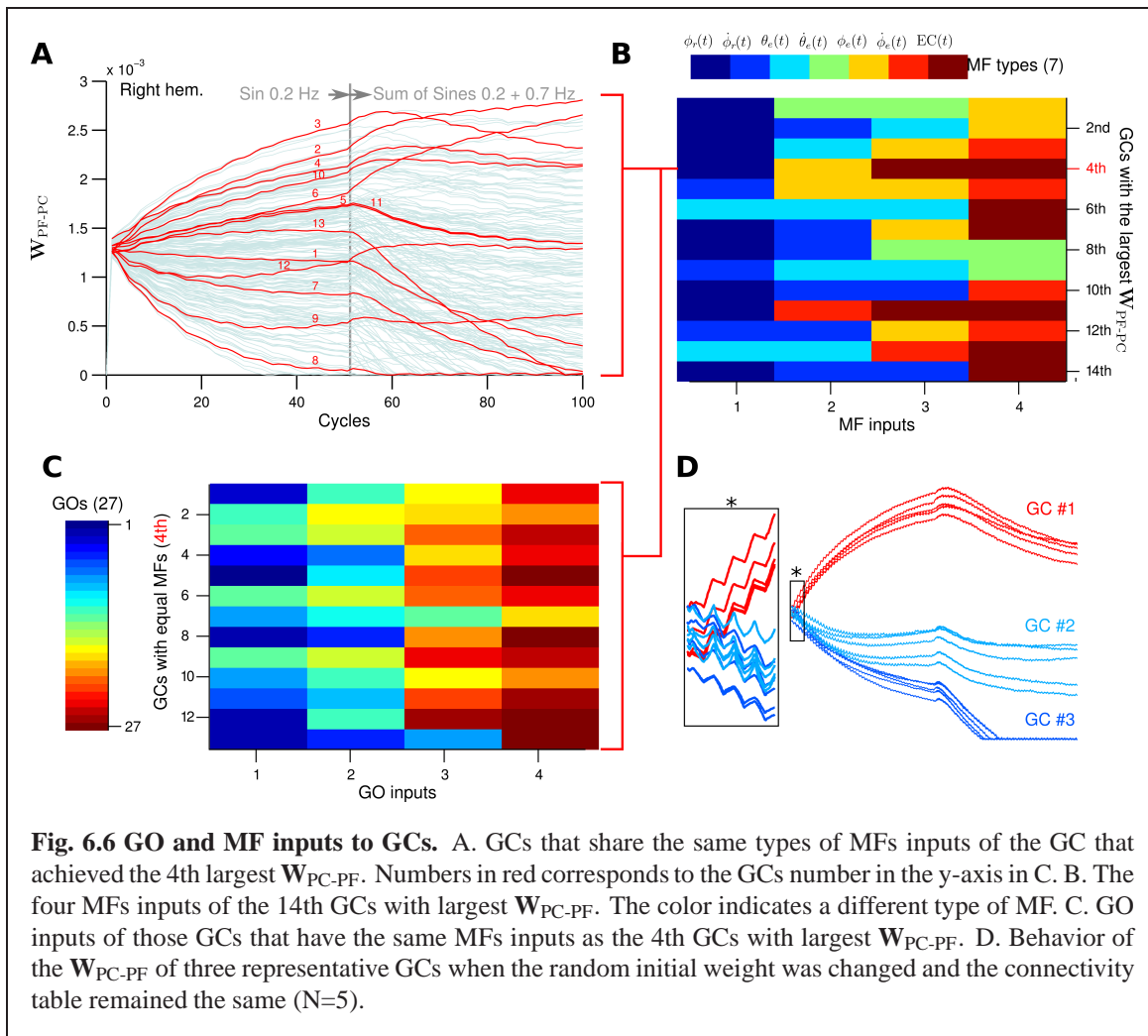


Fig. 6.6 GO and MF inputs to GCs. A. GCs that share the same types of MFs inputs of the GC that achieved the 4th largest W_{PC-PF} . Numbers in red corresponds to the GCs number in the y-axis in C. B. The four MFs inputs of the 14th GCs with largest W_{PC-PF} . The color indicates a different type of MF. C. GO inputs of those GCs that have the same MFs inputs as the 4th GCs with largest W_{PC-PF} . D. Behavior of the W_{PC-PF} of three representative GCs when the random initial weight was changed and the connectivity table remained the same ($N=5$).

four dendrites) allows optimal lossless space encoding⁶. A consequence that follows is that not all the GCs are required for a particular motor task, since only a fraction of the population is active at any time (i.e., sparse representation). Computational and experimental evidence have confirmed this premise. Schweighofer's model that implements unsupervised learning of GCs sparse coding showed that basic motor performance can be normal despite a small number of GCs¹⁴⁰. Likewise, behavioral experiments with mutant mice with impaired GC output showed that motor performance during different motor tasks was intact⁴³. In line with this evidence, the results of our behavioral experiments with both real world and simulated control objects showed that only a fraction of the GCs population is required for performing successfully a specific control task (DC motor, 10 GCs Fig. 6.1A; two-wheel balancing robot, 40 GCs Fig. 6.2A; quadcopter, 200 GCs Fig. 6.3A). Our experiments further showed that increasing the number of GCs reduces the variability in the results caused

by changing the initialization synaptic weights and the synaptic connections (**Fig. 6.4**). This suggests that the abundant number of GCs brings robustness to the cerebellar circuit in two ways; first, a large number of GCs mean that a vast repertoire of input patterns and output control objects can be adequately coordinated, and second, in the case of a structural reconfiguration (e.g., injuries, aging) the integrity of the cerebellar circuit and its functions can be preserved. From an engineering point of view, using a large number of GCs bring flexibility and robustness to the cerebellar model because control objects with different dynamics can be adequately controlled. In addition, if the control task is fixed, the number of GCs can be reduced to find a compromise between the control performance and the energy/hardware requirements of the cerebellar.

Our results are also in line with the prediction that the loop conformed by the feedback and feedforward pathways between GC–GO, and MFs–GO–GC, respectively, supporting the sparsification of the incoming information at the GCs¹³¹. We found that the pattern of MF inputs of the GCs preferably potentiated during the control tasks did not provide enough features to discriminate the GCs. However, when we included in the classification the patterns of GO inputs to those GCs it was possible to identify unequivocally each GC. Therefore, the role carried out by the GCs is accentuated by the inhibition from GO in our cerebellar as in the real cerebellum.

7

Discussion and Future research

The overall aim of the studies described in this thesis is the development of computational methods inspired by the brain and their incorporation into engineering applications. In turn, by developing and using such methods, we can also deepen our understanding about the brain itself. More specifically, we investigated whether a novel wavelet-based computational method for analyzing the neural activity acquired from microelectrodes (MER) during implantation of the deep brain stimulator (DBS) as treatment for Parkinson disease can be used to automatically identify the nuclei in the basal ganglia (BG). Whether a realistic computational model of the cerebellar cortex provides adaptive control to a variety of control objects; and whether hypothesis for three unresolved questions about the neural mechanism of function in the cerebellum are brought forward by using the cerebellar model during engineering applications.

Inspiration from the brain to solve engineering applications

In **Chapter 2**, we presented a novel computational method for analysis of neural activity from the BG to support the localization of the DBS during the treatment of Parkinson's disease. Traditionally the localization of the nucleus target in the BG relies on stereotactic coordinates generated before the surgery by image planning softwares that use brain scans and

generic anatomic atlas to reconstruct approximate models of the patient's head. These coordinates guide the neurosurgeon to an approximately location inside the brain during surgery, however, due to the limited resolution of the images, brain movements, tissue compression, and stereotactic frame's accuracy extra aids are used to secure the adequate location of the DBS. Auditive and visual confirmation of the neural activity of the BG is commonly used as a confirmation tool despite being highly subjective. In this context, an automatic system for identification of the BG responds to the needs of objectivity, determinism, and accuracy desired as a support tool to the neurosurgeon during DBS procedures. We showed that by creating new wavelet functions based on the neural information within the microelectrodes recording (MER) signals acquired from the BG, it was possible to identify four nuclei in the BG with high accuracy ($> 90\%$), outperforming the results obtained with regular wavelet analysis that does not take into account the nature of the MER signals⁴⁷. The success in this method relies in the distinctiveness of the neural data coming from each of the BG. The new wavelet function exploits this fact and provides the objective version of what the auditive and visual examination of the MER signals yield. These results evidence that by taking into account the particularities in the brain, the engineering application under consideration, i.e., the automatic location of the DBS in the BG, can be improved^{121;126}. Although this is not the first attempt to produce such a computational method^{88;154;164;170}, the method presented here is the first one to take the MER signal itself to create the wavelet functions, that is, the first method to take inspiration in the BG neural activity itself to solve the BG localization problem.

Similarly, **Chapter 3** presented a neuronal network model inspired by the cerebellum to accomplish adaptive robot control. We tested the model during control of two real world and one simulated plants to demonstrate that disregarding the complexity of the control object (i.e., the number of DoF) the cerebellar model provides an adaptive contribution to classical feedback loops. We showed that by using the cerebellar model, the control performance achieved was higher than that obtained by using only classical non-adaptive controllers. The cerebellar model developed here is compatible with the Marr-Albus-Ito theory of motor learning and with other models regarding the anatomical description of the cerebellar cortex¹⁴³. It employs a 3D approach for construction of the network connections following biological densities of neurons^{27;143}, and includes a biologically plausible learning rule⁶⁷. This is important because by incorporating the concepts of the Marr-Albus-Ito theory, and the spatial features of the cerebellar cortex our model is in-line with the evidence supporting the classical (i.e., the motor learning theory) view and the new findings regarding the information processing in the granular layer¹⁴³. Different from other models proposed thus far, our model includes a bi-hemispheric structure, inhibitory connections from BA to GO,

and mutual inhibitory synapses between BA and PC, which have been characterized electrophysiologically^{34;97;112}. The feedback connection between BA and GO is remarkable for being vastly obliterated in the current literature and because it could have striking consequences in the cerebellar circuit. A recurrent connection such as the BA-GO feedback pathway might provide strong modulation of GC activity, memory storage, and integration functions¹³¹. This connection calls for further study and characterization. We have also shown that our cerebellar model is suitable for implementations using real time, stand alone devices¹²⁵ (**Appendix B**). In contrast to spiking neuron models of the cerebellum^{46;63;168}, due to the level of abstraction in our model (i.e., firing rate neuron models), spike patterns and temporal or spatial effects were not possible to evaluate. This would require the construction of a cerebellar network with spiking neuronal models that could endanger the real-time real-world application in control engineering. Finally, our cerebellar model includes plasticity at synapses between GCs and PCs. However, other sites of plasticity in the cerebellum and their involvement in motor learning have been argued^{45;46;105}, such as the synapses between BA and PCs driven by the CF and MFs and GCs. Our results evidence that by constructing a model inspired by the brain, we can solve engineering applications such as adaptive robot control.

Engineering applications to understand the brain

Chapter 4, 5, and 6 enclose the second part of the philosophy of this thesis. That is, by using the computational model inspired by the cerebellum to solve real world engineering applications such as adaptive robot control, we could also foster our understanding of the cerebellum. The engineering applications and the cerebellar model provide us with a unique testbed for attempting to conciliate three questions about this brain area regarding the type of error content in the CF, the mechanisms of cerebellar asymmetrical learning, and the role of the abundant number of GCs. Firstly, two types of error have been greatly defended: SE and ME^{31;70;86;152}. Our experimental results in **Chapter 4** showed that both SE and ME despite producing unique behavioral and neural changes in the cerebellar model, specially at the PC, are adequate error signals to drive the plasticity in our model and govern successfully the plants in a diversity of control tasks. This is the first direct demonstration that both SE and ME can be an adequate error signal to teach the cerebellar model in real world engineering applications.

Secondly, asymmetrical cerebellar learning has been repeatedly demonstrated, yet its understanding is limited. Lesioning of the cerebellar hemispheres compromises both the ipsilateral and contralateral motor learning^{22;113}. The results presented in **Chapter 5** show that the cerebellar model with a bi-hemispheric structure can produce a form of cerebellar

asymmetrical adaptation, in contrast to the model with uni-hemispheric structure. During the control experiments with the two-wheel balancing robot, the performance was affected not only when the asymmetrical perturbation was added to the ipsidirectional side of the robot but also (albeit in a lesser degree) when the perturbations were located on the contradirectional side of the robot. Furthermore, the results of the present model suggest a mechanism that explains the interaction observed between the cerebellar hemispheres. This mechanism involves the CF input, which drove the plasticity at PF-PC synapses in each hemisphere. This input increased its firing rate above its spontaneous firing rate with ipsidirectional erroneous motions, whereas it reduced its firing rate with contradirectional erroneous motions. This configuration of CF input has been suggested in monkey experiments, where complex spike activity of PCs is highly correlated with CF activity^{58;59}. Our results reinforce the relevance of this configuration of the CF input. The CF worked as a differential link that balanced the contribution of each hemisphere to the overall input to the VN.

Lastly, **Chapter 6** investigated the role of the abundant GCs. There has been a popular theory proposing that GCs transform the incoming information into a higher dimensional, sparse representation^{69;103;131}, which allows the downstream cerebellar circuits to perform associative learning^{1;26;103;107;140}, adaptive filtering^{31;42}, and binary addressing⁷⁵. Computational and experimental evidence have confirmed this premise. Schweighofer's model that implements unsupervised learning of GCs sparse coding showed that basic motor performance can be normal despite a small number of GCs¹⁴⁰. Likewise, behavioral experiments with mutant mice with impaired GC output showed that motor performance during different motor tasks was intact⁴³. In line with this evidence, the results of our behavioral experiments with both real world and simulated control objects showed that only a fraction of the GCs population is required for performing a specific control task successfully. Our experiments further showed that increasing the number of GCs reduces the variability in the results caused by changing the initialization of synaptic weights and the synaptic connections. This suggests that the abundant number of GCs brings robustness to the cerebellar circuit in two ways; first, a large number of GCs mean that a vast repertoire of input patterns and output control objects can be adequately coordinated, and second, in the case of a structural reconfiguration (e.g., injuries, aging) the integrity of the cerebellar circuit and its functions can be preserved.

These results in overall demonstrate that by approaching engineering applications with computational models inspired by the brain, not only the solution to the application is achieved but also questions regarding the brain function can be investigated. This is particularly adequate in the case of motor control and robotics, since the brain and the controller

share common objectives, that is, smooth, low jerk, and adaptive control of movements.

Future research

Reflecting on the results presented in this thesis, I realized that there are more open doors and unknowns now than at the beginning of the thesis. We have shed some light into three questions regarding the cerebellum including the nature of the error in the CF, the mechanisms of asymmetrical adaptation, and the role of the abundant number of GCs, however, experimental evidence to prove or refute these hypotheses of function are required. Some of the experimental conditions required to test these hypotheses are already available and have been explored in the literature such as ipsilateral cerebellar ablation to test asymmetrical cerebellar learning^{113;155}. Other conditions required new techniques and protocols, for instance, to test the nature of the CF error content. An open question that remains latent is the role of the recurrent connection produced by the inhibitory projection of BA to GO. Although this inhibition is not unique to the GO because LU also inhibit GO^{33;34}, the inputs of BA are well known and better characterized than those of the LU. Nonetheless, both connections have the potential of modulating the activity of GCs, providing memory, and integrating information. These are rich computational qualities that have been shown to be critical in recurrent neural networks.

The BG and the cerebellum share disynaptic connections¹¹, yet thus far little has been known to develop a unified computational model of both structures. This is an interesting topic because the cerebellum works under supervised associative learning whereas the BG follows unsupervised reinforcement learning. The prospect of a model enclosing both types of learning is indeed alluring for the engineering applications that could be enriched by such a learning scheme, and also for the implications for the research about motor dysfunctions such as Parkinson' disease and tremor.

In **Chapter 2**, I presented an evolutive optimization procedure to create new wavelet functions from the neural activity of the BG. These procedure general in the sense that it could be used to create wavelets from other types of signals. In fact, we have demonstrated this case in EEG signals for classification of epileptic seizures¹²⁷, EMG signals for classification of hand movements, and Pupil fluctuation signals for detection of driver drowsiness¹²⁸. It remains a future improvement of this procedure to include cultural algorithm in the optimization, to construct sparse representations of the input signal with optimal dictionaries that could learned during the evolutive optimization¹¹⁴, to select the best basis of decomposition based on the wavelet packet transform, and to validate with other types of signals.

I envision that computational models that integrate the neural circuits of the BG and cerebellum will be developed in the near future and their extrapolation into engineering application will be explored. I foresee that the role of the non-classical interneurons in the molecular layer (i.e., the LU) will be reevaluated and assimilated into the mainstream cerebellar research. Finally, I anticipate that leaps towards artificial intelligence and every day robotics will be enriched by the computational models of the BG and cerebellum for motor control and coordination.

References

- [1] Albus, J. S. (1971). A theory of cerebellar function. *Mathematical Biosciences*, 10(1–2):25 – 61.
- [2] Albus, J. S. (1975). A new approach to manipulator control: the cerebellar model articulation controller (cmac). *Journal of Dynamic Systems, Measurement, and Control*, 97:220–227.
- [3] Anzai, M., Kitazawa, H., and Nagao, S. (2010). Effects of reversible pharmacological shutdown of cerebellar flocculus on the memory of long-term horizontal vestibulo-ocular reflex adaptation in monkeys. *Neuroscience Research*, 68(3):191 – 198.
- [4] Bartels, A. L. and Leenders, K. L. (2009). Parkinson’s disease: The syndrome, the pathogenesis and pathophysiology. *Cortex*, 45(8):915–921.
- [5] Belknap, D. and Noda, H. (1987). Eye movements evoked by microstimulation in the flocculus of the alert macaque. *Experimental Brain Research*, 67(2):352–362.
- [6] Billings, G., Piasini, E., Lőrincz, A., Nusser, Z., and Silver, R. (2014). Network structure within the cerebellar input layer enables lossless sparse encoding. *Neuron*, 83:1–15.
- [7] Blazquez, P., Partsalis, A., Gerrits, N. M., and Highstein, S. M. (2000). Input of anterior and posterior semicircular canal interneurons encoding head-velocity to the dorsal y group of the vestibular nuclei. *Journal of Neurophysiology*, 83(5):2891–2904.
- [8] Blazquez, P. M., Hirata, Y., Heiney, S. A., Green, A. M., and Highstein, S. M. (2003). Cerebellar signatures of vestibulo-ocular reflex motor learning. *The Journal of Neuroscience*, 23(30):9742–9751.
- [9] Blazquez, P. M., Hirata, Y., and Highstein, S. M. (2006). Chronic changes in inputs to dorsal y neurons accompany VOR motor learning. *Journal of Neurophysiology*, 95(3):1812–1825.
- [10] Bobo, L., Herreros, I., and Verschure, Paul, F. (2012). A digital neuromorphic implementation of cerebellar associative learning. In *Biomimetic and Biohybrid Systems*, volume 7375 of *Lecture Notes in Computer Science*, pages 13–25. Springer Berlin Heidelberg.
- [11] Bostan, A. and Strick, P. (2010). The cerebellum and basal ganglia are interconnected. *Neuropsychology Review*, 20(3):261–270.
- [12] Bostan, A. C., Dum, R. P., and Strick, P. L. (2010). The basal ganglia communicate with the cerebellum. *Proceedings of the National Academy of Sciences*, 107(18):8452–8456.
- [13] Bostan, A. C., Dum, R. P., and Strick, P. L. (2013). Cerebellar networks with the cerebral cortex and basal ganglia. *Proceedings of the National Academy of Sciences*, 110(5):241–254.

- [14] Brette, R., Rudolph, M., Carnevale, T., Hines, M., Beeman, D., Bower, J. M., Diesmann, M., Morrison, A., Goodman, P. H., Harris, Frederick C., J., Zirpe, M., Natschläger, T., Pecevski, D., Ermentrout, B., Djurfeldt, M., Lansner, A., Rochel, O., Vieuille, T., Muller, E., Davison, A. P., El Boustani, S., and Destexhe, A. (2007). Simulation of networks of spiking neurons: A review of tools and strategies. *Journal of Computational Neuroscience*, 23(3):349–398.
- [15] Broussard, D. M. and Kassardjian, C. D. (2004). Learning in a simple motor system. *Learning and Memory*, 11(2):127–136.
- [16] Cantalupo, C., Freeman, H., Rodes, W., and Hopkins, W. (2008). Handedness for tool use correlates with cerebellar asymmetries in chimpanzees (*pan troglodytes*). *Behavioral Neuroscience*, 122(1):191–19.
- [17] Capobianco-Guido, R., Barbon, S., Sasso-Vieira, L., Lopes-Sanchez, F., Dias-Macié, C., J.C.Pereira, Scalassara, P., and Silva-Fonseca, E. (2008). Introduction to the discrete shapelet transform and a new paradigm: Joint time-frequency-shape analysis. In *IEEE International Symposium on Circuits and Systems, 2008. ISCAS 2008.*, pages 2893–2896.
- [18] Carrillo, R. R., Ros, E., Boucheny, C., and Coenen, O. J.-M. (2008). A real-time spiking cerebellum model for learning robot control. *Biosystems*, 94(1–2):18 – 27.
- [19] Casellato, C., Pedrocchi, A., Garrido, J., Luque, N., Ferrigno, G., D’Angelo, E., and Ros, E. (2012). An integrated motor control loop of a human-like robotic arm: Feedforward, feedback and cerebellum-based learning. In *4th IEEE RAS EMBS International Conference on Biomedical Robotics and Biomechatronics (BioRob)*, pages 562–567.
- [20] Chan, H.-L., Wu, T., Lee, S.-T., Lin, M.-A., He, S.-M., Chao, P.-K., and Tsai, Y.-T. (2010). Unsupervised wavelet-based spike sorting with dynamic codebook searching and replenishment. *Neurocomputing*, 73(7-9):1513–1527.
- [21] Chiu, C.-H. (2010). The design and implementation of a wheeled inverted pendulum using an adaptive output recurrent cerebellar model articulation controller. *IEEE Transactions on Industrial Electronics*, 57(5):1814–1822.
- [22] Choi, K.-D., Kim, H.-J., Cho, B., and Kim, J. (2008). Saccadic adaptation in lateral medullary and cerebellar infarction. *Experimental Brain Research*, 188(3):475–482.
- [23] Coesmans, M., Weber, J. T., De Zeeuw, C. I., and Hansel, C. (2004). Bidirectional parallel fiber plasticity in the cerebellum under climbing fiber control. *Neuron*, 44(4):691–700.
- [24] Cozzens, J. W. (2007). Surgery for parkinson’s disease: Motor aspects of parkinson’s disease. *Disease-a-Month*, 53(4):227–242.
- [25] D’Angelo, E. (2011). Neural circuits of the cerebellum: hypothesis for function. *Journal of Integrative Neuroscience*, 10(03):317–352.
- [26] D’Angelo, E. and De Zeeuw, C. I. (2009). Timing and plasticity in the cerebellum: focus on the granular layer. *Trends in Neurosciences*, 32(1):30–40.
- [27] D’Angelo, E., Mazzarello, P., Prestori, F., Mapelli, J., Solinas, S., Lombardo, P., Cesana, E., Gandolfi, D., and Congi, L. (2011). The cerebellar network: From structure to function and dynamics. *Brain Research Reviews*, 66(1–2):5–15.
- [28] Davies, D. L. and Bouldin, D. W. (1979). A Cluster Separation Measure. *IEEE Transactions on Pattern Analysis and Machine Intelligence*, PAMI-1(2):224–227.

- [29] De Zeeuw, C. I., Koekkoek, S., van Alphen, A., Luo, C., Hoebeek, F., van der Steen, J., Frens, M., Sun, J., Goossens, H., Jaarsma, D., Coesmans, M., Schmolesky, M., De Jeu, M., and Galjart, N. (2004). Gain and phase control of compensatory eye movements by the flocculus of the vestibulocerebellum. In Highstein, S., Fay, R., and Popper, A., editors, *The Vestibular System*, volume 19 of *Springer Handbook of Auditory Research*, pages 375–422. Springer New York.
- [30] Dean, P., Anderson, S., Porrill, J., and Jörntell, H. (2013). An adaptive filter model of cerebellar zone c3 as a basis for safe limb control? *The Journal of Physiology*, 591(22):5459–5474.
- [31] Dean, P., Porrill, J., Ekerot, C.-F., and Jörntell, H. (2010). The cerebellar microcircuit as an adaptive filter: experimental and computational evidence. *Nat Rev Neurosci*, 11(1):30–43.
- [32] Demer, J. L. (1992). Mechanisms of human vertical visual-vestibular interaction. *Journal of Neurophysiology*, 68(6):2128–2146.
- [33] Dieudonné, S. and Dumoulin, A. (2000). Serotonin-driven long-range inhibitory connections in the cerebellar cortex. *The Journal of Neuroscience*, 20(5):1837–1848.
- [34] Dumoulin, A., Triller, A., and Dieudonne, S. (2001). Ipse kinetics at identified gabaergic and mixed gabaergic and glycinergic synapses onto cerebellar golgi cells. *The Journal of Neuroscience*, 21(16):6045–6057.
- [35] Eccles, J. C. and Ito Masao, a. S. J. (1967). *The cerebellum as a neuronal machine*. Springer-Verlag.
- [36] Edwin, C. and C D, O. (1968). *The human brain and spinal cord; a historical study illustrated by writings from antiquity to the twentieth century*. University of California Press.
- [37] Eliasmith, C. and Trujillo, O. (2014). The use and abuse of large-scale brain models. *Current Opinion in Neurobiology*, 25:1–6.
- [38] Erkelens, C. J., Collewijn, H., and Steinman, R. M. (1989). Asymmetrical adaptation of human saccades to anisotropic spectacles. *Investigative Ophthalmology and Visual Science*, 30(6):1132–1145.
- [39] Eskiizmirliiler, S., Forestier, N., Tondu, B., and Darlot, C. (2002). A model of the cerebellar pathways applied to the control of a single-joint robot arm actuated by mckibben artificial muscles. *Biological Cybernetics*, 86(5):379–394.
- [40] Floureens, P. (1858). *De la vie et de l'intelligence*. Garnier.
- [41] Frens, M. A., Mathoera, A. L., and van der Steen, J. (2001). Floccular complex spike response to transparent retinal slip. *Neuron*, 30(3):795 –801.
- [42] Fujita, M. (1982). Adaptive filter model of the cerebellum. *Biological Cybernetics*, 45(3):195–206.
- [43] Galliano, E., Gao, Z., Schonewille, M., Todorov, B., Simons, E., Pop, A. S., D'Angelo, E., van den Maagdenberg, A. M., Hoebeek, F. E., and De Zeeuw, C. I. (2013). Silencing the majority of cerebellar granule cells uncovers their essential role in motor learning and consolidation. *Cell Reports*, 3(4):1239–1251.
- [44] Galliano, E., Mazzarello, P., and D'Angelo, E. (2010). Discovery and rediscoveries of golgi cells. *The Journal of Physiology*, 588(19):3639–3655.

- [45] Gao, Z., Beugen, B. J. v., and De Zeeuw, C. I. (2012). Distributed synergistic plasticity and cerebellar learning. *Nature Reviews Neuroscience*, 13:619–635.
- [46] Garrido Alcazar, J. A., Luque, N. R., D’Angelo, E., and Ros, E. (2013). Distributed cerebellar plasticity implements adaptable gain control in a manipulation task: a closed-loop robotic simulation. *Frontiers in Neural Circuits*, 7(159).
- [47] Gemmar, P., Gronz, O., Henrichs, T., and Hertel, F. (2008). Advanced methods for target navigation using microelectrode recordings in stereotactic neurosurgery for deep brain stimulation. In *CBMS ’08: Proceedings of the 2008 21st IEEE International Symposium on Computer-Based Medical Systems*, pages 99–104, Washington, DC, USA. IEEE Computer Society.
- [48] Gerfen, C., Engber, T., Mahan, L., Susel, Z., Chase, T., Monsma, F., and Sibley, D. (1990). D1 and d2 dopamine receptor-regulated gene expression of striatonigral and striatopallidal neurons. *Science*, 250(4986):1429–1432.
- [49] Golgi, C. (1967). *The Neuron Doctrine – Theory and Facts*. Nobel Lectures, Physiology or Medicine. Elsevier Publishing.
- [50] Goodman, D. F. M. and Brette, R. (2009). The BRIAN simulator. *Frontiers in Neuroscience*, 3(26).
- [51] Gouze, A., Antonini, M., Barlaud, M., and Macq, B. (2004). Design of signal-adapted multidimensional lifting scheme for lossy coding. *IEEE Transactions on Image Processing*, 13(12):1589–1603.
- [52] Graf, W., Simpson, J. I., and Leonard, C. S. (1988). Spatial organization of visual messages of the rabbit’s cerebellar flocculus. ii. complex and simple spike responses of purkinje cells. *Journal of Neurophysiology*, 60(6):2091–2121.
- [53] Guido, R. C., Slaets, J. F. W., Köberle, R., Almeida, L. O. B., and Pereira, J. C. (2006). A new technique to construct a wavelet transform matching a specified signal with applications to digital, real time, spike, and overlap pattern recognition. *Digital Signal Processing*, 16(1):24–44.
- [54] Gurney, K., Prescott, T. J., Wickens, J. R., and Redgrave, P. (2004). Computational models of the basal ganglia: from robots to membranes. *Trends in Neurosciences*, 27(8):453–459.
- [55] Gurney K1, Prescott TJ, R. P. (2001). A computational model of action selection in the basal ganglia. ii. analysis and simulation of behaviour. *Biol Cybernetics*, 84(6):411–423.
- [56] Helmich, R. C., Hallett, M., Deuschl, G., Toni, I., and Bloem, B. R. (2012). Cerebral causes and consequences of parkinsonian resting tremor: a tale of two circuits? *Brain*, pages 1–21.
- [57] Highstein, S., Porritt, J., and Dean, P. (2005). Report on a workshop concerning the cerebellum and motor learning. *The Cerebellum*, 4:140–150.
- [58] Hirata, Y., Blazquez, P. M., Inagaki, K., Furuta, K., and Highstein, S. M. (2006). Flocculus purkinje cell complex spikes during acute motor learning of the horizontal vestibuloocular reflex in squirrel monkeys. In *Program No. 805.6. 2006 Abstract Viewer/Itinerary Planner: Society for Neuroscience*.
- [59] Hirata, Y., Blazquez, P. M., Inagaki, K., Furuta, K., and Highstein, S. M. (2007). Cerebellar flocculus purkinje cell complex spikes during VOR in the dark before and after VOR motor learning in squirrel monkeys. In *Program No. 190.3. 2007 Abstract Viewer/Itinerary Planner: Society for Neuroscience*.

- [60] Hirata, Y. and Highstein, S. M. (2001). Acute adaptation of the vestibuloocular reflex: Signal processing by floccular and ventral parafloccular purkinje cells. *Journal of Neurophysiology*, 85(5):2267–2288.
- [61] Hirata, Y., Lockard, J. M., and Highstein, S. M. (2002). Capacity of vertical VOR adaptation in squirrel monkey. *Journal of Neurophysiology*, 88(6):3194–3207.
- [62] Hofstoetter, C., Gil, M., Eng, K., Indiveri, G., Mintz, M., Kramer, J., and Verschure, P. (2004). The cerebellum chip: an analog vlsi implementation of a cerebellar model of classical conditioning. In *NIPS'04*, volume 17, pages 577–584.
- [63] Hofstotter, C., Mintz, M., and Verschure, P. (2002). The cerebellum in action: a simulation and robotics study. *European Journal of Neuroscience*, 16(7):1361–1376.
- [64] Hopp, J. and Fuchs, A. F. (2004). The characteristics and neuronal substrate of saccadic eye movement plasticity. *Progress in Neurobiology*, 72(1):27 – 53.
- [65] Hu, D., Shen, H., and Zhou, Z. (2008). Functional asymmetry in the cerebellum: A brief review. *The Cerebellum*, 7(3):304–313.
- [66] Huang, C.-C., Sugino, K., Shima, Y., Guo, C., Bai, S., Mensh, B. D., Nelson, S. B., and Hantman, A. W. (2013). Convergence of pontine and proprioceptive streams onto multimodal cerebellar granule cells. *eLife*, 2.
- [67] Ito, M. (1998). Cerebellar learning in the vestibulo-ocular reflex. *Trends in cognitive sciences*, 2(9):313–321.
- [68] Ito, M. (2000). Mechanisms of motor learning in the cerebellum. *Brain Research*, 886(1–2):237–245.
- [69] Ito, M. (2011). *The Cerebellum: Brain for an Implicit Self*. FT Press Science. Pearson Education.
- [70] Ito, M. (2013). Error detection and representation in the olivo-cerebellar system. *Frontiers in Neural Circuits*, 7(1).
- [71] Ito, M., Sakurai, M., and Pavich, T. (1982). Climbing fibre induced depression of both mossy fibre responsiveness and glutamate sensitivity of cerebellar purkinje cells. *Physiology*, (324):113–134.
- [72] Jancke, L., Specht, K., Mirzazade, S., and Peters, M. (1999). The effect of finger-movement speed of the dominant and the subdominant hand on cerebellar activation: A functional magnetic resonance imaging study. *NeuroImage*, 9(5):497 – 507.
- [73] Jinzhu Peng, Y. W. and Sun, W. (2007). Trajectory-tracking control for mobile robot using recurrent fuzzy cerebellar model articulation controller. *Neural Information Processing*, 11(1):15–23.
- [74] Johansson, C. and Lansner, A. (2007). Towards cortex sized artificial neural systems. *Neural Networks*, 20(1):48–61.
- [75] Kanerva, P. (1988). *Sparse Distributed Memory*. MIT Press, Cambridge, MA, USA.
- [76] Kapoula, Z., Eggert, T., and Bucci, M. P. (1996). Disconjugate adaptation of the vertical oculomotor system. *Vision Research*, 36(17):2735–2745.

- [77] Kassardjian, C. D., Tan, Y.-F., Chung, J.-Y. J., Heskin, R., Peterson, M. J., and Broussard, D. M. (2005). The site of a motor memory shifts with consolidation. *The Journal of Neuroscience*, 25(35):7979–7985.
- [78] Kawato, M. (1999). Internal models for motor control and trajectory planning. *Current Opinion in Neurobiology*, 9(6):718–727.
- [79] Kawato, M. (2008). From understanding the brain by creating the brain towards manipulative neuroscience. *Philosophical Transactions of the Royal Society London B Biological Sciences*, 363(1500):2201–2214.
- [80] Kawato, M. and Gomi, H. (1992a). The cerebellum and VOR/OKR learning models. *Trends in Neurosciences*, 15(11):445–453.
- [81] Kawato, M. and Gomi, H. (1992b). A computational model of four regions of the cerebellum based on feedback-error learning. *Biological Cybernetics*, 68(2):95–103.
- [82] Kemp, J. M. and Powell, T. P. S. (1971). The connexions of the striatum and globus pallidus: Synthesis and speculation. *Philosophical Transactions of the Royal Society of London. B, Biological Sciences*, 262(845):441–457.
- [83] Kettner, R. E., Mahamud, S., Leung, H.-C., Sitkoff, N., Houk, J. C., Peterson, B. W., and Barto, A. G. (1997). Prediction of complex two-dimensional trajectories by a cerebellar model of smooth pursuit eye movement. *Journal of Neurophysiology*, 77(4):2115–2130.
- [84] Kim, J. C. C., Cook, M. N., Carey, M. R., Shen, C., Regehr, W. G., and Dymecki, S. M. (2009). Linking genetically defined neurons to behavior through a broadly applicable silencing allele. *Neuron*, 63(3):305–315.
- [85] Kitazawa, S., Kimura, T., and Yin, P.-B. (1998). Cerebellar complex spikes encode both destinations and errors in arm movements. *Nature*, 392:494–497.
- [86] Kobayashi, Y., Kawano, K., Takemura, A., Inoue, Y., Kitama, T., Gomi, H., and Kawato, M. (1998). Temporal firing patterns of purkinje cells in the cerebellar ventral paraflocculus during ocular following responses in monkeys ii. complex spikes. *Journal of Neurophysiology*, 80(2):832–848.
- [87] Kojima, Y., Soetedjo, R., and Fuchs, A. F. (2010). Changes in simple spike activity of some purkinje cells in the oculomotor vermis during saccade adaptation are appropriate to participate in motor learning. *The Journal of Neuroscience*, 30(10):3715–3727.
- [88] Kostis, M., Konstantina, N., Georgios, T., and Damianos, S. (2009). Towards input output non-linear modeling of the subthalamic nucleus using intranuclear recordings. pages 601–604.
- [89] Lemij, H. and Collewijn, H. (1991). Long-term nonconjugate adaptation of human saccades to anisometropic spectacles. *Vision Research*, 31(11):1939–1954.
- [90] Lenz, A., Anderson, S., Pipe, A., Melhuish, C., Dean, P., and Porrill, J. (2009). Cerebellar-inspired adaptive control of a robot eye actuated by pneumatic artificial muscles. *IEEE Transactions on Systems, Man, and Cybernetics, Part B: Cybernetics*, 39(6):1420–1433.
- [91] LevRam, V., Wong, S. T., Storm, D. R., and Tsien, R. Y. (2002). A new form of cerebellar long-term potentiation is postsynaptic and depends on nitric oxide but not cAMP. *Proceedings of the National Academy of Sciences*, 99:8389–8393.

- [92] Li, Z., Yang, C., and Fan, L. (2013). *Advanced Control of Wheeled Inverted Pendulum Systems*. Springer.
- [93] Lin, C.-M. and Chen, C.-H. (2007). Robust fault-tolerant control for a biped robot using a recurrent cerebellar model articulation controller. *IEEE Transactions on Systems, Man, and Cybernetics, Part B: Cybernetics*, 37(1):110–123.
- [94] Lisberger, S. G., Pavelko, T. A., and Broussard, D. M. (1994). Neural basis for motor learning in the vestibuloocular reflex of primates. i. changes in the responses of brain stem neurons. *Journal of Neurophysiology*, 72(2):928–953.
- [95] Llinas, R. R. (2011). Cerebellar motor learning versus cerebellar motor timing: the climbing fibre story. *The Journal of Physiology*, 589(14):3423–3432.
- [96] Maex, R. and De Schutter, E. (1998). Synchronization of golgi and granule cell firing in a detailed network model of the cerebellar granule cell layer. *Journal of Neurophysiology*, 80(5):2521–2537.
- [97] Maex, R. and De Schutter, E. (2005). Oscillations in the cerebellar cortex: a prediction of their frequency bands. In *Creating coordination in the cerebellum*, volume 148 of *Progress in Brain Research*, pages 181–188. Elsevier.
- [98] Malenka, R. C. and Bear, M. F. (2004). LTP and LTD: An embarrassment of riches. *Neuron*, 44(1):5–21.
- [99] Manni, E. and Petrosini, L. (1997). Luciani’s work on the cerebellum a century later. *Trends in Neurosciences*, 20(3):112–116.
- [100] Mano, N.-I. (1974). Simple and complex spike activities of the cerebellar purkinje cell in relation to selective alternate movement in intact monkey. *Brain Research*, 70(3):381 – 393.
- [101] Manto, M., Bower, J., Conforto, A. B., Delgado-García, J., Guarda, S., Gerwig, M., Habas, C., Hagura, N., Ivry, R., Mariën, P., Molinari, M., Naito, E., Nowak, D., Oulad Ben Taib, N., Pelisson, D., Tesche, C., Tilikete, C., and Timmann, D. (2012). Consensus paper: Roles of the cerebellum in motor control: the diversity of ideas on cerebellar involvement in movement. *The Cerebellum*, 11(2):457–487.
- [102] Manto, M., Schmahmann, J. D., Rossi, F., Gruol, D. L., and Koibuchi, N. (2013). *Handbook of the Cerebellum and Cerebellar Disorders*. Springer Netherlands.
- [103] Marr, D. (1969). A theory of cerebellar cortex. *The Journal of Physiology*, 202(2):437–470.
- [104] Marti, S., Bockisch, C., and Straumann, D. (2006). Asymmetric short-term adaptation of the vertical vestibulo-ocular reflex in humans. *Experimental Brain Research*, 172(3):343–350.
- [105] McElvain, L. E., Bagnall, M. W., Sakatos, A., and du Lac, S. (2010). Bidirectional plasticity gated by hyperpolarization controls the gain of postsynaptic firing responses at central vestibular nerve synapses. *Neuron*, 68(4):763–775.
- [106] Medina, J. F. and Lisberger, S. G. (2008). Links from complex spikes to local plasticity and motor learning in the cerebellum of awake-behaving monkeys. *Nature Neuroscience*, 11:1185–1192.
- [107] Medina, J. F. and Mauk, M. D. (2000). Computer simulation of cerebellar information processing. *Nature Neuroscience*, 3:1205–1211.

- [108] Melvill Jones, G., Guitton, D., and Berthoz, A. (1988). Changing patterns of eye-head coordination during 6 h of optically reversed vision. *Experimental Brain Research*, 69(3):531–544.
- [109] Migliore, M., Cannia, C., Lytton, W. W., Markram, H., Hines, M. L., and Migliore, M. (2006). Parallel network simulations with NEURON. *Journal of Computational Neuroscience*, 21:119–129.
- [110] Mink, J. W. and Thach, W. (1993). Basal ganglia intrinsic circuits and their role in behavior. *Current Opinion in Neurobiology*, 3(6):950–957.
- [111] Newman, M. E. J. (2003). The structure and function of complex networks. *SIAM REVIEW*, 45:167–256.
- [112] O'Donoghue, D., King, J., and Bishop, G. (1989). Physiological and anatomical studies of the interactions between purkinje cells and basket cells in the cat's cerebellar cortex: evidence for a unitary relationship. *The Journal of Neuroscience*, 9(6):2141–2150.
- [113] Ohki, M., Kitazawa, H., Hiramatsu, T., Kaga, K., Kitamura, T., Yamada, J., and Nagao, S. (2009). Role of primate cerebellar hemisphere in voluntary eye movement control revealed by lesion effects. *Journal of Neurophysiology*, 101(2):934–947.
- [114] Ophir, B., Lustig, M., and Elad, M. (2011). Multi-scale dictionary learning using wavelets. *IEEE Journal of Selected Topics in Signal Processing*, 5(5):1014–1024.
- [115] Overwalle, F. V., Baetens, K., Marian, P., and Vandekerckhove, M. (2013). Social cognition and the cerebellum: A meta-analysis of over 350 fMRI studies. *Neuroimage*, 86(1):554–572.
- [116] Paige, G. and Sargent, E. (1991). Visually-induced adaptive plasticity in the human vestibulo-ocular reflex. *Experimental Brain Research*, 84(1):25–34.
- [117] Panouilleres, M., Neggers, S. F., Gutteling, T. P., Salemme, R., Stigchel, S. v. d., van der Geest, J. N., Frens, M. A., and Pélinson, D. (2012). Transcranial magnetic stimulation and motor plasticity in human lateral cerebellum: Dual effect on saccadic adaptation. *Human Brain Mapping*, 33(7):1512–1525.
- [118] Parent, A. (1986). *Comparative neurobiology of the basal ganglia*. Willey and Sons.
- [119] Parent, A. (2012). The history of the basal ganglia: The contribution of karl friedrich burdach. *Neuroscience and Medicine*, 3(4):374–379.
- [120] Pellionisz, A. and Llinas, R. (1979). Brain modeling by tensor network theory and computer simulation. the cerebellum: Distributed processor for predictive coordination. *Neuroscience*, 4(3):323–348.
- [121] Pinzon-Morales, R., Garces-Arboleda, M., and Orozco-Gutierrez, A. (2009). Automatic identification of various nuclei in the basal ganglia for parkinson's disease neurosurgery. In *Annual International Conference of the IEEE Engineering in Medicine and Biology Society*, pages 3473–3476.
- [122] Pinzon-Morales, R. and Hirata, Y. (2013). Cerebellar inspired bi-hemispherical neural network for adaptive control of an unstable robot. In *Confenrence on Biosignals and Biorobotics BRC 2013*, pages 1–4.

- [123] Pinzon-Morales, R. and Hirata, Y. (2014a). A bi-hemispheric neuronal network model of the cerebellum with spontaneous climbing fiber firing produces asymmetrical motor learning during robot control. *Frontiers in Neural Circuits*, 8(131).
- [124] Pinzon-Morales, R. and Hirata, Y. (2014b). Error signals used for cerebellar motor learning: evaluation in real world adaptive robot control using a cerebellar neuronal network model. *in review*.
- [125] Pinzon-Morales, R. and Hirata, Y. (2014c). An stand-alone and portable bi-hemispherical neuronal network model of the cerebellum for engineering applications. In *IEEE International Conference on Robotics and Biomimetics (ROBIO)*, pages 1–4.
- [126] Pinzon-Morales, R., Orozco-Gutierrez, A., Carmona-Villada, H., and Castellanos, C. (2010). Towards high accuracy classification of mer signals for target localization in parkinson's disease. In *Annual International Conference of the IEEE Engineering in Medicine and Biology Society (EMBC)*, pages 4040–4043.
- [127] Pinzon-Morales, R., Orozco-Gutierrez, A., and Castellanos-Dominguez, G. (2011a). EEG seizure identification by using optimized wavelet decomposition. In *Annual International Conference of the IEEE in Engineering in Medicine and Biology Society, EMBC*, pages 2675–2678.
- [128] Pinzon-Morales, R.-D. and Hirata, Y. (2012). Customization of wavelet function for pupil fluctuation analysis to evaluate levels of sleepiness. In *Proceedings of the 11th International Conference on Telecommunications and Informatics, Proceedings of the 11th International Conference on Signal Processing*, pages 115–120, Stevens Point, Wisconsin, USA. World Scientific and Engineering Academy and Society (WSEAS).
- [129] Pinzon-Morales, R. D., Orozco-Gutierrez, A. A., and Castellanos-Dominguez, G. (2011b). Novel signal-dependent filter bank method for identification of multiple basal ganglia nuclei in parkinsonian patients. *Journal of Neural Engineering*, 8(3):036026.
- [130] Pogula Sridhar, S. (2005). Developing neural network applications using labview. Master's thesis, University of Missouri–Columbia.
- [131] Porrill, J. and Dean, P. (2007). Recurrent cerebellar loops simplify adaptive control of redundant and nonlinear motor systems. *Neural Computation*, 19(1):170–193.
- [132] Ramón y Cajal, S. (1967). The structure and connections of neurons. Elsevier Publishing.
- [133] Raymond, J. L. and Lisberger, S. G. (1998). Neural learning rules for the vestibulo-ocular reflex. *The Journal of Neuroscience*, 18(21):9112–9129.
- [134] Redgrave, P., Prescott, T., and Gurney, K. (1999). The basal ganglia: a vertebrate solution to the selection problem? *Neuroscience*, 89(4):1009–1023.
- [135] Ruan, X. and Chen, J. (2011). On-line nnac for a balancing two-wheeled robot using feedback-error-learning on the neurophysiological mechanism. *Journal of Computers*, 6(3).
- [136] Salin, P. A., Malenka, R. C., and Nicoll, R. A. (1996). Cyclic AMP mediates a presynaptic form of LTP at cerebellar parallel fiber synapses. *Neuron*, 16(4):797–803.
- [137] Santaniello, S., Fiengo, G., Glielmo, L., and Catapano, G. (2008). A biophysically inspired microelectrode recording-based model for the subthalamic nucleus activity in parkinson's disease. *Biomedical Signal Processing and Control*, 3(3):203–211.

- [138] Schilling, K., Oberdick, J., Rossi, F., and Baader, S. (2008). Besides purkinje cells and granule neurons: an appraisal of the cell biology of the interneurons of the cerebellar cortex. *Histochemistry and Cell Biology*, 130(4):601–615.
- [139] Schonewille, M., Gao, Z., Boele, H.-J., Veloz, M. F. V., Amerika, W. E., Simek, A. A., Jeu, M. T. D., Steinberg, J., Takamiya, K., Hoebeek, F. E., Linden, D. J., Huganir, R. L., and De Zeeuw, C. I. (2011). Reevaluating the role of LTD in cerebellar motor learning. *Neuron*, 70(1):43–50.
- [140] Schweighofer, N., Doya, K., and Lay, F. (2001). Unsupervised learning of granule cell sparse codes enhances cerebellar adaptive control. *Neuroscience*, 103(1):35–50.
- [141] Snow, R., Hore, J., and Vilis, T. (1985). Adaptation of saccadic and vestibulo-ocular systems after extraocular muscle tenectomy. *Investigative Ophthalmology and Visual Science*, 26(7):924–31.
- [142] Snyder, P. J., Bilder, R. M., Wu, H., Bogerts, B., and Lieberman, J. A. (1995). Cerebellar volume asymmetries are related to handedness: A quantitative MRI study. *Neuropsychologia*, 33(4):407–419.
- [143] Solinas, S., Nieus, T., and D’Angelo, E. (2010). A realistic large-scale model of the cerebellum granular layer predicts circuit spatio-temporal filtering properties. *Frontiers in Cellular Neuroscience*, 4(12).
- [144] Solodkin, A., Hlustik, P., Noll, D. C., and Small, S. L. (2001). Lateralization of motor circuits and handedness during finger movements. *European Journal of Neurology*, 8(5):425–434.
- [145] Spencer, R., Ivry, R., and Zelaznik, H. (2005). Role of the cerebellum in movements: control of timing or movement transitions? *Experimental Brain Research*, 161(3):383–396.
- [146] Steiner, H. and Tseng, K. Y. (2010). Handbook of behavioral neuroscience. volume 20 of *Handbook of Basal Ganglia Structure and Function*. Elsevier.
- [147] Stone, L. S. and Lisberger, S. G. (1990). Visual responses of purkinje cells in the cerebellar flocculus during smooth-pursuit eye movements in monkeys. ii. complex spikes. *Journal of Neurophysiology*, 63(5):1262–1275.
- [148] Strata, P. (2009). David Marr’s theory of cerebellar learning: 40 years later. *The Journal of Physiology*, 587(23):5519–5520.
- [149] Sweldens, W. (1996). The lifting scheme: A custom-design construction of biorthogonal wavelets. *Applied and Computational Harmonic Analysis*, 3(2):186–200.
- [150] Takemura, A., Inoue, Y., Gomi, H., Kawato, M., and Kawano, K. (2001). Change in neuronal firing patterns in the process of motor command generation for the ocular following response. *Journal of Neurophysiology*, 86(4):1750–1763.
- [151] Tanaka, Y., Ohata, Y., Kawamoto, T., and Hirata, Y. (2010). Adaptive control of 2-wheeled balancing robot by cerebellar neuronal network model. In *Annual International Conference of the IEEE Engineering in Medicine and Biology Society*, pages 1589–1592.
- [152] Thach, W. T. (1996). On the specific role of the cerebellum in motor learning and cognition: Clues from pet activation and lesion studies in man. *Behavioral and Brain Sciences*, 19:411–433.
- [153] Thach, W. T. (1998). What is the role of the cerebellum in motor learning and cognition? *Trends in Cognitive Sciences*, 2(9):331 – 337.

- [154] Trottenberg, T., Kupsch, A., Schneider, G.-H., Brown, P., and Kühn, A. A. (2007). Frequency-dependent distribution of local field potential activity within the subthalamic nucleus in parkinson's disease. *Experimental Neurology*, 205(1):287 – 291.
- [155] Ushio, M., Minor, L., Della Santina, C., and Lasker, D. (2011). Unidirectional rotations produce asymmetric changes in horizontal VOR gain before and after unilateral labyrinthectomy in macaques. *Experimental Brain Research*, 210(3-4):651–660.
- [156] Van de Vijver, D. A. M. C., Roos, R. A. C., Jansen, P. A. F., Porsius, A. J., and de Boer, A. (2001). Estimation of incidence and prevalence of parkinson's disease in the elderly using pharmacy records. *Pharmacoepidemiology and Drug Safety*, 10(6):549–554.
- [157] Veredas, F., Vico, F., and Alonso, J. (2004). A computational tool to simulate correlated activity in neural circuits. *Journal of Neuroscience Methods*, 136(1):23 – 32.
- [158] Verschure, P. F. M. J. and Mintz, M. (2001). A real-time model of the cerebellar circuitry underlying classical conditioning: A combined simulation and robotics study. *Neurocomputing*, 38-40:1019–1024.
- [159] Wada, N., Kishimoto, Y., Watanabe, D., Kano, M., Hirano, T., Funabiki, K., and Nakanishi, S. (2007). Conditioned eyeblink learning is formed and stored without cerebellar granule cell transmission. *Proceedings of the National Academy of Sciences*, 104(42):16690–16695.
- [160] Wang, G., Wang, Z., Chen, W., and Zhuang., J. (2006). Classification of surface emg signals using optimal wavelet packet method based on davies-bouldin criterion. *Springer Medicine and Biological Engineering*, 44(10):865–872.
- [161] Welsh, J. P., Yamaguchi, H., Zeng, X.-H., Kojo, M., Nakada, Y., Takagi, A., Sugimori, M., and Llinás, R. R. (2005). Normal motor learning during pharmacological prevention of purkinje cell long-term depression. *Proceedings of the National Academy of Sciences of the United States of America*, 102(47):17166–17171.
- [162] Wen, C.-M. and Cheng, M.-Y. (2013). Development of a recurrent fuzzy cmac with adjustable input space quantization and self-tuning learning rate for control of a dual-axis piezoelectric actuated micromotion stage. *IEEE Transactions on Industrial Electronics*, 60(11):5105–5115.
- [163] Wolpert, D. M., Miall, R., and Kawato, M. (1998). Internal models in the cerebellum. *Trends in Cognitive Sciences*, 2(9):338–347.
- [164] Wong, S., Baltuch, G. H., Jaggi, J. L., and Danish, S. F. (2009). Functional localization and visualization of the subthalamic nucleus from microelectrode recordings acquired during dbs surgery with unsupervised machine learning. *Journal of Neural Engineering*, 6(2):026006.
- [165] Wong, Y.-F. and Sideris, A. (1992). Learning convergence in the cerebellar model articulation controller. *IEEE Transactions on Neural Networks*, 3(1):115–121.
- [166] Wu, T. and Hallett, M. (2013). The cerebellum in parkinson's disease. *Brain*, 136(3):696–709.
- [167] Xiang, H., Lin, C., Ma, X., Zhang, Z., Bower, J. M., Weng, X., and Gao, J.-H. (2003). Involvement of the cerebellum in semantic discrimination: An fMRI study. *Human Brain Mapping*, 18(3):208–214.
- [168] Yamazaki, T. and Igarashi, J. (2013). Realtime cerebellum: A large-scale spiking network model of the cerebellum that runs in realtime using a graphics processing unit. *Neural Networks*, 47(0):103–111.

- [169] Yoshikawa, A. and Hirata, Y. (2006). Mechanism of frequency selectivity in VOR motor learning: Frequency channel or waveform learning? In *Annual International Conference of the IEEE Engineering in Medicine and Biology Society*, pages 6217–6220.
- [170] Zaidel, A., Spivak, A., Shpigelman, L., Bergman, H., and Israel, Z. (2009). Delimiting subterritories of the human subthalamic nucleus by means of microelectrode recordings and a hidden markov model. *Movement Disorders*, 24(12):1785–1793.
- [171] Zhen, L., Zhengjia, H., Yanyang, Z., and Yanxue, W. (2008). Customized wavelet denoising using intra- and inter-scale dependency for bearing fault detection. *Journal of Sound and Vibration*, 313(1-2):342–359.
- [172] Ziegler, J. G. and Nichols, N. B. (1942). Optimum settings for automatic controllers. *Transactions of ASME*, 64:759–768.

A

LabVIEW framework for building neuronal network models of the cerebellum

Submitted to Advances in Engineering Software Pinzon-Morales, R D and Hirata, Y.

THE implementation of neural network models of the cerebellum and other brain areas have been carried out in computational efficient programming languages such as BRIAN⁵⁰, Neuron¹⁰⁹, NEST¹⁵⁷, among others¹⁴. These software packages are exceedingly robust for detailed simulations of neural networks and they represent advantageous tools for studying and predicting the behavior of biological systems. However, these softwares lack the flexibility that LabVIEW offers for integration of user interfaces with hardware and software. LabVIEW is multi-platform visual programming language commonly used for data acquisition, instrument control, and industrial automation. A key feature of LabVIEW is the extensive support for accessing instrumentation hardware. These characteristics make LabVIEW an outstanding platform for implementation of cerebellar models and their integration into engineering application. Multilayer perceptron artificial neural networks have been demonstrated in LabVIEW, however, their number of neurons are rarely beyond 20^{130} .

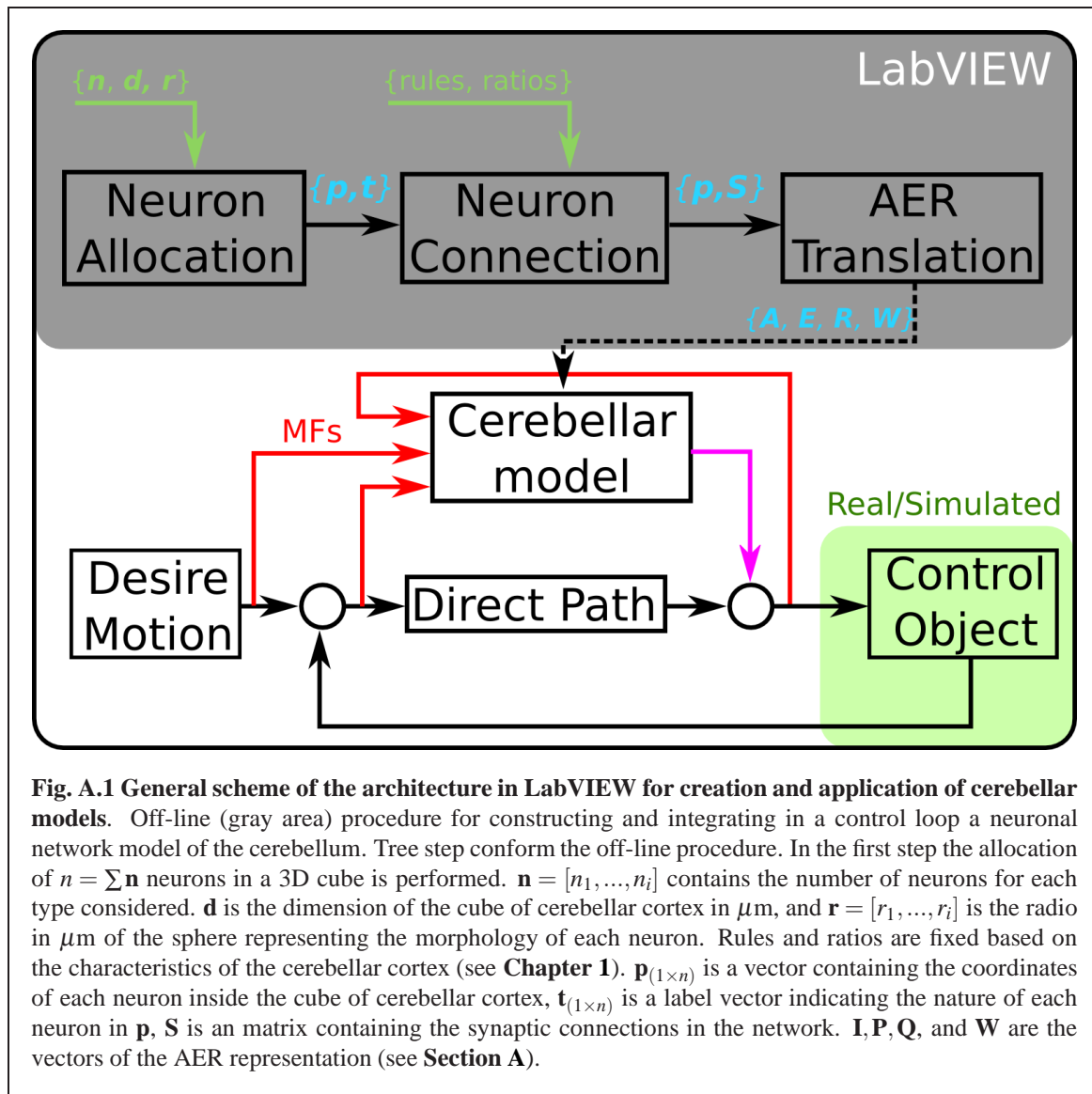


Fig. A.1 General scheme of the architecture in LabVIEW for creation and application of cerebellar models. Off-line (gray area) procedure for constructing and integrating in a control loop a neuronal network model of the cerebellum. Three steps conform the off-line procedure. In the first step the allocation of $n = \sum n_i$ neurons in a 3D cube is performed. $\mathbf{n} = [n_1, \dots, n_i]$ contains the number of neurons for each type considered. \mathbf{d} is the dimension of the cube of cerebellar cortex in μm , and $\mathbf{r} = [r_1, \dots, r_i]$ is the radius in μm of the sphere representing the morphology of each neuron. Rules and ratios are fixed based on the characteristics of the cerebellar cortex (see Chapter 1). $\mathbf{p}_{(1 \times n)}$ is a vector containing the coordinates of each neuron inside the cube of cerebellar cortex, $\mathbf{t}_{(1 \times n)}$ is a label vector indicating the nature of each neuron in \mathbf{p} , \mathbf{S} is a matrix containing the synaptic connections in the network. $\mathbf{I}, \mathbf{P}, \mathbf{Q}$, and \mathbf{W} are the vectors of the AER representation (see Section A).

A.1 Introduction

The contribution of this work is the implementation and validation of a software architecture for construction of realistic neural network models of the cerebellum that allow networks with more than 40 k neurons and 220 k synaptic connections to execute in real time. The proposed architecture is developed using the object oriented programming (OOP) design pattern. In addition, the address event representation (AER) strategy is used to describe the structure of the neural network model. These two strategies, OOP and AER, bring to the proposed architecture flexibility, modularity, and scalability.

This architecture has been used thorough this thesis for creating the neural networks of the cerebellum presented. Here the architecture is formalized.

A.2 LabVIEW architecture for constructing and integrating neural network models of the cerebellum in control loops

The proposed architecture for constructing and integrating neural network models of the cerebellum into control engineering applications follows the diagram in **Fig. A.1**. It comprises an off-line three-step procedure for constructing the network, and the on-line execution of the model for integration with the engineering application. The design pattern used in LabVIEW follows the object-oriented programming pattern so that the architecture proposed is flexible, modular, and easily scalable. **Fig. A.2** shows the general class diagram of the architecture. It consists of four classes that encapsulate the methods and data for creating the structure, neurons, synaptic connections, and the AER of the network. Each class is directly related to the steps shown in **Fig. A.1**. Classes cube and neuron, synapses, and AER implement the algorithms for the step neuron allocation, neuron connection, and AER translation, respectively. The class AER also includes the methods for the on-line execution of the cerebellar model.

A.2.1 Off-line construction of the cerebellar network

The first step in the off-line procedure shown in **Fig. A.1** (gray area), consists in allocating the neurons in the model inside the cube representing the cerebellar cortex. Neurons are modeled as spheres. The network is allocated in a 3D space rather than a 2D plane because doing so brings additional spatial features to the neural network that has been shown to carry important information about signal processing in the cerebellum¹⁴³. In this step, the dimension of the cube in μm ($\mathbf{d} = [d_x, d_y, d_z]$), the number of neurons of each type considered $\mathbf{n} = [n_1, \dots, n_t]$, where t is different types of neurons considered (See **Table 3.1**), and the radius of a sphere representing the morphology of each neuron type ($\mathbf{r} = [r_1, \dots, r_t]$) in μm are provided as inputs to the allocation algorithm (**Fig. A.3**). The algorithm works by generating an aleatory and valid xyz coordinate for each neuron in \mathbf{n} (**Fig. A.3A**). To be considered valid, the coordinate must reside inside the cube boundaries and its neighborhood must be free of other neurons (**Fig. A.3B**). The neighborhood is calculated by using the Euclidean distance and the double of the radius of the neuron being allocated (**Fig. A.3C**).

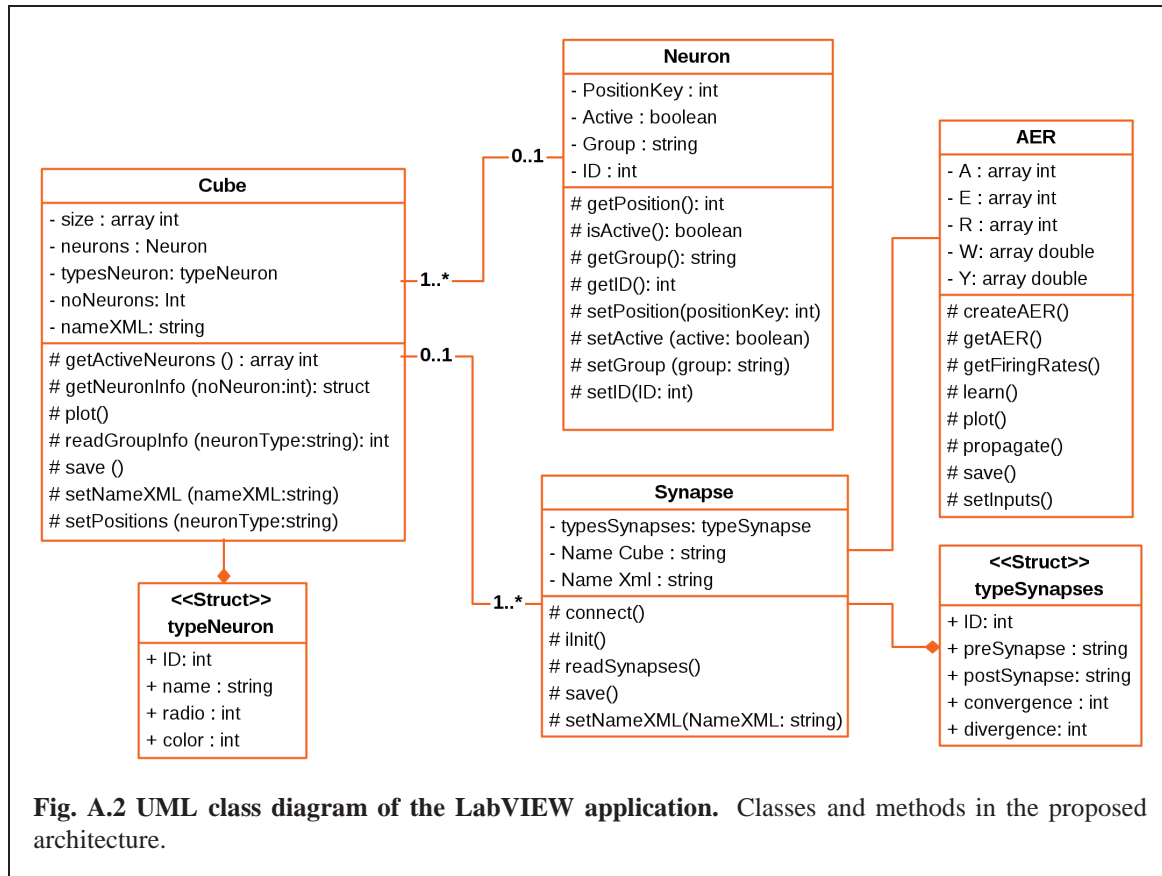


Fig. A.2 UML class diagram of the LabVIEW application. Classes and methods in the proposed architecture.

The output of this stage is the vector $\mathbf{p} = [x_1 + y_1 d_x + z_1 d_x d_y, \dots, x_n + y_n d_x + z_n d_x d_y]$, where $n = \sum \mathbf{n}$, containing the coordinates of each neuron inside the cube.

In the second step, the neurons are connected by following synaptic rules, and the divergence/convergence synaptic ratios shown in **Table 3.1**. The algorithm for connecting each neuron is shown in **Fig. A.4**. The inputs of this algorithm include the vectors $\mathbf{Pre} = [\text{pre}_1, \dots, \text{pre}_{n_s}]$ and $\mathbf{Post} = [\text{post}_1, \dots, \text{post}_{n_s}]$, where n_s is the number of synaptic rules. These two vectors contain the labels of pre-synaptic and post-synaptic neurons according to **Table 3.1**. $\mathbf{c} = [c_1, \dots, c_{n_s}]$ and $\mathbf{d} = [d_1, \dots, d_{n_s}]$ are the convergence/divergence synaptic ratios, \mathbf{p} is output of the algorithm shown in **Fig. A.4**, and $\mathbf{t} = [t_1, \dots, t_n]$ is a vector containing a label indicating the type of each neuron. According to this algorithm each pre-synaptic neuron is connected to the closest post-synaptic neuron (**Fig. A.4A**). The maximum number of inputs in the post-synaptic neuron, or convergence ratio is verified during the connection procedure (**Fig. A.4B**), and the maximum number of projections of the pre-synaptic neuron, or divergence ratio, is also confirmed (**Fig. A.4C**). The distance between pre and post-synaptic neurons is measured as the Euclidean distance. The output of this algorithm is the structure $\mathbf{S} = \{S_1, \dots, S_{n_s}\}$ that contains the matrices of the coordinates

of pre/post synaptic connections according to the synapses embedded in **Table 3.1**. The last step in the procedure for creating a neural network model of the cerebellum is the translation of the coordinates and synapses connections of each neuron (i.e., \mathbf{S}) to the AER format. AER is a compact and efficient (in terms of memory consumption) communication technique for sparse networks and has been successfully extrapolated to neural networks⁷⁴. In AER four vectors are required to describe the network structure, whereas one vector stores the network dynamics (**Fig. A.5**). Regarding the structure, the first vector ($\mathbf{I} = [1, \dots, n]$) encodes the neurons in the network with unique sequential identification numbers (IDs). The second vector ($\mathbf{K} = [k_1, \dots, k_n]$) stores the number of pre-synapses of each neuron. The third and forth vectors encode the IDs of the pre-synaptic neurons ($\mathbf{Q} = [q_1, \dots, q_m]$) and the corresponding synaptic weights ($\mathbf{W} = [w_1, \dots, w_m]$) in a stacked ordered way, where m is the total number of synaptic connections. A vector storing the firing rates of each neuron ($\mathbf{Y} = [y_1, \dots, y_n]$) completes the AER of the cerebellar neuronal network. For the example network in **Fig. A.5**, neuron #3 is reached by two neurons (#4, #2); this information is clearly seen in the fourth element of $\mathbf{K}[4] = 2$ (red arrows **Fig. A.5**). The synapses reaching this neuron and their synaptic weight can be read by first accumulating the number of synapses of the neurons that precede neuron #3 (neuron #1, 2 pre-synapses, neuron #2, 1 pre-synapse) yielding the indexes [3, 4], and then looking up those indexes in the vectors $\mathbf{Q}[3,4] = [2, 4]$ and $\mathbf{W}[3,4] = [0.3, -0.2]$. The AER used here stores the pre-synaptic connections rather than the post-synaptic connections (as was originally presented in⁷⁴) because it is more suitable for dataflow based programming frameworks such as LabVIEW as shown below. The five vectors comprising the AER implementation are the output of the three step algorithm for creating the neuronal network model of the cerebellum. In the next section these vectors are incorporated into the architecture in LabVIEW for executing the model.

A.2.2 Integrating the neural network model to the engineering application

The five vectors composing the AER are encapsulated in the class with the same name (**Fig. A.2**). The execution of the network, namely, computing the inputs/output of each neuron using the AER vector follows the algorithm in **Fig. A.6**. The core of the algorithm computes the firing rate of each neuron as the weighted summation of all the pre-synaptic inputs (**Fig. A.6A**) passed through a sigmoid activation function (**Fig. A.6B**). In this procedure the order of the neurons store in the vector \mathbf{I} is paramount. It follows the flow of data from the input to the output of the cerebellum. In other words MFs are first stored in \mathbf{I} , then BA, GO, GC, and lastly PC. To compute the output at time t of the BAs (i.e., $\mathbf{Y}_{\text{BA}}(t)$), the

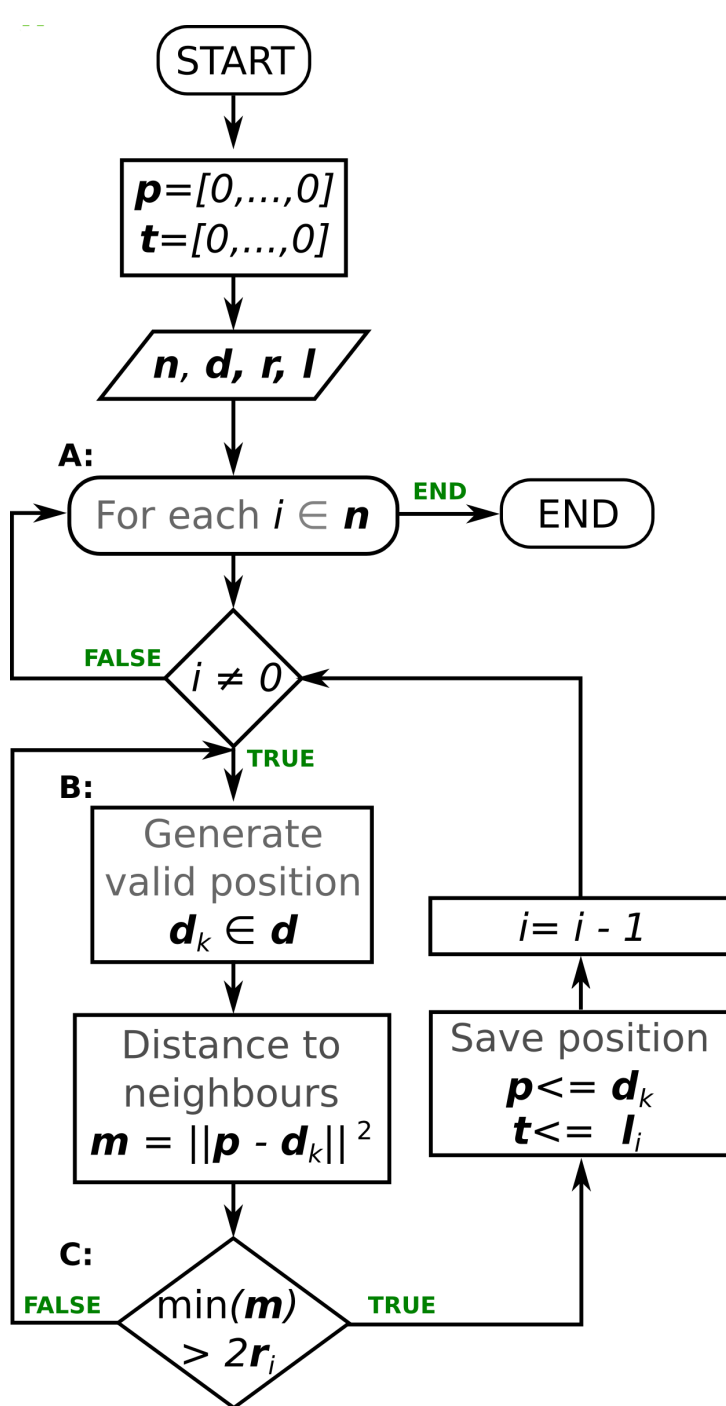


Fig. A.3 Algorithm for allocation of neurons inside the cube of cerebellar cortex. Each neuron is represented by a sphere. p is a vector containing the coordinates of each neuron, t is a label vector indicating the nature of each neuron, n vector containing the number of neurons, d is the dimension of the cube in μm , r is the radio in μm , and l is a vector containing the labels of the types of neurons used.

input from $\mathbf{Y}_{PC}(t - 1)$, and $\mathbf{Y}_{GC}(t - 1)$ are needed and stored in \mathbf{Y} . Then the output of GO ($\mathbf{Y}_{GO}(t)$) is computed using the previously computed $\mathbf{Y}_{BA}(t)$, with the inputs $\mathbf{Y}_{GC}(t - 1)$, and $\mathbf{Y}_{MF}(t)$. In turn, computing $\mathbf{Y}_{GC}(t)$ requires $\mathbf{Y}_{GO}(t)$ and $\mathbf{Y}_{MF}(t)$. Finally the execution of the network is completed by computing $\mathbf{Y}_{PC}(t)$ using $\mathbf{Y}_{GC(t)}$ and $\mathbf{Y}_{BA}(t)$. As shown in **Fig. A.1** (non shadowed area), the cerebellar model can be integrated to a traditional feedback control loop in parallel with the feedback controller employed in the direct path (**Fig. A.1**). The inputs to the cerebellar model are taken from desired motions, error signals, and a copy of the command sent to the control object. In turn, the output of the cerebellar mode can be combined with the output of the direct path to produce the command to the control object.

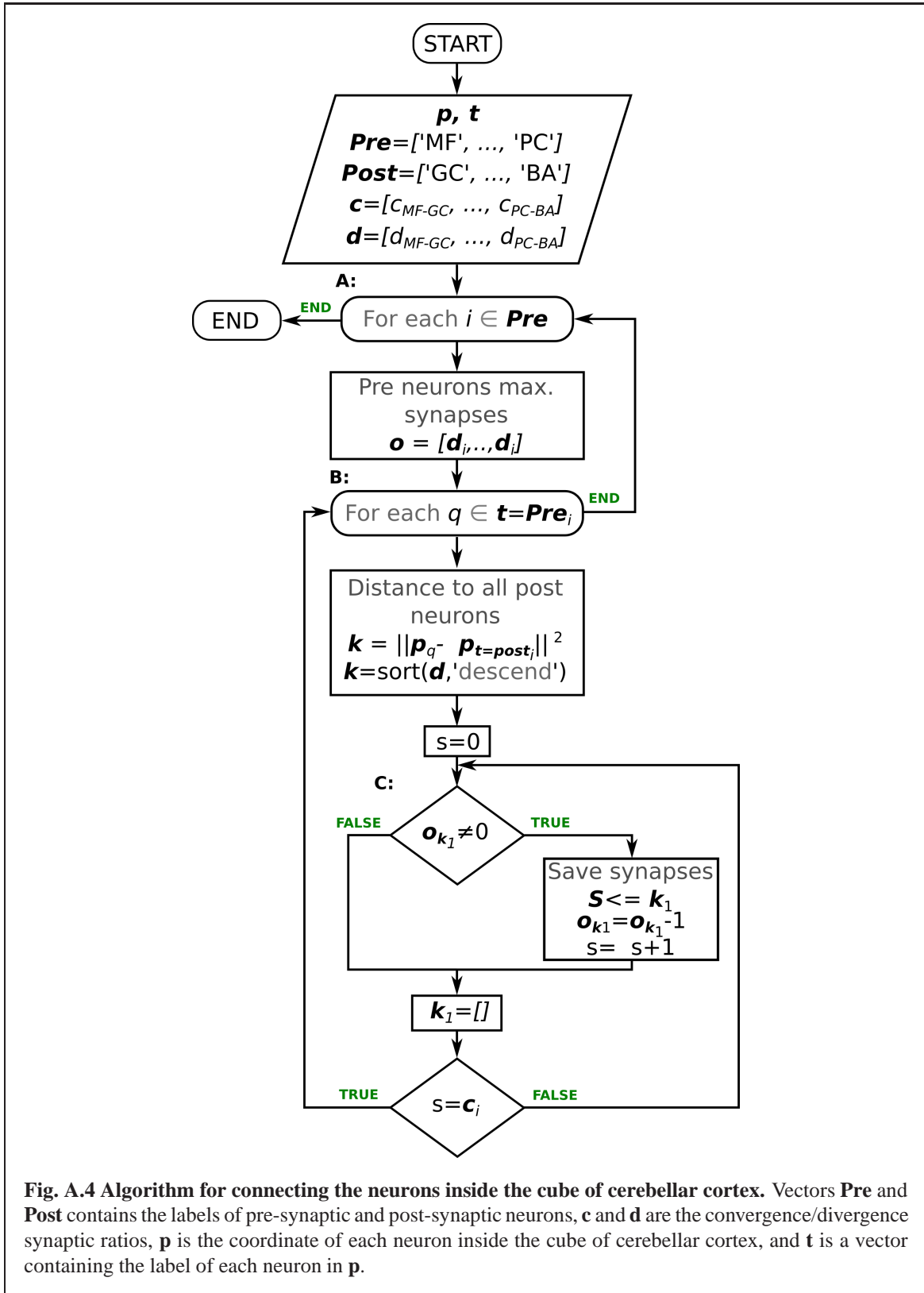
A.3 Results

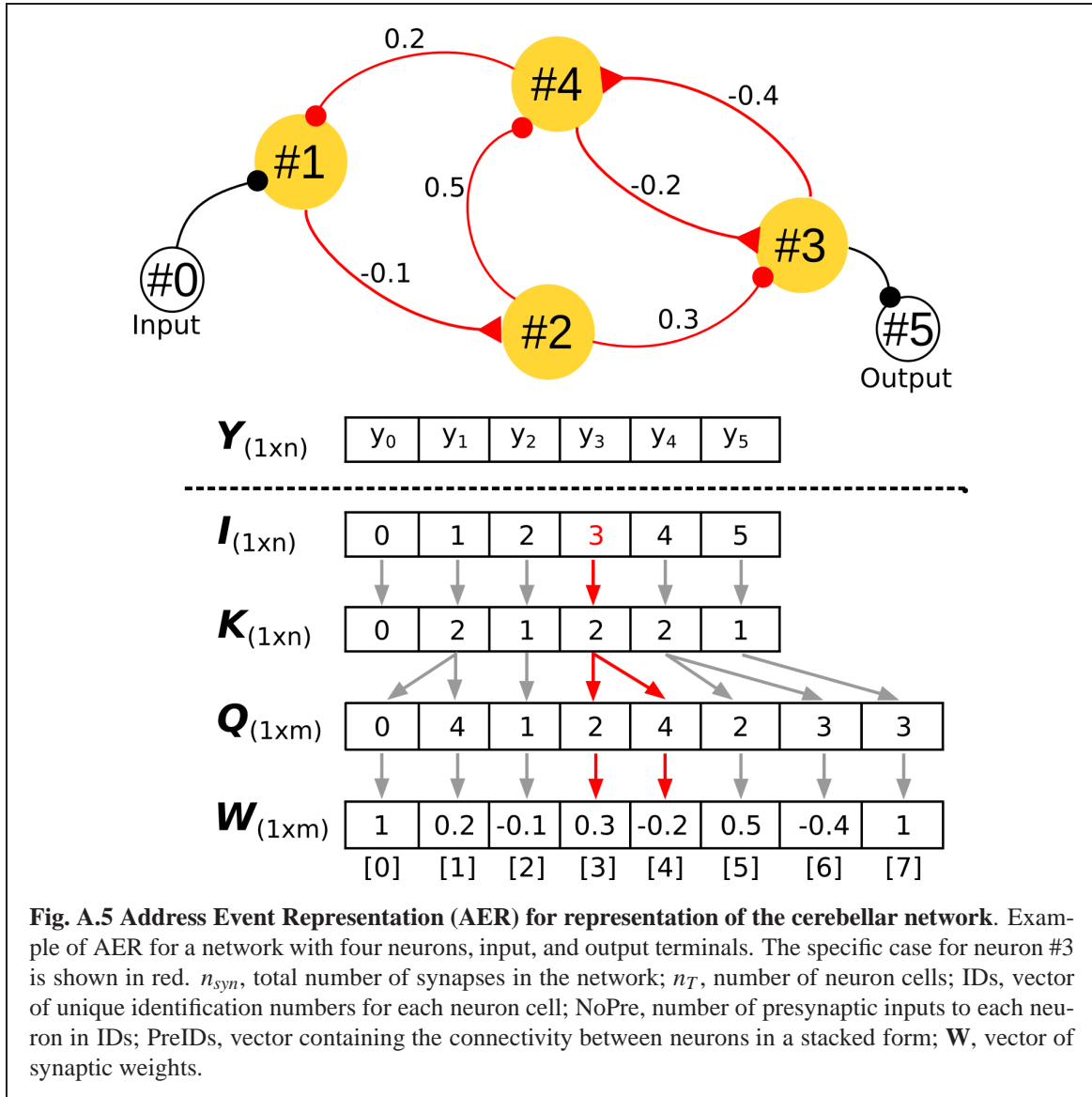
Using the ratios consigned in **Table 3.1** two networks were created with $\mathbf{n}_A = [27, 40, 3, 400, 1]$, $\mathbf{d}_A = [100, 100, 100]$, and $\mathbf{n}_B = [257, 267, 27, 4096, 10]$, $\mathbf{d}_B = [100, 100, 100]$, following the procedure described in **Sec. A.2**. **Fig. A.7** shows these networks. Time required to build up the network A was below 10 s, whereas for the network B was 2 min.

A.4 Conclusions

This appendix presents a software architecture based on LabVIEW to construct and incorporate neural network models of the cerebellum into engineering applications. The proposed architecture is developed using the object oriented programming (OOP) design pattern. In addition, the address event representation (AER) strategy is used to describe the structure of the neural network model. These two strategies, OOP and AER, brings tot he proposed architecture flexibility, modularity, and scalability.

The proposed architecture is used to create a neural network model of the cerebellum and integrate it into the control loop of a direct current (DC) motor and a highly unstable two-wheel balancing robot. This two control scenarios demonstrate not only the effectiveness of the proposed architecture to easy the creation and application of the cerebellar model, but also the benefits in control performance obtained by the learning capabilities of the model.





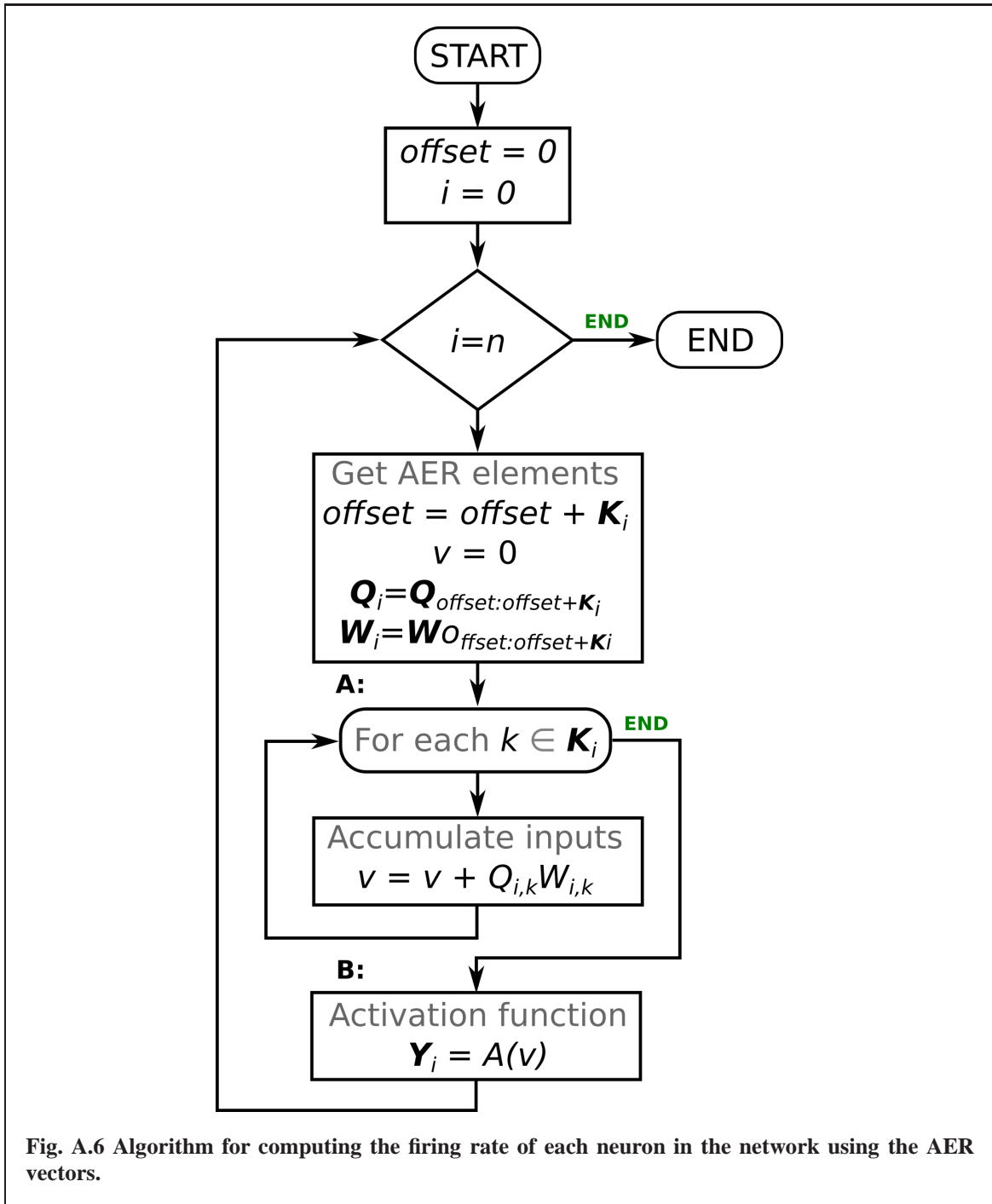


Fig. A.6 Algorithm for computing the firing rate of each neuron in the network using the AER vectors.

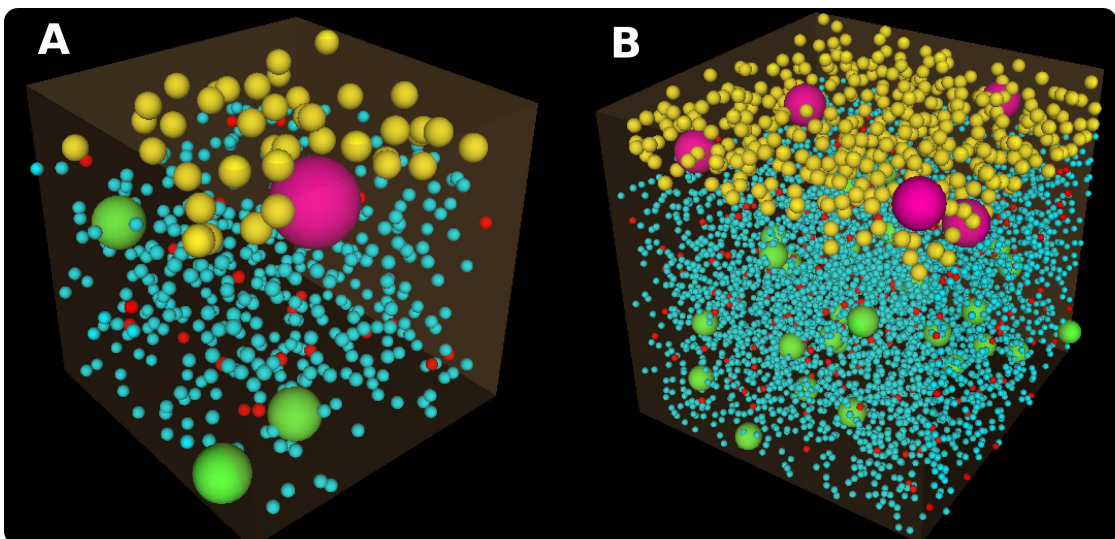


Fig. A.7 Result of the algorithm for allocation of neurons inside the cube of cerebellar cortex using values in Table 3.1. BA (yellow), GC (cyan), GO (green), MF (red), and PCs (magenta) are shown. The scale bar is 10A. $\mathbf{n}_A = [27, 40, 3, 400, 1]$, $\mathbf{d}_A = [100, 100, 100]$. B. $\mathbf{n}_B = [257, 267, 27, 4096, 10]$, $\mathbf{d}_B = [100, 100, 100]$.

B

Mobile and stand alone implementation of the cerebellar model

2014 IEEE international conference on Robotics and Biomimetics Pinzon-Morales,
R D and Hirata, Y.

CONTROL of humanoid robots is one of many engineering applications that have been challenged not only by the engineering community but also by neuroscientists. They provide a unique combination of complexity and similarities with the human body that make them an appealing workbench for understanding how the brain works. Computational models inspired by the brain have been shown to provide both efficient solutions to engineering problems and insights into the function of the biological systems^{79;123}. One brain structure extensively studied and modeled is the cerebellum⁶⁹, which is involved in cognition^{102;115;153} and in motor learning and coordination^{57;69;101;145;152}. Computational models of the cerebellum have been successfully employed in motor control of inverted pendulums^{21;123}, robotic arms^{18;19}, wheeled robots⁶³, humanoid robots^{79;90;168}, among other engineering applications¹⁶².

B.1 Introduction

Due to the computational power required for simulating cerebellar models, the favored target for their implementation has commonly been personal computers, computer clusters, or graphical processor units (GPUs)^{18;168}. However dedicated hardware implementations such as those using field programmable gate arrays (FPGAs)¹⁰ or VLSI circuits⁶² present extra benefits (e.g., speed, real time operation, portability, and low power consumption) that make them alluring for engineering applications. In this chapter I show the first implementation of a bi-hemispherical neuronal network of the cerebellum¹²³ in a stand-alone, portable real time (RT) device. The RT device considered were the National Instruments myRIO-1900. As an example application, the model is tested during a control of the highly unstable two-wheel balancing robot. Comparison of the execution time required by the RT device and a personal computer with different number of neurons and synapses in the cerebellar model is also provided for reference.

B.2 Characteristics of the real time device

The real time device selected to implement the cerebellar model is the National Instruments myRIO-1900 (National Instruments, Austin, TX) shown in **Fig. B.1**. It includes a dual-core ARM Cortex-A9 real-time processor at 667 MHz, 512 MB of DDR3 volatile memory, 2.4 GHz IEEE 802.11 port for wifi remote programming/surveillance, and several multi-purpose input/output ports. In addition the stand-alone myRIO is readily compatible with LabVIEW programming code.

B.3 Results

The robot was commanded to follow 100 cycles of a sinusoidal desired wheel motion ($\phi(t)_{des.} = \pi\sin(2\pi0.25t)$) while the body tilt angle was desired to be constant (90 degrees with respect to the horizontal plane). The number of neurons in each hemisphere of the cerebellar models was set to 300 gr, 2 Go, 20 ba, 1 Pk. These numbers of neurons have been shown to be an optimal selection for the current control object¹²⁵. Variability due to the initial conditions in the cerebellar model, namely, the set of initial random synaptic weights and the synaptic connections, was taken into account by creating 25 permutations of five different sets of random synaptic weights and five different AER tables (i.e., synaptic connections)¹²⁵. Control performance was measured in terms of the root square error (RSE) of the control variable $\phi(t)$. **Fig. B.2** summarizes the control performance attained

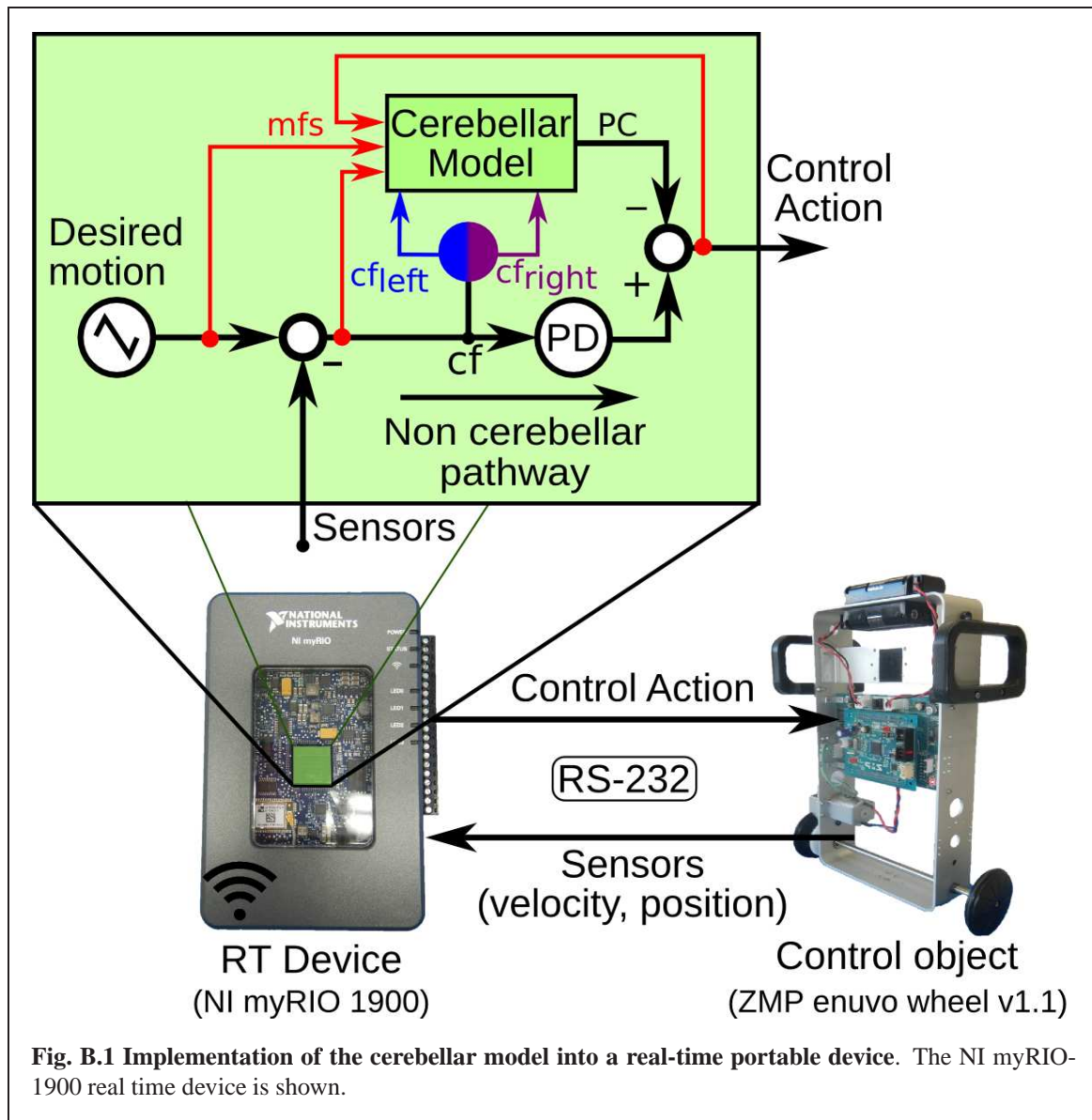


Fig. B.1 Implementation of the cerebellar model into a real-time portable device. The NI myRIO-1900 real time device is shown.

in two different cases. One when the cerebellar model was active (N=10, black traces) and the other when it was inactive (i.e., only the PD controller governed the robot, N=3, gray traces). This figure demonstrates the adaptation happening in the cerebellar model and the general improvement in control performance.

In the experiments presented here a total of 646 neurons were employed because it is an optimal size for the current control task and control object¹²⁵. However, larger cerebellar models can be deployed using the myRIO-1900 device. We measured the average processing time for one execution of the cerebellar model of different sizes using the resident Profiler tool in LabVIEW. For reference purpose, the cerebellar model is also executed

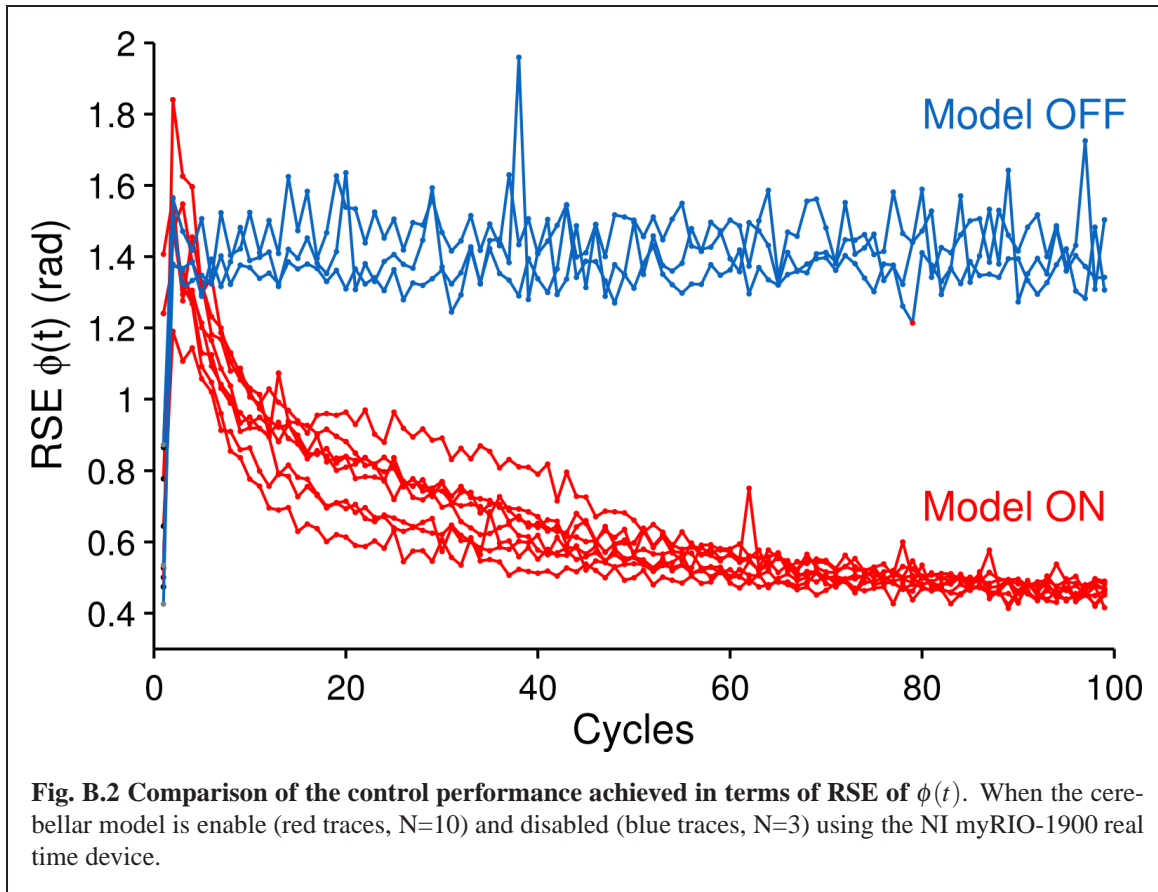
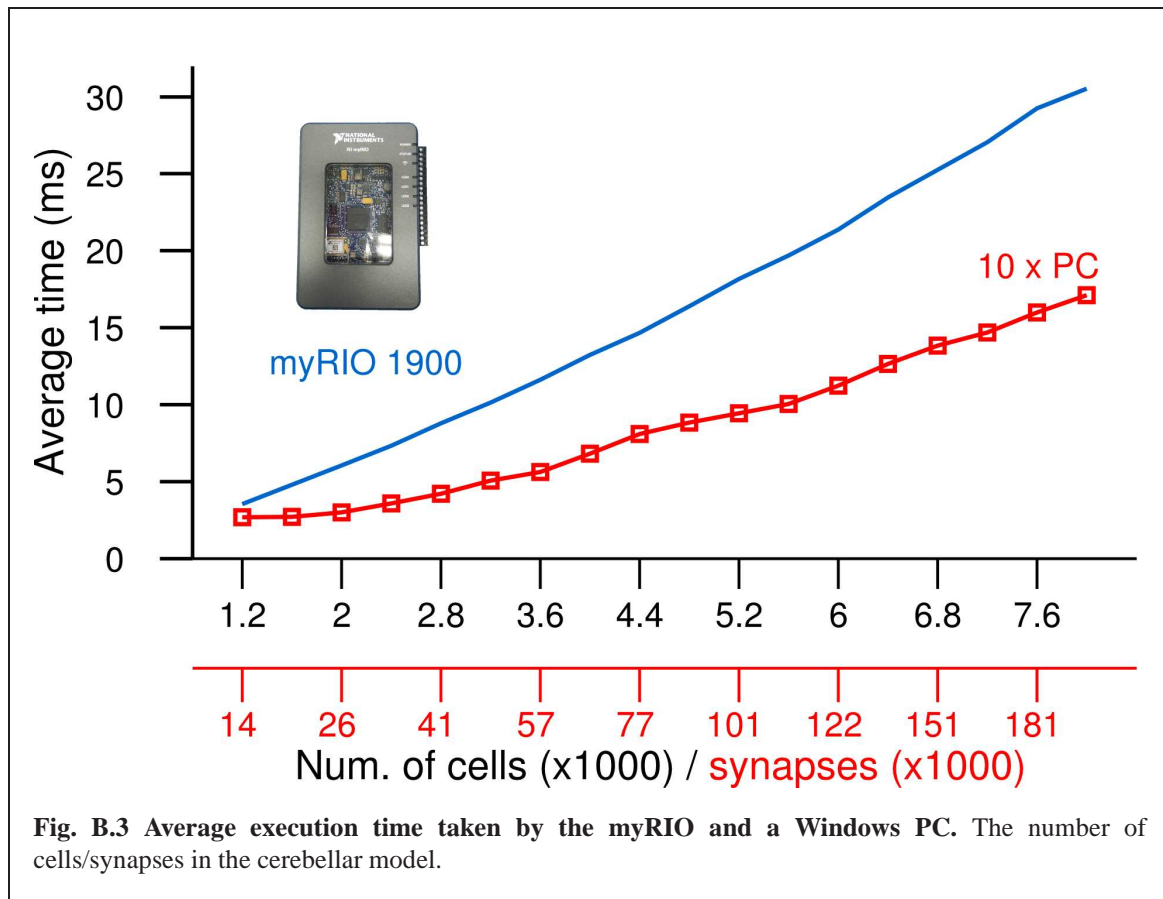


Fig. B.2 Comparison of the control performance achieved in terms of RSE of $\phi(t)$. When the cerebellar model is enable (red traces, N=10) and disabled (blue traces, N=3) using the NI myRIO-1900 real time device.

on a Windows laptop (Intel Core i5-2430M CPU @ 2.40GHz x 4, 8 GB DDR3 RAM). LabVIEW version 2013 was used during all the experiments. **Fig. B.3** shows the average time required by the myRIO and the Laptop (labeled *PC* multiplied by 10) versus the number of neuron cells and synapses. It evidences that the execution time in the RT device grows linearly with the number of synapses in the cerebellar model, whit a steeper gradient than in the PC. This figure serves as reference for choosing the maximum number of neurons in the cerebellar model for a given control scenario. For instance, the two-wheel robot used here has a sampling frequency of 10 ms. The execution time has to be below the sampling frequency and therefore the cerebellar model could include up to 3 k neurons with more than 57 k synapses in a myRIO device or more than 20 k and 380 k synapses in a PC. Slower sampling frequencies would allow larger size of cerebellar model whereas faster sampling frequencies would require smaller size.



B.4 Discussion

We presented in this document the implementation of our bi-hemispherical neuronal network model of the cerebellum in a stand-alone real time device. The cerebellar model was tested during control of a two-wheel balancing robot, outperforming the control performance attained when using a classical controller (PD controller). The RT device chosen (National Instruments myRIO-1900) brought flexibility and portability to the cerebellar model. To the best of our knowledge this is the first implementation of a realistic bi-hemispherical model of the cerebellum in a dedicated hardware device for solving a real world engineering problem.



List of publications

Reviewed Journal Papers

1. **Pinzon-Morales, R D** and Hirata, Y “A bi-hemispheric neuronal network model of the cerebellum with spontaneous climbing fiber firing produces asymmetrical motor learning during robot control”, *Frontiers in Neural Circuits*, 8(131), 2014
2. **Pinzon-Morales, R D** and Hirata, Y “Customization of Wavelet Function for Pupil Fluctuation Analysis to Evaluate Levels of Sleepiness”, *Communication and Computer*, 10(1):585–592, 2013.
3. **Pinzon-Morales, R D** and Baquero-Duarte, K A and Orozco-Gutierrez, A A and Grisales-Palacio, V H “Pattern Recognition of Surface EMG Biological Signals by Means of Hilbert Spectrum and Fuzzy Clustering”, *Software Tools and Algorithms for Biological Systems: Advances in Experimental Medicine and Biology*, 696:201–209, 2011.
4. **Pinzon-Morales, R D** and Orozco-Gutierrez, A A and Castellanos-Dominguez, C G “Novel signal-dependent filter bank method for identification of multiple basal ganglia nuclei in Parkinsonian patients”, *Neural Engineering*, 8(3):036026, 2011.

5. **Pinzon-Morales, R D** and Orozco-Gutierrez, A A and Castellanos-Dominguez, C G “Caracterización multicanal no lineal de señales emg con la transformada hilbert-huang”, *Scientia et Technica*, 41(1):36–41, 2009.
6. **Pinzon-Morales, R D** and Morales-Barrera, D-A and Grisales-Palacio, V-H “Caracterización de señales electromiográficas para la discriminación de seis movimientos de la mano”, *Scientia et Technica*, 42(2):278–283, 2009.

Journal Papers under review

1. **Pinzon-Morales, R D** and Hirata, Y “Error signals used for cerebellar motor learning: evaluation in real world adaptive robot control using a cerebellar neuronal network model” 2014. Submitted to *BMC Neuroscience*.
2. **Pinzon-Morales, R D** and Hirata, Y “Realistic bi-hemispherical model of the cerebellum uncovers the purpose of the abundant granular cells during robot control” 2014. Submitted to *Frontiers in Neural Circuits*.
3. **Pinzon-Morales, R D** and Hirata, Y “Efficient implementation of neural network models of the cerebellum using LabVIEW for engineering applicationsl” 2014. Submitted to *Advances in Software Engineering*.

Peer reviewed conference papers

1. **Pinzon-Morales, R D** and Hirata, Y “Spontaneous firing activity in climbing fiber is critical for a realistic bi-hemispherical cerebellar neuronal network during robot control”, *23th Annual Computational Neuroscience Meeting: CNS2014*, Quebec, Canada, 2014.
2. **Pinzon-Morales, R D** and Hirata, Y “The number of granular cells in a cerebellar neuronal network model engaged during robot control increases with the complexity of the motor task”, *23th Annual Computational Neuroscience Meeting: CNS2014*, Quebec, Canada, 2014.
3. **Pinzon-Morales, R D** and Hirata, Y “Number of granular cells in a bi-hemispherical model of the cerebellum correlates with robot control performance”, *24th Annual Conference of the Japanese Neural Network Society: JNNS2014*, Hokkaido, Japan, 2014.

4. **Pinzon-Morales, R D** and Hirata, Y “A portable stand-alone bi-hemispherical neuronal network model of the cerebellum for adaptive robot control ”, *The 2014 IEEE International Conference on Robotics and Biomimetics: ROBIO2014*, Bali, Indonesia, 2014.
5. **Pinzon-Morales, R D** and Hirata, Y “Cerebellar-inspired bi-hemispheric neural network for adaptive control of an unstable robot ”*Biosignals and Biorobotics Conference: BRC2013, ISSNIP2013*, Rio de Janeiro, Brazil, 2013.
6. **Pinzon-Morales, R D** and Hirata, Y “Customization of wavelet function for pupil fluctuation analysis to evaluate levels of sleepiness”*11th international conference on Signal Processing: SIP2012*, Saint Malo and Mont Saint-Michel, France, 2012.
7. **Pinzon-Morales, R D** and Yohei, Ohata and Hirata, Y “Adaptive control of 2-wheeled balancing robot by two hemispheric cerebellar neuronal network model”*21st Annual Computational Neuroscience Meeting: CNS2012*, Decatur, GA, USA, 2012.
8. **Pinzon-Morales, R D** and Orozco-Gutierrez, A A and Castellanos-Dominguez, C G “EEG seizure identification by using optimized wavelet decomposition”*IEEE Engineering in Medicine and Biology Society: EMB2011*, Boston, MA, USA, 2011.
9. **Pinzon-Morales, R D** and Orozco-Gutierrez, A A and Castellanos-Dominguez, C G and Guido, R C “The Discrete Lifting Shapelet Transform for biological pattern recognition”*IEEE Conference on Neural Engineering: NER2011*, Cancun, Mexico, 2011.
10. **Pinzon-Morales, R D** and Restrepo, F and Moscoso, O and Castro-Cabrera, P A , and Orozco-Gutiérrez, A A and Castellanos-Dominguez, C G “Detection of Attention-Deficit/Hyperactivity Disorder based on Customized Wavelet”*XXVIII Congreso Anual de la Sociedad Española de Ingeniería Biomédica: CASEIB2010*, Madrid, Spain, 2010.
11. **Pinzon-Morales, R D** and Orozco-Gutierrez, A A and Castellanos-Dominguez, C G “Feature selection using an ensemble of optimal wavelet packet and learning machine: Application to MER signals”*7th Symposium on Communication Systems Networks and Digital Signal Processing: CSNDSP2010*, Newcastle, UK, 2010.
12. **Pinzon-Morales, R D** and Orozco-Gutierrez, A A and Castellanos-Dominguez, C G “Towards high accuracy classification of MER signals for target localization in

- Parkinson's disease" *IEEE Engineering in Medicine and Biology Society: EMB2010*, Buenos Aires, Argentina, 2010.
13. **Pinzon-Morales, R D** and Orozco-Gutierrez, A A and Garces A, M "Automatic identification of various nuclei in the basal ganglia for Parkinson's disease neurosurgery", *IEEE Engineering in Medicine and Biology Society: EMB2009*, Boston, MA, USA, 2009.
 14. Carmona-Villada, H and Orozco-Gutierrez, A A and Castellanos-Dominguez, C G and Betancourt, G and, **Pinzon-Morales, R D** and Gomez, D "Refinement of Automatic Neurophysiological Detection of Subthalamic Nucleus Targeting for Surgical Treatment of Parkinson Disease " *6th Annual World Congress for Brain Mapping and Image Guided Therapy* Minneapolis, MN, USA, 2009.
 15. **Pinzon-Morales, R D** and Orozco-Gutierrez, A A and Baquero-Duarte, K A and Grisales-Palacio, V H "Hand Movement Recognition based on Empirical Mode Decomposition" *Signal and Image Processing: SIP 2009*, Hawaii, USA, 2009.

Awards

Conference Awards

- Travel award: 23th Annual Meeting of the Organization for Computational Neuroscience, CNS2014 Jul 2014
- 2nd best paper: IEEE Engineering in Medicine and Biology Society. Sept 2010
Paper's title: "*Towards high accuracy classification of MER signals for target localization in Parkinson's disease*".
- 2nd best poster: VII IEEE Latin-American Summer School on Dec 2010
Computational Intelligence. Poster's title: "*On the wavelet transform customization via machine learning for biological signal processing*".

Scholarship — Japanese Ministry of Education, Culture, Sports, Science and Technology Education

- Monbukagakusho Scholarship for graduate studies Mar 2011

Grants — Chubu University, Graduate School Engineering

- Special internal grant for graduate students 2014 Feb 2014

- Special internal grant for graduate students 2012 Feb 2012

Special Award — Nagoya City Industrial Group

- Special prize at the regional technology entrepreneurship contest Jan 2014
Campus Venture Grand-prix. Project: *Mobile health application for supporting health services delivery in remote villages*. Nagoya, Japan